

Stephen F. Austin State University

**SFA ScholarWorks**

---

Electronic Theses and Dissertations

---

Spring 5-11-2024

## **INVESTIGATION OF RESIDUAL MINERAL CONTENT OF BAUXITE STOCKPILES, SALINE MINING DISTRICT, ARKANSAS, U.S.A.**

Melanie L. Ertoms

*Stephen F Austin State University*, [ertonsml@jacks.sfasu.edu](mailto:ertonsml@jacks.sfasu.edu)

Follow this and additional works at: <https://scholarworks.sfasu.edu/etds>

 Part of the [Geochemistry Commons](#), [Geology Commons](#), and the [Natural Resources and Conservation Commons](#)

[Tell us](#) how this article helped you.

---

### **Repository Citation**

Ertoms, Melanie L., "INVESTIGATION OF RESIDUAL MINERAL CONTENT OF BAUXITE STOCKPILES, SALINE MINING DISTRICT, ARKANSAS, U.S.A." (2024). *Electronic Theses and Dissertations*. 536.  
<https://scholarworks.sfasu.edu/etds/536>

This Thesis is brought to you for free and open access by SFA ScholarWorks. It has been accepted for inclusion in Electronic Theses and Dissertations by an authorized administrator of SFA ScholarWorks. For more information, please contact [cdsscholarworks@sfasu.edu](mailto:cdsscholarworks@sfasu.edu).

---

## INVESTIGATION OF RESIDUAL MINERAL CONTENT OF BAUXITE STOCKPILES, SALINE MINING DISTRICT, ARKANSAS, U.S.A.

### Creative Commons License



This work is licensed under a [Creative Commons Attribution-Noncommercial-No Derivative Works 4.0 License](#).

INVESTIGATION OF RESIDUAL MINERAL CONTENT OF BAUXITE STOCKPILES,  
SALINE MINING DISTRICT, ARKANSAS, U.S.A.

By

MELANIE ERTONS, Bachelor of Science

Presented to the Faculty of the Graduate School of  
Stephen F. Austin State University

In Partial Fulfillment

Of the Requirements

For the Degree of

Master of Science

STEPHEN F. AUSTIN STATE UNIVERSITY

May, 2024

INVESTIGATION OF RESIDUAL MINERAL CONTENT OF BAUXITE STOCKPILES,  
SALINE MINING DISTRICT, ARKANSAS, U.S.A.

By

MELANIE ERTONS, Bachelor of Science

APPROVED:

---

Dr. Melinda Faulkner, Thesis Director

---

Dr. Julie Bloxson, Committee Member

---

Dr. Zachariah Fleming, Committee Member

---

Dr. I-Kuai Hung, Committee Member

---

Forrest Lane, Ph. D.  
Dean of Research and Graduate Studies

---

## **ABSTRACT**

The former mining town of Bauxite is in the Saline County Mining District, in central Arkansas. Bauxite is located approximately 40 km (25 mi) southwest of Little Rock just east of Benton, Arkansas. This area contains extensive deposits of bauxite ore and nepheline syenite previously mined by Aluminum Company of America using open pit and subsurface mining techniques. This study incorporates five bauxite stockpiles (SP1, Clay, SP2, SP3, SP4) with varying amounts of alumina content situated on approximately 10 acres of land within an area of the former mine recognized as Section 20. Over the past several years, there has been renewed economic interest in minerals that can be derived from bauxite and related residues due to the rapid evolution in modern technologies including batteries, alloys, lasers, and much more. There have been investigations on bauxite ore and residue around the world, but the minerals within each setting where bauxite forms may vary depending on parent material, dissolution patterns, and time, potentially yielding elements that may have economic value.

One-hundred twenty-eight (128) rock samples were collected from five stockpiles and analyzed using X-ray fluorescence (XRF) and Laser Ablation – Inductively Coupled Plasma – Mass Spectrometry (LA-ICP-MS). Several samples had elements that were determined to be enriched using XRF and/or LA-ICP-MS with respect to background concentrations in the Earth's upper continental crust and/or a NIST-698 sample (Jamaican bauxite standard), including some which are on the 2022 List of Critical Minerals. Comparing XRF and LA-ICP-MS results, Si, Ca, Rb, Sr, Zr, Nb, and Mo had very strong correlations. A table showing correlations among elements tested in XRF and LA-ICP-MS compared to Fe, Ti, and Al was created to assess for elemental relationships.

In addition to element information, volume analyses of each stockpile were completed using both open source (QGIS) and commercial (ArcGIS Pro) GIS software for processing. A programmed flight with a DJI Mavic Pro 2 drone was used to complete the survey and obtain images to create maps of the study area. For all stockpiles, QGIS and ArcGIS had a statistically significant difference in mean volume calculations. The largest percent difference between each software for the averaged stockpile volumes was 4.2%. Mean volumes were consistently higher in ArcGIS for each stockpile. Maps depicting the spatial distribution of elements (Sr, Zr, Nb, Si, Ca, and Mo) were generated using ArcGIS Pro to assess mobility by evaluating changes in element concentrations of the five stockpiles. Higher values of Sr, Zr, Nb, and Ca were noted in stockpiles with higher alumina ( $\text{Al}_2\text{O}_3$ ) content. The hydrolysates (Zr and Nb) with the exception of Mo, mobilized around the base and slope of SP2, the tallest stockpile among the five in this study.

The chemical characteristics of each stockpile may provide understanding to elemental patterns and metal affinities within bauxite ores. The relationship between bauxite stockpile aluminum concentrations and the presence of elements associated with critical minerals could potentially lead to a future economic supply of important resources.

## **ACKNOWLEDGEMENTS**

Many people were involved throughout the process of completing this project and deserve recognition for their efforts. I would like to thank the McGeorge Contracting Company, specifically Anthony Jones, for providing information and access to the Section 20 mine study area. Funding was provided by Texas Academy of Science, Houston Geological Society, and East Texas Gem and Mineral Society which supported the sample collection and analyses required to complete this research, for which I am truly grateful. I would like to recognize the Department of Earth Sciences and Geologic Resources at Stephen F. Austin State University, they provided facilities and a department vehicle at times to help with my research activities. Also, thanks to Dr. Kevin Werts at TexasTech GeoAnalytical Laboratory for assisting with sample analysis. To Courtney Kaufman, thank you for your many hours of helping prep samples for analysis. Thank you, Dr. Greg Miller, for helping me navigate statistics used in this research. To my friend, Dr. Katy Trotty, thank you for enduring my many questions and the moral support throughout this thesis. I appreciate all the hard work and dedication that my committee members put into helping me succeed in this project. A special thanks to Dr. Julie Bloxson for answering my many questions about sample analyses and interpretation. Her dedication to students is unmatched. Thank you, Dr. I-Kuai Hung and Dr. Zachariah Fleming for sharing your time and expertise helping me navigate spatial analysis, ultimately enhancing my research. Finally, I want to thank my thesis advisor, Dr. Mindy Faulkner, for guiding me through this venture and her encouragement along the way. She has watched me grow as a student and is always up for a new adventure. Thank you all for the support throughout this project.

## TABLE OF CONTENTS

ABSTRACT .....	iii
ACKNOWLEDGMENTS .....	v
TABLE OF CONTENTS .....	vi
LIST OF FIGURES.....	ix
LIST OF TABLES.....	xi
LIST OF EQUATIONS .....	xiii
INTRODUCTION.....	1
GEOLOGIC SETTING AND REGIONAL STRUCTURE .....	7
Paleo-Physiography/Climate .....	15
Hydrogeology (Surface and Subsurface).....	15
Soils .....	18
Geochemistry and Mineralogy.....	18
OBJECTIVES .....	24
SIGNIFICANCE.....	25
METHODOLOGY .....	26
UAV Image Processing.....	27
Volume Measurement – ArcGIS Pro.....	30
Volume Measurement – QGIS.....	33

Accuracy Assessment of Stockpile Volumes.....	38
Rock Sample Collection .....	39
X-Ray Fluorescence (XRF).....	42
Laser Ablation – Inductively Coupled Plasma – Mass Spectrometry (LA-ICP-MS).....	45
Statistical Analysis of Elements .....	46
Spatial Distribution of Elements .....	51
RESULTS.....	53
Stockpile Volume.....	53
XRF Analyses: Elements Detected .....	56
LA-ICP-MS Analyses.....	56
Comparison of XRF and LA-ICP-MS Data.....	59
Sample Enrichment Compared to Earth's Upper Continental Crust .....	64
XRF Sample Enrichment: Earth's Upper Continental Crust .....	64
LA-ICP-MS Sample Enrichment: Earth's Upper Continental Crust .....	66
Sample Enrichment Compared to NIST-698 Sample.....	69
XRF Sample Enrichment: NIST – 698 .....	69
LA-ICP-MS Sample Enrichment: NIST – 698.....	71
Fe, Al, Ti Correlations .....	73
Spatial Distribution of Elements .....	76
Discussion.....	84

Volume Analysis .....	84
Elemental Presence.....	84
Comparison of XRF and LA-ICP-MS Results.....	85
Comparison of Elemental Values: Earth's Upper Continental Crust.....	86
Comparison of Elemental Values: NIST-698 (Jamaican bauxite standard) Sample .....	87
Fe, Ti, and Al Correlations .....	89
Spatial Distribution of Elements .....	91
LIMITATIONS .....	93
Conclusion.....	94
FUTURE WORK.....	97
REFERENCES .....	98
APPENDICES .....	105
VITA .....	190

## LIST OF FIGURES

Figure 1. Map outlining study area in Arkansas, U.S.A.....	3
Figure 2. Map outlining boundary of ALCOA .....	4
Figure 3. Image of five stockpiles in Section 20 at former ALCOA mine .....	5
Figure 4. Overview of Wilson cycles affecting southern U.S.A.....	8
Figure 5. Structural boundaries of Arkansas, U.S.A. ....	9
Figure 6. Stratigraphic section of Central Arkansas during Mesozoic and Cenozoic Eras.	12
Figure 7. Stratigraphic section for bauxite district in Saline County, Arkansas.....	14
Figure 8. Upper Saline watershed boundary .....	17
Figure 9. Images of bauxite textures .....	19
Figure 10. Image of clasts .....	20
Figure 11. Ionic potential of elements .....	21
Figure 12. Orthorectified image of Section 20 mine .....	28
Figure 13. Digital surface model of Section 20 mine .....	29
Figure 14. Polygon of SP4 for volume calculation – ArcGIS Pro .....	31
Figure 15. ArcGIS Pro workflow for volume calculation.....	32
Figure 16. Temporary polygon of SP4 for volume calculation – QGIS.....	34
Figure 17. Interpolated base surface layer – QGIS .....	35

Figure 18. Elevation differences in raster layer – QGIS .....	36
Figure 19: QGIS workflow for calculating volume for a stockpile .....	38
Figure 20. Sample collection locations in Section 20.....	41
Figure 21. Images of sample preparation for XRF .....	43
Figure 22. Reported elements on XRF and LA-ICP-MS .....	44
Figure 23. Scatter plots to determine linear relationship .....	47
Figure 24. Scatter plots of XRF and LA-ICP-MS results showing linear relationship .....	60
Figure 25. Scatter plots of XRF and LA-ICP-MS results showing non-linear relationship.	63
Figure 26. Spatial distribution map of Sr .....	78
Figure 27. Spatial distribution map of Zr .....	79
Figure 28. Spatial distribution map of Nb.....	80
Figure 29. Spatial distribution map of Si.....	81
Figure 30. Spatial distribution map of Ca .....	82
Figure 31. Spatial distribution map of Mo .....	83
Figure 32. Scatterplot of Ta-Nb from LA-ICP-MS results .....	89
Figure 33. Scatterplot of Pr-Nd from LA-ICP-MS results.....	90
Figure 34. Scatterplot of Hf-Zr from LA-ICP-MS results.....	91

## LIST OF TABLES

Table 1: Pearson's correlation coefficient (r) ranges and description.....	48
Table 2. Baseline values of upper continental crust and NIST-698 XRF values .....	49
Table 3. Volume measurements for QGIS and ArcGIS Pro .....	54
Table 4. Independent sample t-test results of volume analyses.....	55
Table 5. Stockpile volumes: percent difference of mean .....	55
Table 6. Elements detected: XRF .....	57
Table 7. Abbreviated list of LA-ICP-MS results .....	58
Table 8. Pearson's correlation coefficient values from XRF and LA-ICP-MS analyses.....	62
Table 9. XRF: percentage of samples enriched compared to Earth's upper continental crust .....	65
Table 10. LA-ICP-MS: percent greater than Earth's upper continental crust .....	67
Table 11. XRF: percentage of samples enriched compared to NIST-698 sample.....	70
Table 12. LA-ICP-MS results: elements enriched compared to NIST-698 sample.....	71
Table 13. LA-ICP-MS: percent greater than NIST-698.....	72
Table 14. Correlation coefficient values comparing elements in stockpiles to Fe, Ti, and Al using XRF .....	74
Table 15. Correlation coefficient values comparing elements in clasts and matrix to Fe, Ti, and Al using XRF .....	75

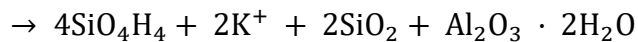
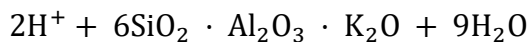
Table 16. Correlation coefficient values comparing Ti to elements using LA-ICP-MS results.....	76
--	----

## LIST OF EQUATIONS

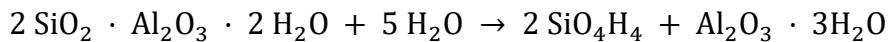
Equation 1. Chemical change of feldspar to gibbsite ..... 23



Equation 2. Chemical change of feldspar to kaolinite ..... 23



Equation 3. Chemical change of kaolinite to gibbsite ..... 23



Equation 4. Percent difference ..... 39

$$\text{Percent difference (\%)} = \left( \frac{|\text{Volume 1} - \text{Volume 2}|}{\frac{(\text{Volume 1} + \text{Volume 2})}{2}} \right) * 100$$

Equation 5. Percent greater value ..... 50

$$\text{Percent Greater Value (\%)} = \left[ \left( \frac{\text{NIST698 element value}}{\text{LAICPMS element value}} \right) - 1 \right] * 100$$

Equation 6. Percent of enriched samples ..... 50

$$\text{Enriched samples (\%)} = \frac{\text{number of enriched samples in stockpile}}{\text{total samples in stockpile}} * 100$$

## **INTRODUCTION**

Bauxite deposits in central Arkansas are well-known alumina bearing ores that reside in the southeastern portion of the Saline Mining District, where exposed Cretaceous-aged nepheline syenite domes were heavily weathered in a tropical environment during the Eocene Epoch (Eby and Vasconcelos, 2009; Guccione, 1993; Geologic History, 2020). Mining of bauxite for alumina in Saline County peaked during World War II (WWII), with significant extraction of ore resources performed by Reynolds Company and Aluminum Company of America (ALCOA) (Bush, 2007). Open pit mines were and still are the dominate method of obtaining bauxite ore, however, several underground mines were used intermittently throughout early to mid-1900s (Bramlette, 1936; Gordon et al., 1958; Van Gosen and Choate, 2021). Bauxite mining declined significantly in the United States after WWII, with smaller operators mining bauxite for commercial use in the construction, oil and gas, automobile, and chemical industries (Bush, 2007; Valeton, 1972). Most of the high-grade ore has been extracted and processed, leaving lower grade materials suitable for aggregate, cement, and proppants used in hydraulic fracturing (Bush, 2007). At present, active mining of bauxite at the ALCOA mine in central Arkansas has ceased, with prior excavated ore rock sorted into stockpiles based on alumina content at the mine site. A small fraction of the remaining

bauxite can be used as aggregate in construction materials, environmental restoration, or various neutralization projects however, the high alkalinity, salinity, and mineralogy of bauxite can be obstacles to these practices (Wang et al., 2018).

Recently, there has been interest in other economic minerals that can be derived from bauxite and related residues due to the rapid evolution in modern technologies including batteries, alloys, lasers, and much more. Many minerals, some now identified as critical minerals, were not commonly extracted in the past but are now considered crucial to advancing technologies. The complete 2022 Final List of Critical Minerals and common uses can be viewed in Appendix A (Burton, 2022). Elements that commonly make up minerals are defined as critical minerals in the 2022 Final List of Critical Minerals (Burton, 2022); therefore, this study will do the same. There have been investigations of bauxite ore and residue around the world, but the minerals within each setting where bauxite forms may vary depending on parent material, dissolution patterns, and time, potentially yielding elements that may have economic value. This study will assess the potential for critical minerals within bauxite in Arkansas, by evaluating both the presence and mobilization of trace elements of five stockpiles within Section 20 of the former ALCOA bauxite mine.

Bauxite, Arkansas is located approximately 40 km (25 mi) southwest of Little Rock just east of Benton, Arkansas (Google, 2022; Figure 1). This area has extensive deposits of bauxite ore and nepheline syenite as reported by Bramlette (1932), Branner

(1897), Stearn (1930), and Gordon et al. (1958). This study incorporates five bauxite stockpiles (SP1, Clay, SP2, SP3, SP4) with varying amounts of alumina content situated on approximately 10 acres of land within an area of the former ALCOA mine recognized as Section 20 (Figures 2, 3).

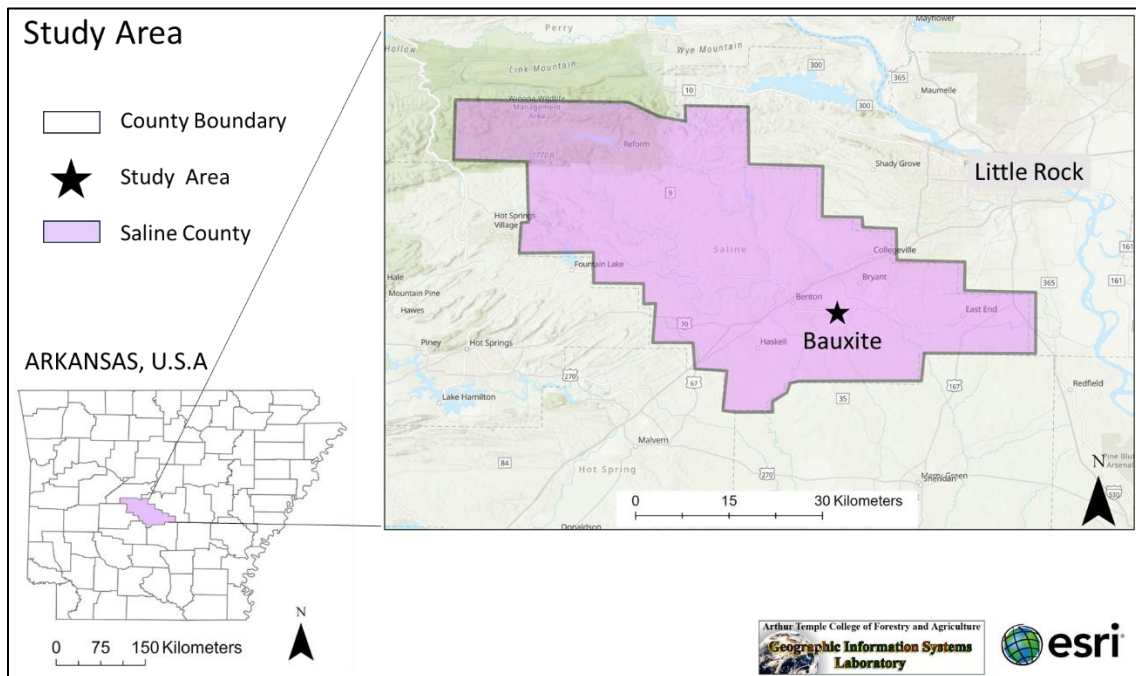


Figure 1: A map showing Saline County and the study area (black star) in Bauxite, Arkansas U.S.A (data from Bureau, U.C., 2021).

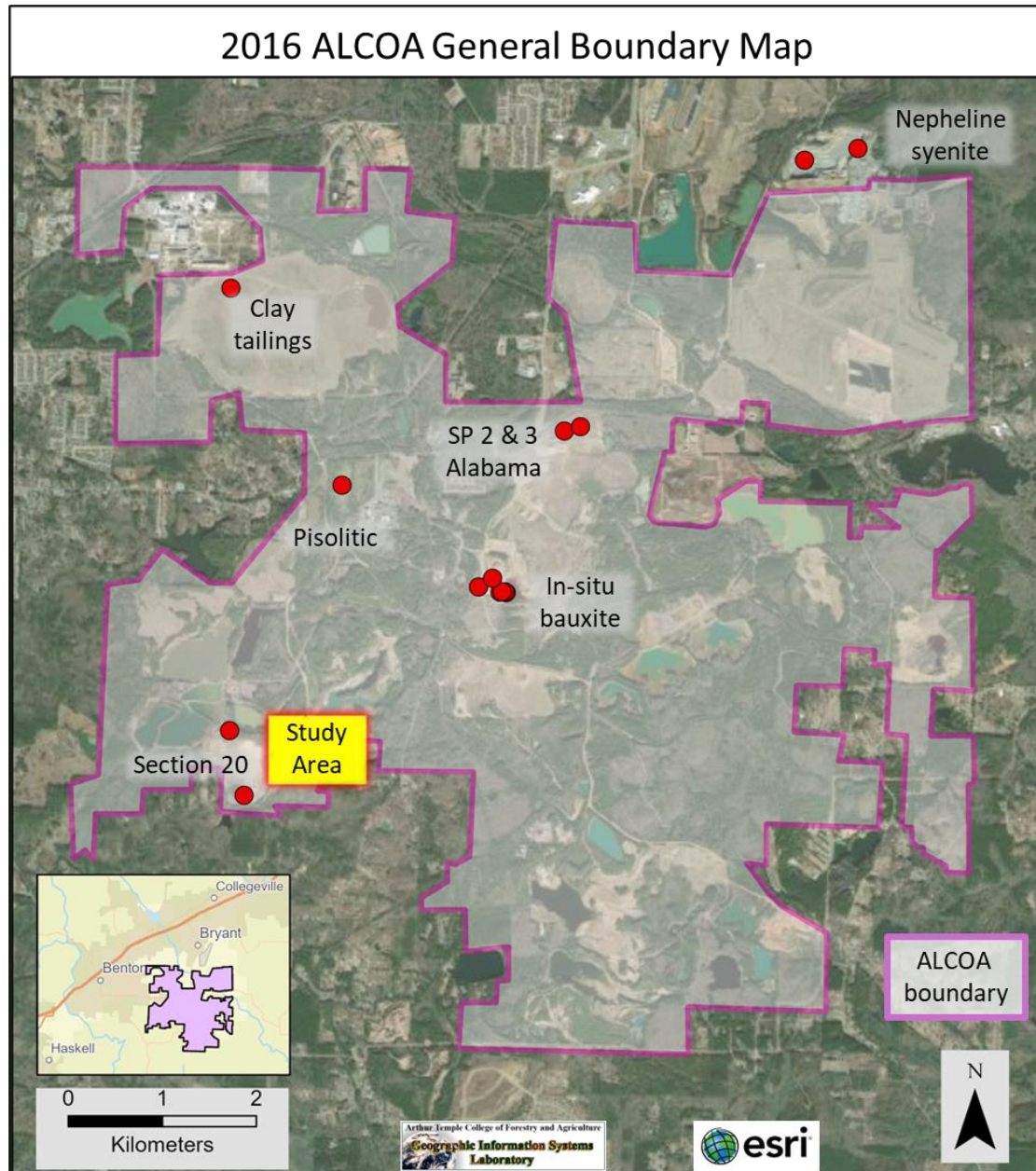


Figure 2. Map from 2016 outlining boundary (in yellow) of Aluminum Company of America (ALCOA) bauxite mine. The study area is located in the southwestern corner of map (outlined in red). Dots (in red) represent sample areas investigated by Van Gosen and Choate in study published in 2021. (Boundary information provided by McGeorge Contracting Company)



Figure 3: View of five stockpiles within study area with respective alumina content in weight percent identified from right to left as SP1, Clay, SP2, SP3 and SP4 in Section 20 of the former ALCOA mine in Bauxite, Arkansas. SP1: 70-80%, Clay: less than 50%, SP2: 50 - 60 %, SP3: 60-70%, SP4: over 80%. (Weight percent information provided by McGeorge Contracting Company)

Both X-ray fluorescence (XRF) and laser ablation - inductively coupled plasma – mass spectrometry (LA-ICP-MS) were used for analysis to identify and characterize economic and environmentally sensitive minerals in bauxite stockpiles. The most recent study published by Van Gosen and Choate (2021), working with the United States Geological Survey, examined major and trace elements of bauxite deposits in Saline and

Pulaski Counties including bauxite ore, syenite, and processed bauxite (residues and clays). Figure 2 displays sample sites investigated by Van Gosen and Choate in study published in 2021. They found gallium (Ga) and niobium (Nb) were present in economic concentrations; other residual elements were of little economic value at current prices, similar to the results of Schulte and Foley (2014) and Gordon and Murata (1952) (Van Gosen and Choate, 2021).

In addition to elemental information, volume analysis of each stockpile was completed using both open (QGIS – Quantum Geographic Information System) and commercial (ArcGIS Pro – Arc Geographic Information System Pro) software for processing. A programmed flight with a DJI Mavic Pro 2 drone was used to complete the survey and obtain images used to make a map of the study area. Spatial analysis techniques were employed to characterize surface elemental concentrations and evaluate the mobility, if any, of elements throughout each stockpile.

## **GEOLOGIC SETTING AND REGIONAL STRUCTURE**

Present-day central Arkansas has been affected by major compressional and extensional tectonic processes throughout its existence. Major tectonic events that impacted central Arkansas include the Grenville Orogeny (1350Ma to 1000Ma), Iapetus Ocean development (760Ma to 530Ma), Ouachita Orogeny (320Ma to 245Ma), and the most recent opening of the Atlantic Ocean (Guccione, 1993; Thomas, 2006; Figure 4).

The location of this study is on the border of three different physiographic regions in Arkansas: West Gulf Coastal Plain, Ouachita Mountains, and Mississippi River Alluvial Plain (Howard, 1987; McFarland, 2004; Figure 5). The Ouachita Mountains region is a subdivision of the Interior Highlands, along with the Arkansas River Valley to the north (Gordon et al., 1958; Howard, 1987). The Ouachita Mountains province extends westward into Oklahoma and is identified by high ridges with a notable northwest trend that developed over Paleozoic-aged fold and thrust structures with east-west orientations (Gordon et al., 1958; Guccione, 1993). The Coastal Plain, West Gulf Coastal Plain, and Mississippi River Alluvial Plain, are comprised of low-relief undulating landscapes (Gordon et al., 1958; Guccione, 1993; Howard, 1987). The Mississippi River Alluvial Plain in this area extends east and straddles the border between Mississippi and Arkansas then narrows to the south upon approaching

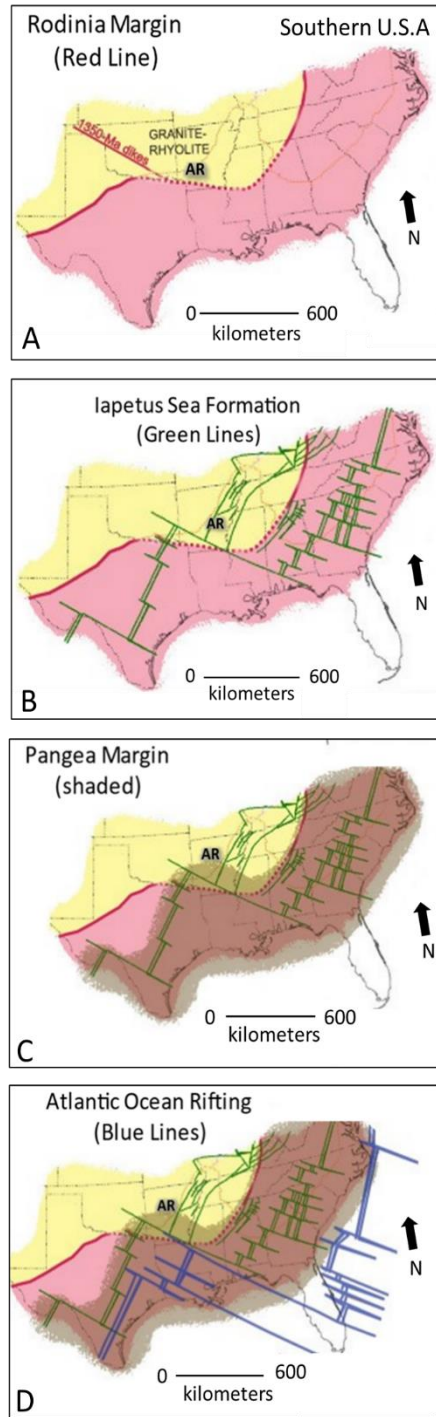


Figure 4. Simplified view of two Wilson Cycle deformation events related to the southern USA. (A) Rodina compressional margin (red line). (B) Rifting of Iapetus Sea (green lines). (C) Pangea compressional margin (shaded area). (D) Rifting of Atlantic Ocean. AR- Arkansas (modified from Thomas 2006).

- Symbol
- / Rift
  - Transform
  - / Intracratonic basement fault

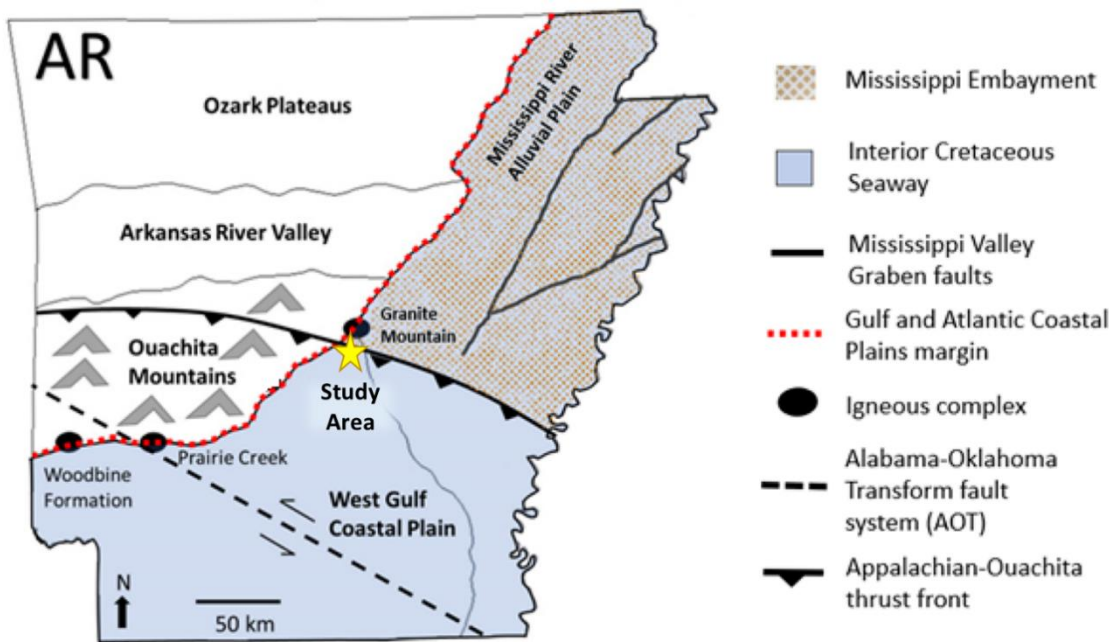


Figure 5: Arkansas state map identifying structural boundaries for Mississippi Embayment (tan dots), Ouachita Mountains (chevrons), Alabama-Oklahoma Transform fault system (AOT), Mississippi Valley Graben faults (black extended lines in NE corner), Interior Cretaceous seaway (shaded area in the south and eastern sections of map), black dots represent selected igneous complexes from the Upper Cretaceous in central Arkansas, star represents study area in Saline Mining District (modified from Baksi, 1997; Cox et al., 2014; Guccione 1993; Howard, 1987; Thomas 1991).

Louisiana (Guccione, 1993; Howard 1987). The Mississippi Alluvial Plain has been subjected to depositional and erosional forces associated with the Mississippi River system and contains geomorphic features including floodplains, meandering river beds, and glacial retreat (Guccione, 1993; Howard 1987).

Some notable structures in the state include the Mississippi Embayment, the northwesterly striking Alabama-Oklahoma transform (AOT) fault, and the Appalachia-Ouachita thrust front (Cox et al., 2014; Van Arsdale, 1998; Figure 5). The Mississippi Embayment is a south-plunging syncline with the axis approximately aligned with the Mississippi River located along the eastern/northeastern corner of Arkansas (Van Arsdale, 1998). Overprinting of the late Paleozoic Mississippi Valley Graben fault system by the Mississippi Embayment (Mesozoic-Cenozoic) alludes to an area of weakness within the crust (Cox and Van Arsdale, 2002; Thomas, 2006). During the Triassic-Jurassic, as Pangaea rifted apart, grabens that were stretched across the lower portion of the state, likely from uplift and extensional faulting, were eventually filled with sediments from the nearby eroding Ouachita Mountains (Cox et al., 2014; Guccione, 1993).

A group of alkaline igneous complexes were identified in central Arkansas with radiometric ages for emplacement ranging from 108 to 88 Ma (Baksi, 1997; Eby and Vasconcelos, 2009; Matton and Jébrak, 2009). In Saline County, Arkansas, the igneous rocks were found to be primarily composed of nepheline syenite and other associated igneous rocks that intruded into Paleozoic rocks (Eby and Vasconcelos, 2009; Flohr & Howard, 1994). Nepheline syenite is a coarse-grained igneous rock that resembles granite, made of orthoclase with little to no quartz present (Nepheline Syenite, 2024). Documented exposures of the alkaline igneous intrusions in central Arkansas are

situated along the southern portion of the Gulf and Atlantic Coastal Plains margin (Cox and Van Arsdale, 2002; Eby and Vasconcelos, 2009; Figure 5).

The mechanism for emplacement of these alkaline intrusive bodies remains a point of discussion among scientists (Cox and Van Arsdale, 2002; Eby and Vasconcelos, 2009; Matton and Jébrak, 2009; Vogt and Jung, 2007). One theory for their emplacement includes the Mississippi Valley Graben traveling over the Bermuda hotspot during the mid-Cretaceous and reactivating faults in the neighboring areas (Cox and Van Arsdale, 2002). An alternate theory suggests that edge-driven convection led to extensional deformation and reorganization of plates, subsequently reactivating faults, thus allowing magma to rise through the weakened conduits (Matton and Jébrak, 2009).

Current models suggest that during the Paleozoic Era, present-day Arkansas was located in a deep marine environment until the mid-Pennsylvanian Period when Pangea began to form (Geology of Arkansas, 2020; Guccione, 1993). Many rock units were dominated by shales, fossiliferous limestones interbedded with shale, and sandstones interbedded with shale (McFarland, 2004; Stone, 1986). Formations in the area include the Bigfork Chert (Ordovician), Polk Creek Shale (Ordovician), Missouri Mountain Shale (Silurian), Arkansas Novaculite (Devonian and Mississippian), and Stanley Shale (Mississippian) (Stone, 1986). Rocks from the early parts of the Mesozoic Era are missing from the geologic record, likely as a result of weathering and erosion events in the area

related to its exposure above sea level at the time (Guccione, 1993; Figure 6). During the Cretaceous, a shallow sea known as the Interior Cretaceous seaway formed near the

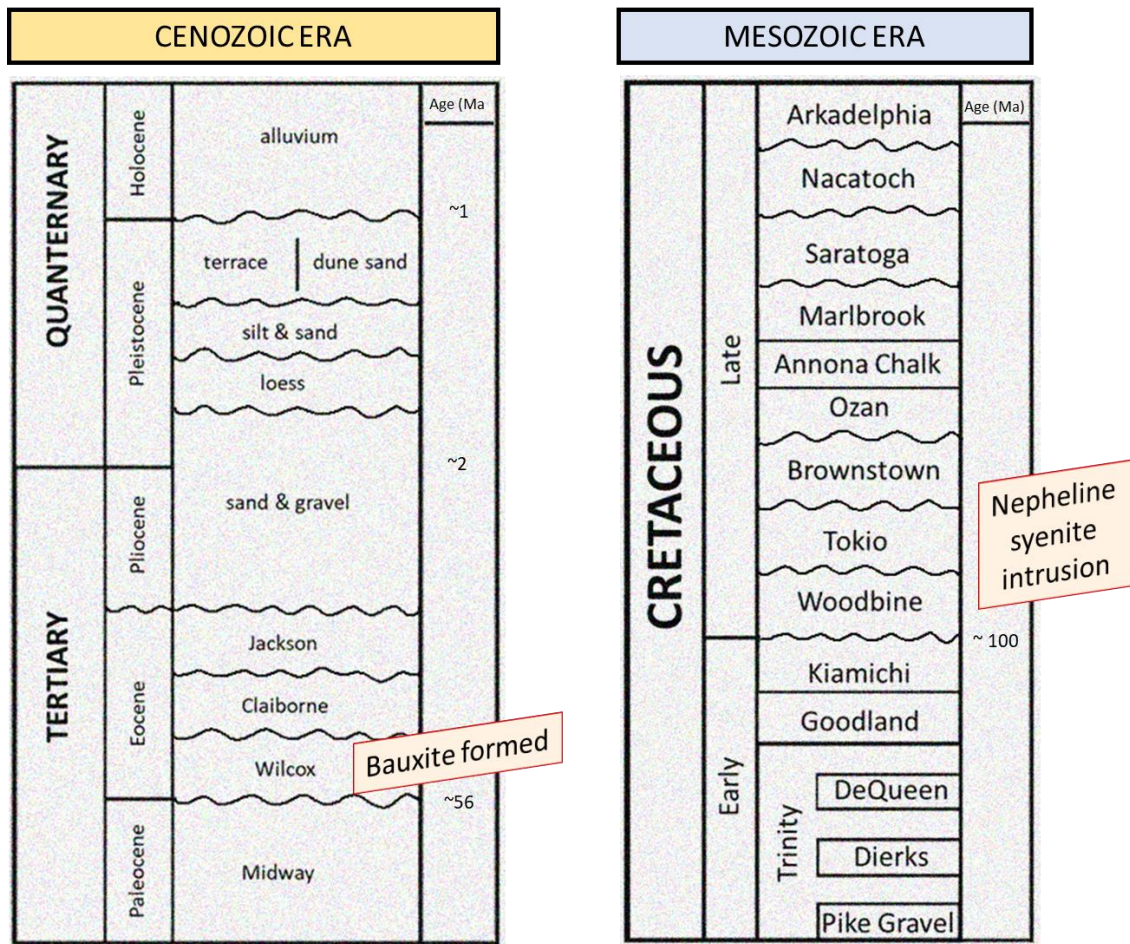


Figure 6: Stratigraphic section of the Central Arkansas region during the Mesozoic and Cenozoic Eras. Unconformities between formations are marked by a wavy line. Approximate ages for nepheline syenite intrusion and bauxite development are shown in boxes outlined in red. This chart does not depict the thickness of layers (modified from McFarland, 2004).

southern portion of present-day central Arkansas (Geology of Arkansas, 2020; Guccione, 1993). Nepheline syenite was emplaced as a slowly cooling pluton, likely resulting from complex extensional deformation and subsidence in the Cretaceous period as part of the continued opening of the Atlantic Ocean and Gulf of Mexico (Eby and Vasconcelos, 2009; Guccione, 1993; Van Gosen and Choate, 2021). According to work completed by Mead (1915), Stearn (1930), and Bramlette (1932), nepheline syenite was the parent rock for bauxite development. The nepheline syenite remained a topographic high in places creating syenite plateaus that were above sea-level, providing an environment conducive for bauxite formation (Geology of Arkansas 2020; Guccione, 1993; Valeton, 1972). The syenite domes were walled by layers of sediments spanning from the Midway Group of the Paleocene to deposits from the Pleistocene (McFarland, 2004; Valeton, 1972; Van Gosen and Choate, 2021; Figure 7). The Midway Group was represented by stratified marine sediments and had an unconformable boundary separating it from the nepheline syenite below (Bramlette, 1932; Gordon, et al., 1958; McFarland, 2004). Due to the topographic high of the nepheline syenite domes, Midway Group deposition from the seaway did not reach the upper portions of these raised areas (Bramlette, 1932). Following this period of weathering, the Wilcox Group was deposited unconformably above the Midway Group during the Eocene (Gordon et al., 1958; McFarland, 2004). The Wilcox Group is composed of a series of non-marine sands, clays, and gravels with areas of thick lignite deposits (McFarland, 2004). It was

subdivided into three formations including the lower Berger Formation, middle Saline Formation and Detoni Sand (Gordon et al., 1958; Figure 7).

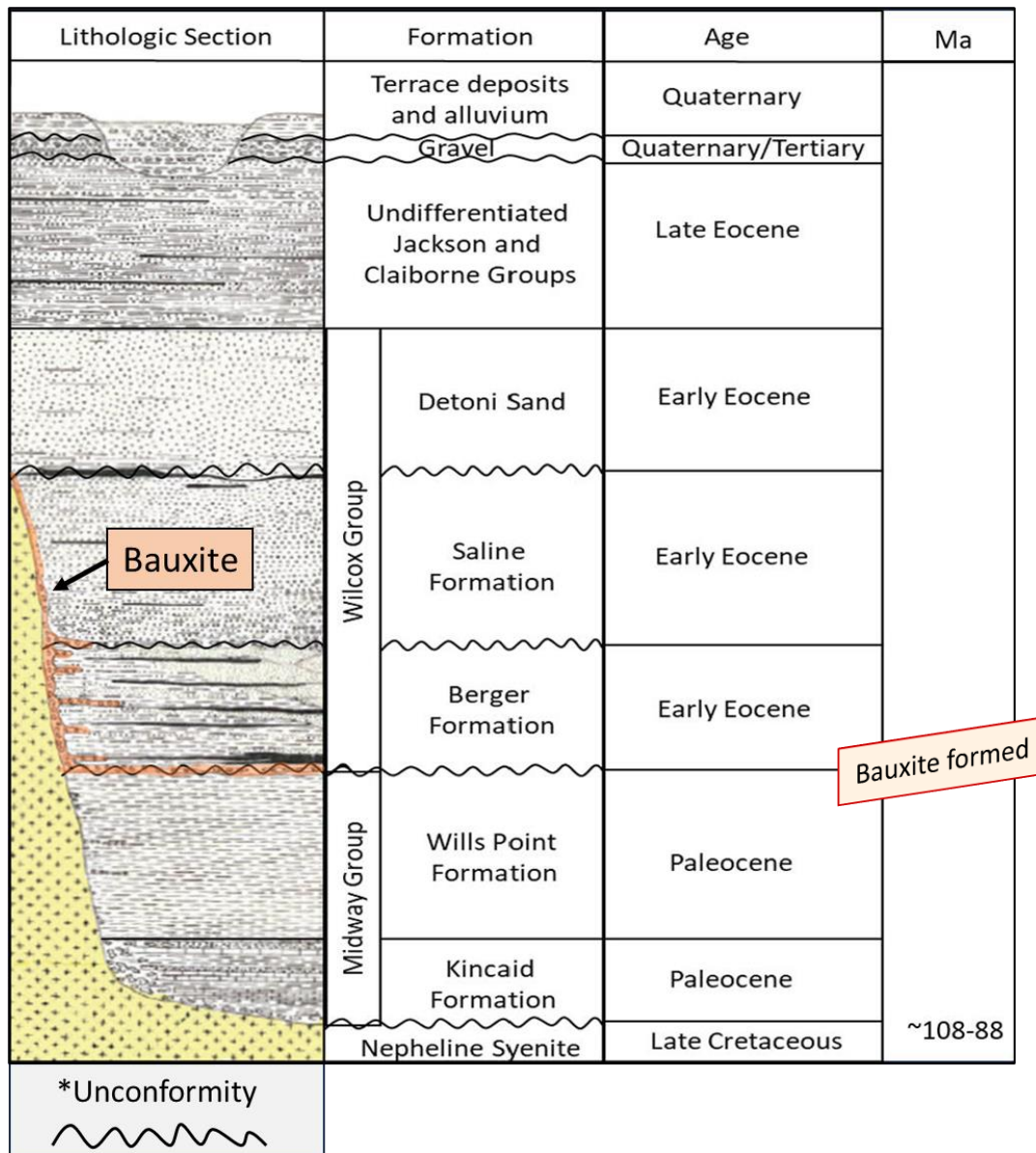


Figure 7: Summarized stratigraphic column for the bauxite district in Saline County, Arkansas (modified from Gordon et al., 1958). Bauxite formed primarily in the Wilcox Group during the Early Eocene (Gordon et al., 1958).

## Paleo-Physiography/Climate

Gordon et al. (1958) researched the conditions that needed to be met in order for bauxitization to occur: a constant source of water and warm temperatures throughout the year (not so warm to cause extended evaporation, but warm enough for microflora to dominate); percolation of rainwater through rocks with high aluminous content; rocks situated on elevated terrain to allow for moderate, but not extensive leaching; a water table that flowed unencumbered below the rocks; and time for all the previous stated factors to form bauxite. These conditions created an environment that favored the development of Oxisols; highly weathered soils that are rich in iron (Fe) and aluminum (Al) oxide minerals. Erosion and weathering obscured many of the soil processes that were present during the Eocene, however, similar soils favorable to bauxite development can be studied in the more recent deposits of Costa Rica, Hawaii, Fiji, and the British Mandated Solomon Islands (Valeton, 1972). In addition to Gordon et al. (1958), Guccione (1993) and Valeton (1972) also concluded that a tropical or subtropical environment was needed for bauxite development.

## Hydrogeology (Surface and Subsurface)

The bauxite region is located within the West Gulf Coastal Plain region of central Arkansas and is bordered by the Arkansas River to the north and east, with flow patterns to the south, and the lesser Saline River to the west, flowing predominately

southward from the area (Gordon et al., 1958). More proximal to the study area, smaller surficial streams including Hurricane Creek - southeasterly flow, Holly Creek - southwesterly flow, and Dry Lost Creek - southward flow, are tributaries to the Saline River and responsible for the primary drainage nearby (Haley et al., 1993; Plebuch and Hines, 1967). This area is part of the Little Hurricane Creek-Hurricane Creek watershed within the greater Upper Saline watershed (Arkansas Natural Resources Division, 2006; Figure 8). Due to the low relief in the coastal plain, migration of water in the surficial streams have little communication with ground waters (Guccione, 1993; Plebuch and Hines, 1967). McGeorge Contracting Company has multiple retention ponds in the mining area to capture water runoff within the reclamation site.

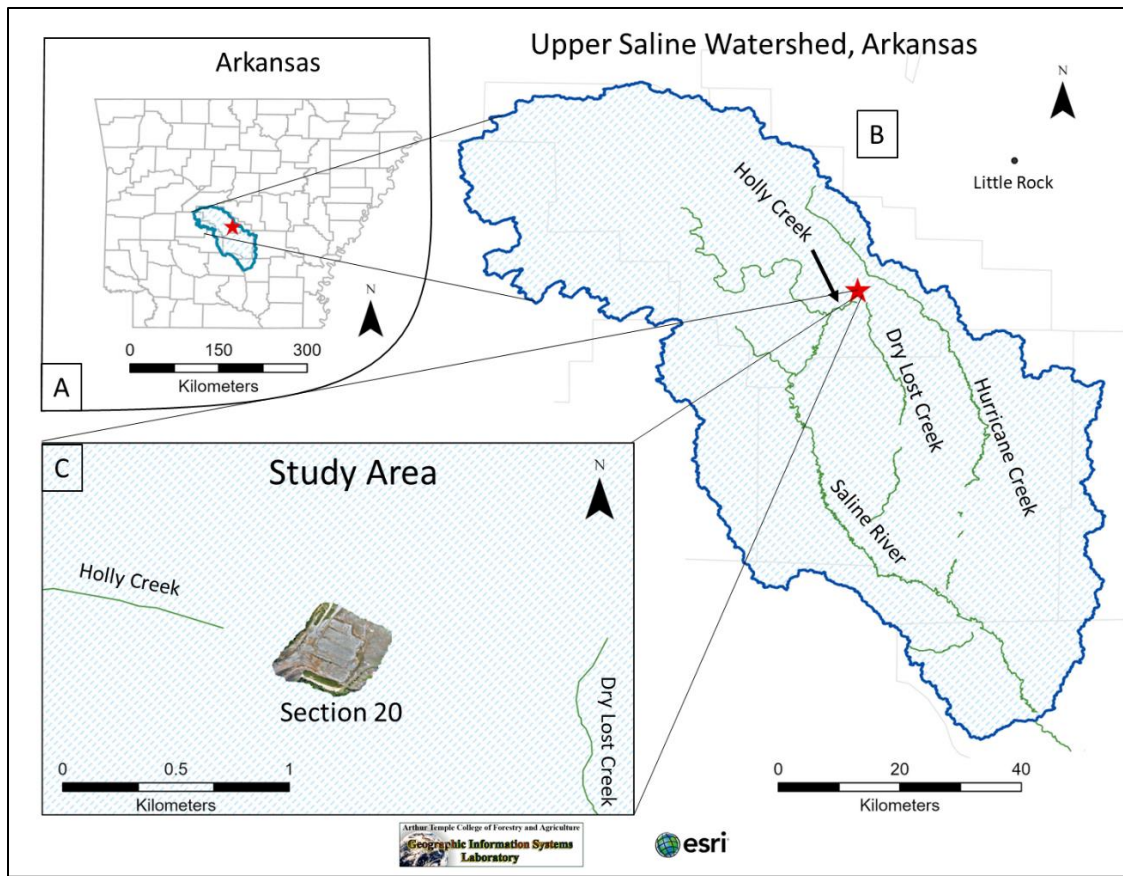


Figure 8: Map of Arkansas (AR) showing Upper Saline watershed boundary with study Bauxite, AR denoted by red star (A). Enlarged view of Upper Saline watershed depicting creeks and rivers near Bauxite, AR (B). View of study area with image of Section 20 overlayed showing proximity to nearby creeks (C) (data from U.S. National Atlas, 2015; Bureau, U.C., 2021; USDA, 2012; USA rivers and streams, 2004).

## Soils

Valeton (1972) and Gordon and Murata (1952) described regolith profiles to better recognize the processes of soil formation and their relationship to bauxite deposits. They found primary bauxite deposits were dominated by a regolith that contained a zone of concretion and zone of leaching (Gordon et al., 1958; Valeton, 1972). Within the zone of leaching, a portion of bauxite, predominantly gibbsite ( $\text{Al}_2\text{O}_3 \cdot 3\text{H}_2\text{O}$ ), retained the granite-like structure from the underlying nepheline syenite (Gordon et al., 1958; Valeton, 1972; Wysor and Fermor 1916). At present, the soils surrounding the site are considered Udorthents, representing an area where the original soil has been removed, covered with a loamy fill material, and graded to a smooth surface (Soil Survey Staff, 1999). Belonging to the soil order and suborder of Entisols and Orthents respectively, these soils are young, widely distributed, fairly resistant, and lack significant profile development (Soil Survey Staff, 1999).

## Geochemistry and Mineralogy

Weathering of the nepheline syenite rocks and associated clays provided the parent material needed to develop bauxite. Chemical weathering and pedogenetic processes have been responsible for creating an environment in which the silica and associated minerals (Na, K, Ca, Mg) were leached while hydrous oxides (Al, Fe, and Ti) remained (Gordon et al., 1958). Primary hydrated aluminum oxides come in the form of

gibbsite, boehmite ( $\text{Al}_2\text{O}_3 \cdot \text{H}_2\text{O}$ ), and dimorphic (different crystal structure) diaspore ( $\text{Al}_2\text{O}_3 \cdot \text{H}_2\text{O}$ ) (Gordon et al., 1958; Valeton, 1972). “Bauxite” is a collective term that includes the aforementioned aluminum hydrates, though gibbsite was frequently the main hydrate in commercial deposits (Wysor and Fermor, 1916). Textures can be coarse-grained (granite-like), reflecting the parent nepheline syenite material, pisolithic (birdseye, oolitic, or vermicular), typically identified by the various sized concretions within the ore, and massive presenting as a structureless clay-like material (Bramlette, 1932; Gordon et al., 1958; Wysor and Fermor, 1916; Figure 9). Pisolithic bauxite was the most dominant type observed while in Section 20. Within the chambers of the rock, clasts/nodules were either present or a mold formed where one once was. The clasts/nodules were spherical and typically ranged between 0.5 to 1 centimeter (cm) (Figure 10).



Figure 9: Images displaying different textures of bauxite: (A) granite-like (from Encyclopedia Britannica, 2022), (B) pisolithic (from Van Gosen and Choate, 2021) and (C) massive (from SHE Media collective, 2022).



Figure 10. Image of various sized clasts found within pisolithic bauxite at Section 20 mine Bauxite, Arkansas.

Goldschmidt (1937) used ionic potential to describe how elements should react in solution, relating it to the size of lattice structure within the minerals of the rock. He did this by using a ratio of the ionic radius versus charge and grouping elements into cations, soluble complex anions, and hydrolysates (Goldschmidt, 1937). Goldschmidt went further to say that basic oxides and complex anions that do not adhere to the ionic potential range of hydrolysates stay in true ionic solution and consequently are likely removed from sediments via chemical weathering processes. Those elements that remained within the hydrolysates range, if present, would potentially remain in the bauxites as soil solution disseminated through the subsurface (Goldschmidt, 1937; Gordon and Murata, 1952; Figure 11). Outliers do exist with regards to Goldschmidt's theory; elements such as copper (Cu), lead (Pb), manganese (Mn), and beryllium (Be) were found in the Arkansas bauxites, and are discussed in detail by Gordon and Murata

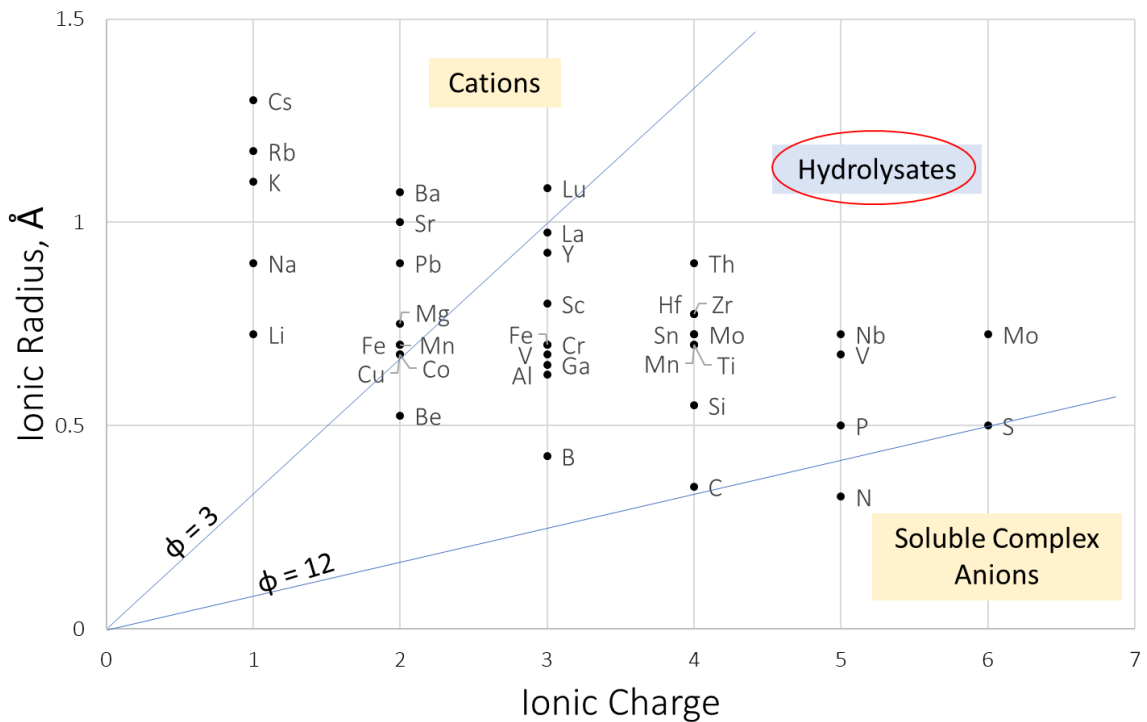
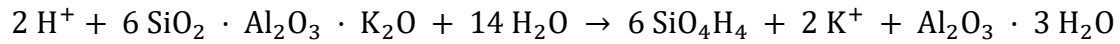


Figure 11: The ionic potential ( $\phi$ ) of elements represented in this chart. The lines separating each group by ionic potential were derived by V.M. Goldschmidt (1937). Cations represent the group above the ionic potential of 3, soluble complex anions below the ionic potential of 12, and hydrolysates (circled in red) is between the cations and soluble complex anions (Gordon and Murata, 1952). Hydrolysates are likely to be enriched and precipitate from solution while the other groups remain in true ionic solution, thus removed from the system (Gordon and Murata, 1952). Ionic radii data for this graph from Bugaenko et al. (2008). Element symbols: Cs – cesium, Rb – rubidium, K – potassium, Na – sodium, Li – lithium, Ba – barium, Sr – strontium, Pb – lead, Mg – magnesium, Fe – iron, Mn – manganese, Co – cobalt, Cu – copper, Be – beryllium, Lu – lutetium, La – lanthanum, Y – yttrium, Sc – scandium, Cr – chromium, V – vanadium, Ga – gallium, Al – aluminum, B – boron, Th – thorium, Hf – hafnium, Zr – zirconium, Sn – tin, Mo – molybdenum, Ti – titanium, Si – silicon, C – carbon, Nb – niobium, P – phosphorus, N – nitrogen, S – sulfur.

(1952). Aluminum, iron (Fe), titanium (Ti), and other minor accessory elements have been observed in the bauxite deposits in Saline County (Gordon et al., 1958). Valeton (1972) reported distinct phases of Arkansas bauxite formation to help explain the various minerals; during the initial phase of bauxite formation, gibbsite was produced from existing feldspars present in the granite-like regolith, with oxides and accessory minerals in this phase (Gordon et al., 1958; Valeton, 1972; Equation 1). Following the formation of gibbsite and clays, along with the leaching of the more soluble elements, diagenetic processes led to concentric spheres (pisolites) to develop during burial (Gordon et al., 1958; Valeton, 1972). Gordon et al. (1958) described gibbsite cross-cutting previous structures among the bauxite and suggested that hydrous aluminum oxides recirculated after bauxite development. Sediments deposited from the Paleocene to the Quaternary likely supplied silica to the underlying bauxite and created an environment conducive to kaolinitic clay formation (Goldman, 1955; Valeton, 1972; Equation 2). As soil solution and pressure increased from sedimentation above, bauxite was then silicified again and kaolinitic clays filled cavities, fractures, and at times even replaced bauxite; reduction of ferric iron is also noted, represented by the development of siderite and pyrite (Goldman, 1955; Valeton, 1972). The geochemical formulas below show the hydrolysis reactions for feldspar to gibbsite, feldspar to kaolinite, and kaolinite to gibbsite (Valeton, 1972; Equations 1-3):

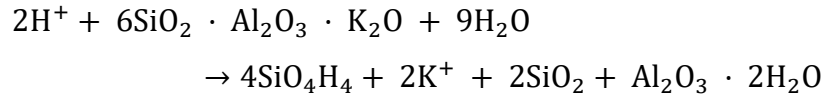
Equation 1:

Feldspar → Gibbsite:



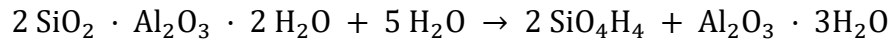
Equation 2:

Feldspar → Kaolinite:



Equation 3:

Kaolinite → Gibbsite:



Common minerals identified in Arkansas bauxite are gibbsite, diaspore, boehmite, kaolinite ( $\text{Al}_2\text{Si}_2\text{O}_5(\text{OH})_4$ ), siderite ( $\text{FeCO}_3$ ), hematite ( $\text{Fe}_2\text{O}_3$ ), goethite ( $\text{FeO(OH)}$ ) and ilmenite ( $\text{FeTiO}_3$ ), and although this list is not exhaustive, it does reflect many of the minerals that have been created from these processes (Goldman, 1955; Gordon et al., 1958; Proctor et al., 1991; Valeton, 1972).

## **OBJECTIVES**

The focus of this study was to identify the primary suite of economic and environmentally sensitive elements that occur in bauxite stockpiles. These objectives include:

1. Identifying and delineating the volume of the existing bauxite stockpiles using an unmanned aerial vehicle (UAV).
2. Analyzing samples of bauxite from each stockpile in Section 20 for element content and concentration using x-ray fluorescence and laser ablation – inductively coupled plasma – mass spectrometry.
3. Evaluating the elemental enrichment of Arkansas bauxite stockpiles compared to background elemental concentrations of the upper continental crust and the National Institute of Standards and Technology (NIST)-698 (Jamaican bauxite standard).
4. Evaluating elemental correlations with respect to aluminum, iron, and titanium content using scatter plot analyses for all five stockpiles in Section 20.
5. Examining the relationships between bauxite stockpile characteristics and potential mobilization of soluble elements using spatial analytical techniques.

## **SIGNIFICANCE**

These stockpiles contain low-grade aluminum ore rock and are currently not economically viable as aluminum ore but may contain important minerals that could be exploited for other purposes. The chemical characteristics of each stockpile may provide understanding to elemental patterns and metal affinities within bauxite ores. The identity and concentration of economic and environmentally sensitive elements within the bauxite stockpiles could provide economic resources for the future, as demand for critical minerals continues to increase over time. In addition to critical minerals, gaining insight about mineral transformations or translocations over time within the bauxite piles would likely benefit future reclamation efforts.

## **METHODOLOGY**

### Unmanned Aerial Vehicle (UAV) Survey

Permission to fly a UAV in Section 20 was granted by a liaison of McGeorge Contracting Company. The area of interest for the flight was an open field with trees around a portion of the perimeter and lacked powerlines. Tree heights were measured with the drone prior to survey to verify safety of aircraft. Section 20 is not an active mining site and workers were not present in the flight area during survey. Hard hats, high visibility safety vests, and safety glasses were used as personal protective equipment. A visual observer was present in addition to the remote pilot.

A DJI Mavic Pro 2 unmanned aerial vehicle quadcopter was used to survey five stockpiles to obtain images and spatial data for volume analysis. The UAV weighed two pounds and was equipped with GPS+GLONASS to capture geo-referenced images and direction of the UAV during capture. The Map Pilot Pro app was used for planning and controlling the flight missions. A minimum of 13 satellites, with an average of 16, were employed to capture positional data at the time of flight. Due to limitations of lithium battery charge, a total of four flights were conducted to complete the survey. The survey began on May 2, 2023 at 12:47 p.m. and was completed at 2:04 p.m. on the same day. Weather was cloudy with winds less than five miles per hour (mph) for the

duration of the survey. The UAV was set for a fly height of 44 m above ground level with along track and across track overlap both at 75%. Max speed during flight was 15.54 m/s. Drone specifications and flight data can be found in Appendix B.

#### UAV Image Processing

A total of 1367 images captured from the UAV of the Section 20 flight were imported into ArcGIS Pro and processed by Drone2Map to generate an orthorectified image, digital elevation model (DTM), and digital surface model (DSM). The orthorectified image was composed of multiple georeferenced images that were stitched together to form a single image with 1 cm resolution (Figure 12). A DSM (Figure 13) was recommended and used for volume measurements because it reflects the elevation of all structures above the ground, whereas a DTM only measures the elevation of the ground (Image Mensuration, 2023). Heights were calculated relative to the takeoff location of the drone, usually ground control systems would be used to communicate with the drone during flight for position but those were not available for this study. McGeorge Contracting Company was unable to verify volumes of stockpiles therefore two methods were used for comparison and validation of data. Two software programs, ArcGIS Pro and QGIS, were used to analyze stockpile volume using the DSM. Both software programs allow for spatial analysis and mapping but an important

distinction between the two is that ArcGIS Pro is a commercial software while QGIS is open source.

## Orthorectified Image

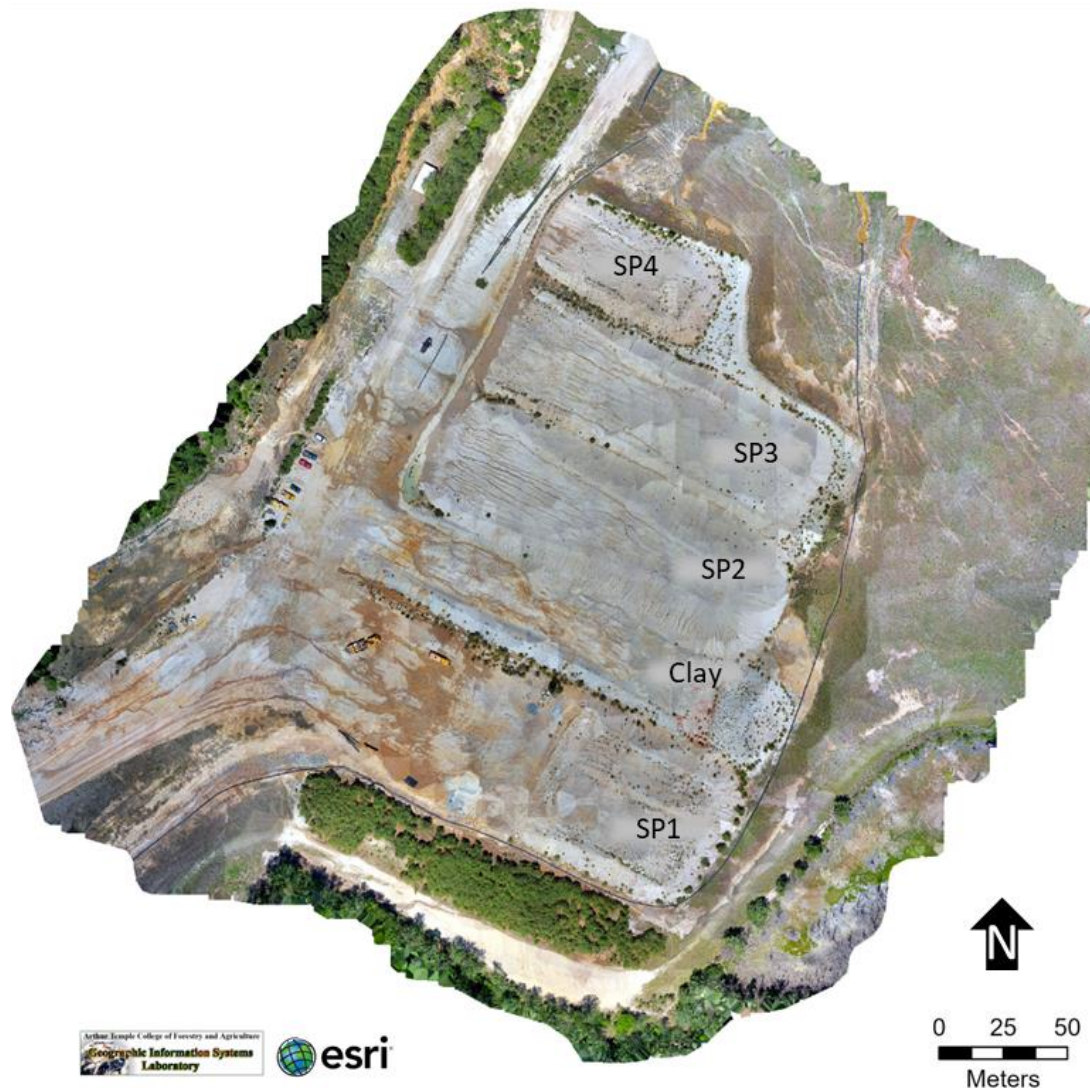


Figure 12: Orthorectified image of Section 20 mine area using ArcGIS Pro.

## Digital Surface Model (DSM)

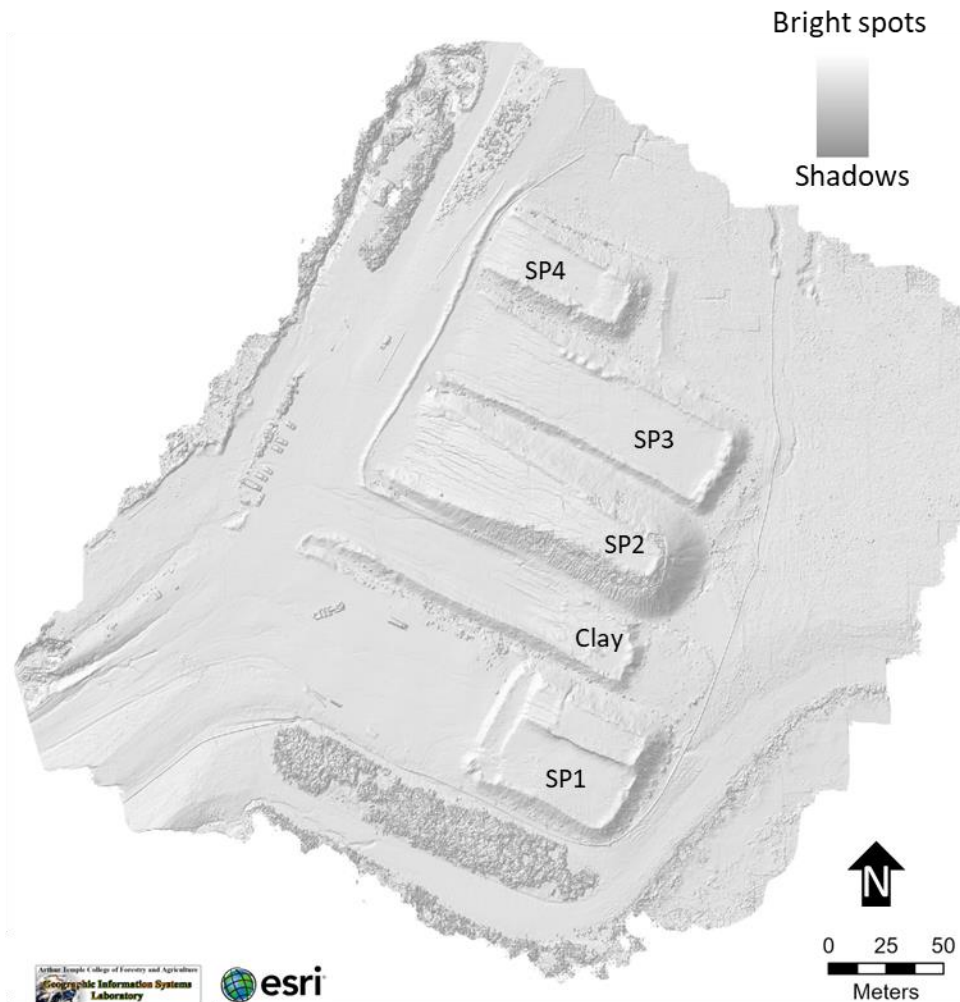


Figure 13: Digital surface model (DSM) for Section 20 mine area to illustrate land surface using ArcGIS Pro. Hillshade is scaled from dark gray (shadows) to white (bright spots).

## Volume Measurement – ArcGIS Pro

The workflow for volume analysis using ArcGIS Pro was obtained from the ESRI – ArcGIS Pro documentation (Image Mensuration, 2023). A DSM and orthorectified image were uploaded into an ArcGIS Pro map using a projected coordinate system of World Geodetic System (WGS) 1984 Universal Transverse Mercator (UTM) Zone 15N. Imagery tab was selected to display the Mensuration section and expanded to see Mensuration options. In the Mensuration option, Volume (in cubic meters) was selected with a precision level of four. Symbols were left on default settings and the DSM file of Section 20 was selected as the elevation source. The base surface was set to Interpolate; where the feature creates a base surface by interpolating elevation from the DSM by selecting points surrounding the feature (Image Mensuration, 2023). Under the mensuration section, volume was selected, then a polygon was drawn around the stockpile of interest using marked vector points (Figure 14). Vector points were used to overlay the DSM to ensure the polygon for each stockpile in both software programs were in the same location, to minimize human error. After selection was complete, the results tab within Mensuration section was selected and cut volume was recorded. Cut volume reflects the volume only above the base surface. Figure 15, provides an overview of workflow of the process using ArcGIS Pro.

## SP4 polygon with control points



Figure 14: View of polygon (in yellow) encircling stockpile SP4 using control points for volume calculation in ArcGIS Pro.

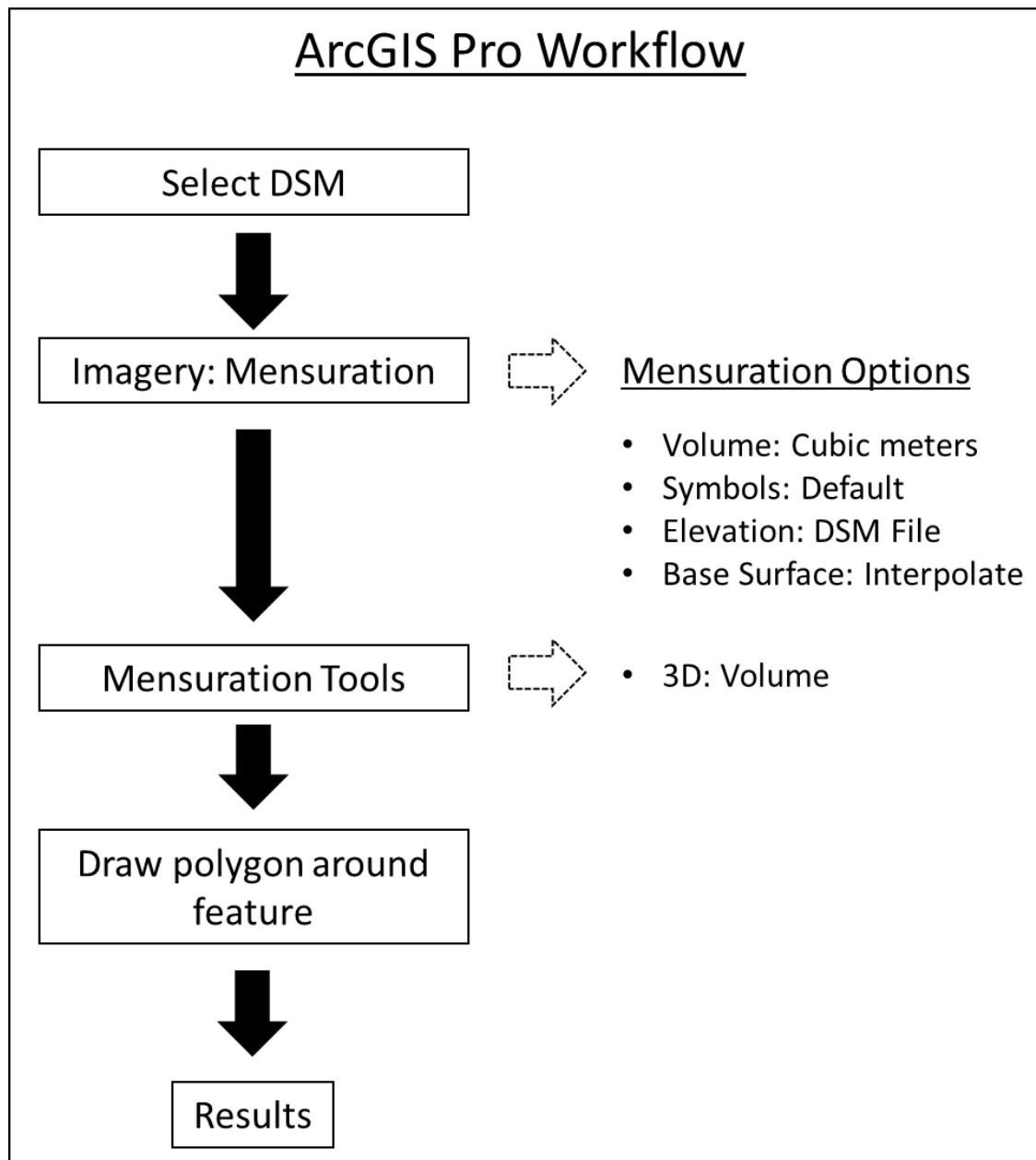


Figure 15: ArcGIS Pro workflow for calculating volume of a stockpile with digital surface model.

## Volume Measurement - QGIS

The workflow for volume analysis using QGIS required more steps which are discussed in this section. A DSM and orthorectified image were uploaded into QGIS using a projected coordinate system of WGS 1984 UTM Zone 15N. A temporary multi-surface polygonal scratch layer was generated using the same spatial reference system as the DSM (Figure 16). With the new scratch layer highlighted, the stockpile of interest was digitized by selecting control points encircling the stockpile of interest. The drape tool, utilizing the DSM raster layer, was used to add elevation to the digitized section. An interpolated base surface was generated by using the triangulated irregular network (TIN) based on control points where each point attained its elevation from the DSM (Figure 17). Subsequently, the TIN was converted to a raster data for a raster calculation against the DSM. Using the raster calculator tool, the DSM raster layer was subtracted from the TIN interpolated base surface layer to create a new layer showing elevation difference (Figure 18). This layer represented the difference in height for each pixel value in the raster layer. The raster layer zonal statistics tool was run on the elevation difference raster layer generating a new table showing the raster zones and associated statistics. Raster zones reflects areas of raster cells which share the same values (elevation difference) and are grouped together. In the resulting table, the field “m<sup>2</sup>” represents the area for each raster zone and “sum” is the collective elevation difference

## Temporary polygon layer

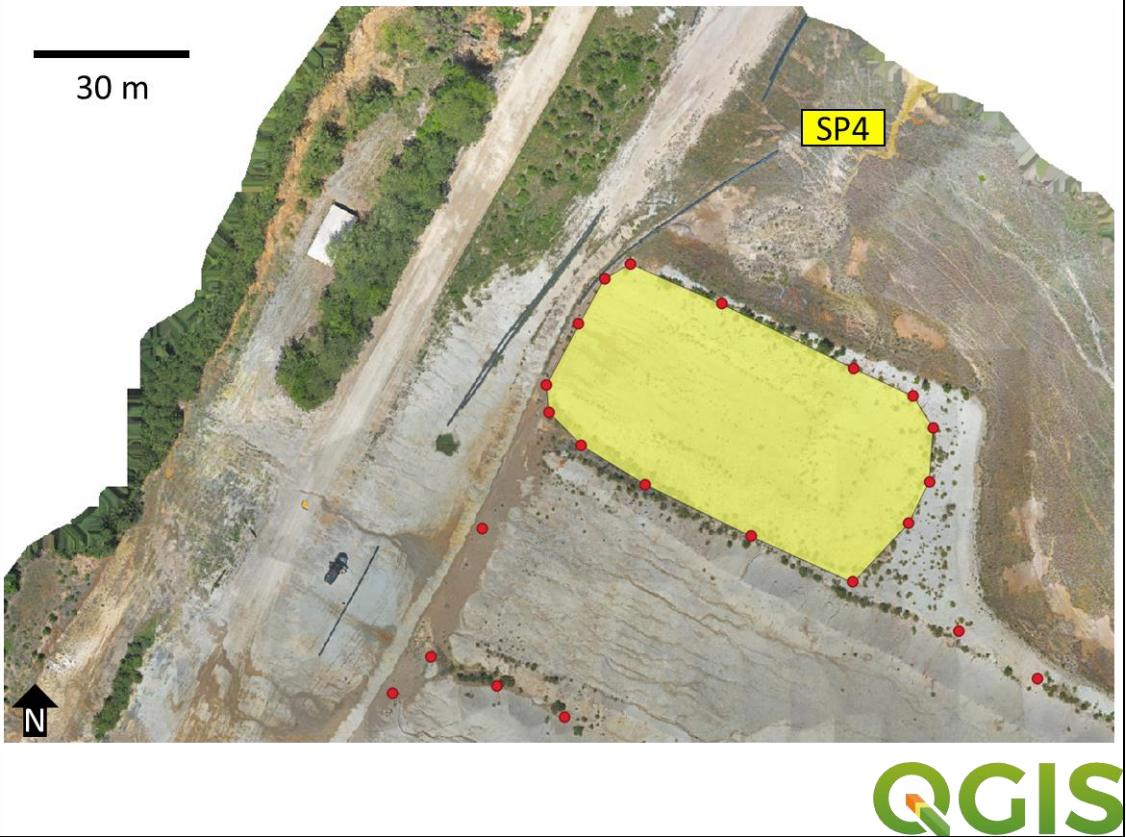
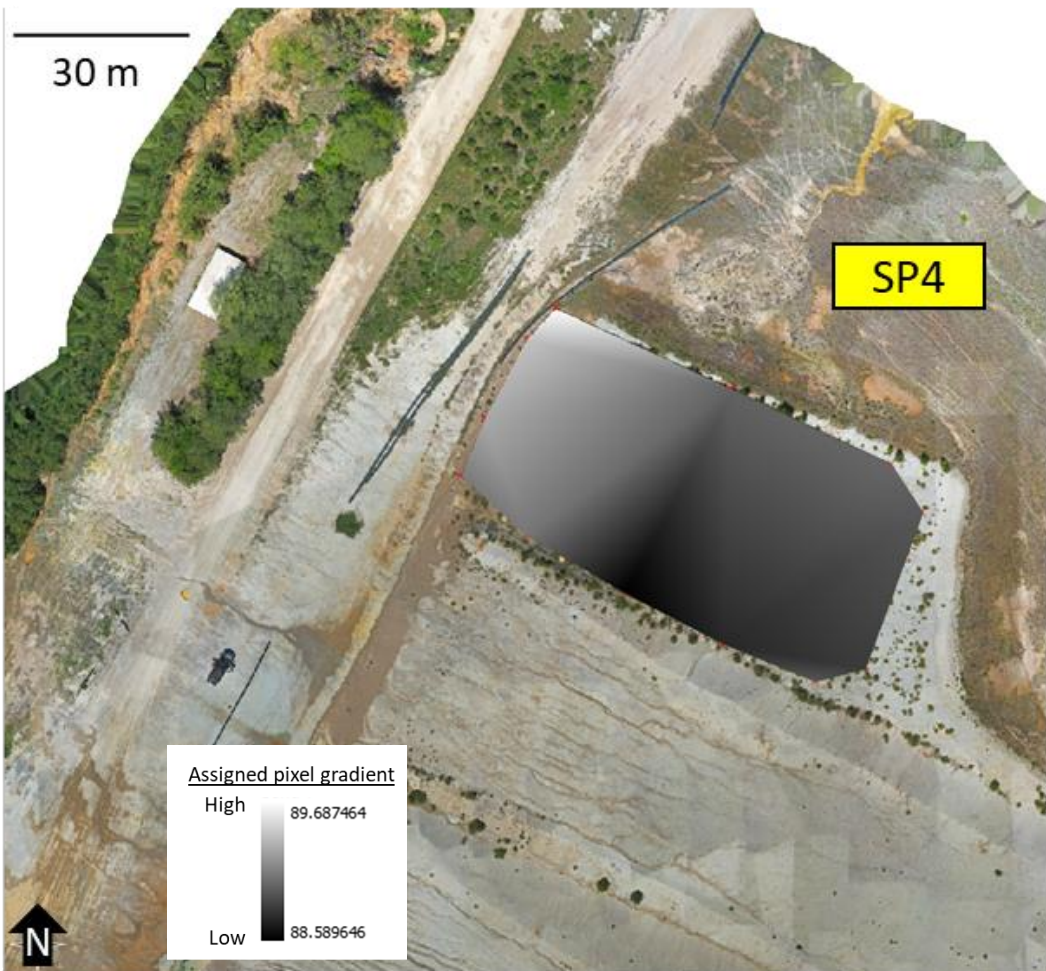


Figure 16: A temporary multisurface polygon (in yellow) layer that will be used with drape tool and applied during QGIS processing for volume analysis.

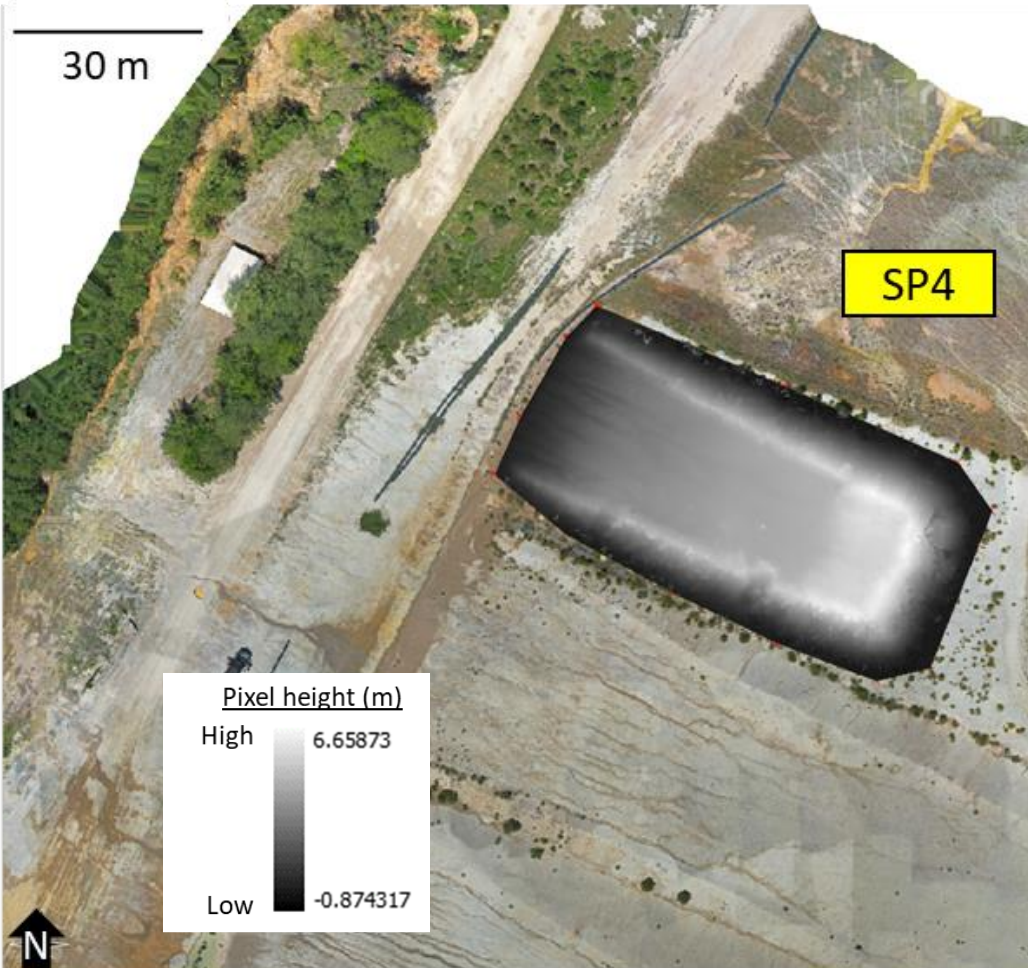
## Interpolated base surface layer



**QGIS**

Figure 17: View of interpolated base surface layer after edges were averaged and smoothed during QGIS processing for volume analysis.

## Elevation difference layer



**QGIS**

Figure 18: Layer showing elevation differences for each pixel value in the raster layer during QGIS processing for volume analysis.

or all the raster cells in a specific zone. Count values represent a single zone and values greater than one would increase the area, for example, if a count was 2, it would double the area, leading to gross overestimation of the calculated volume. Sum values below zero were excluded to calculate only cut volume. The “sum” and “m<sup>2</sup>” values in the attribute table were multiplied using the field calculator which provided the volume for each raster zone. A new output field was generated during the calculation. Once complete, the volume of the stockpile was viewed under “sum” statistic of the new output field. Figure 19 provides an overview of workflow of the process using QGIS.

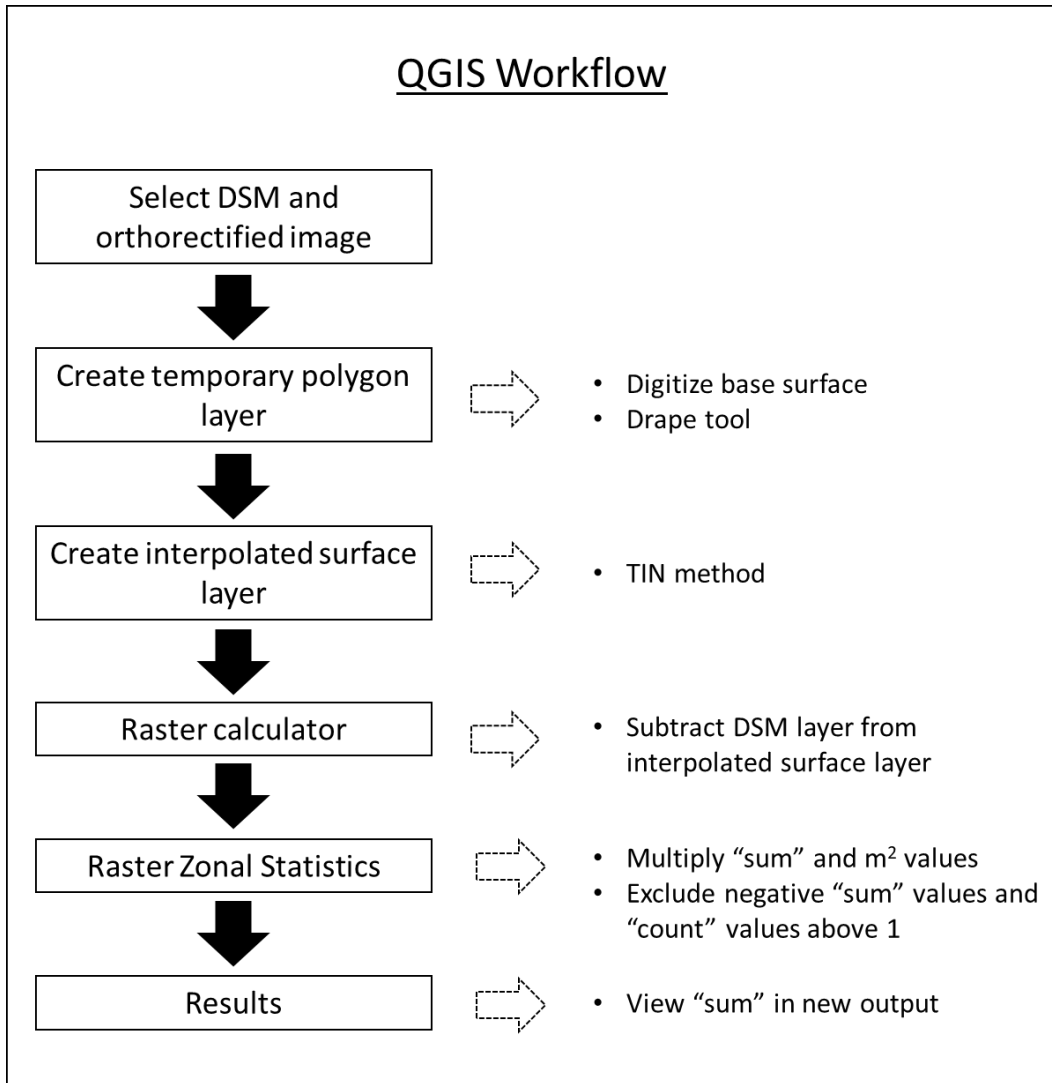


Figure 19: QGIS workflow for calculating volume of stockpiles with digital surface model (QGIS, 2018).

#### Accuracy Assessment of Stockpile Volumes

Upon completion of image processing, all five stockpiles were measured individually, ten times per software application. An independent t-test, two-sample

assuming unequal variances, was used to assess if the differences between software applications were statistically significant (Laerd Statistics, 2016a). A 95% confidence interval was used for the results, showing a range of values on either side of the mean that would be generated 95% of the time if the process was repeated. This test was conducted by using the data analysis tool within Microsoft Excel and confidence intervals were provided by Dr. Greg Miller from the Department of Mathematics and Statistics at Stephen F. Austin State University.

In addition to the independent sample t-test, the percent difference was calculated (Equation 4) by averaging the ten measured volumes for each of the five stockpiles within each software application.

Equation 4:

$$\text{Percent difference (\%)} = \left( \frac{| \text{open source volume} - \text{commercial source volume} |}{\frac{\text{open source volume} + \text{commercial source volume}}{2}} \right) * 100$$

#### Rock Sample Collection

One-hundred twenty-eight (128) rock samples were collected from five stockpiles in Section 20 of the former ALCOA mine in Bauxite, Arkansas. Samples from SP1, SP2, SP3, and SP4 were collected 20m apart while samples from the Clay stockpile were 10m apart to accommodate for the difference in stockpile size. Samples were

collected at 30cm beneath the surface around the base of the pile and along the incline (Figure 20), Appendix C provides images of the stockpiles in the study area with numbered sample locations. Equipment used to obtain samples included an Estwing rock hammer, steel spade, permanent marker, Ziploc bags, gloves, and safety glasses. Each location was marked with a GPS coordinate at the time of collection.

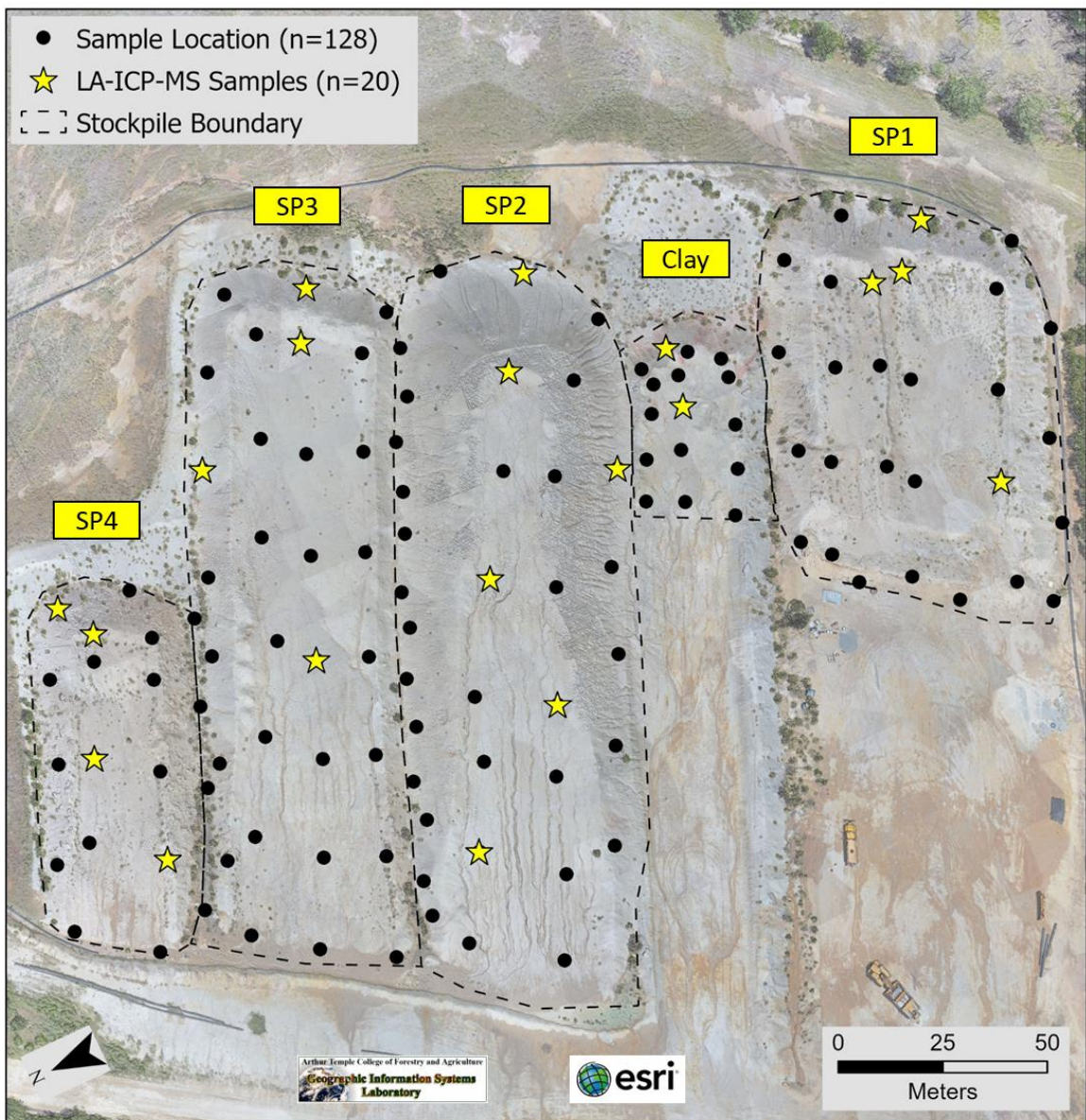


Figure 20: Orthorectified image of Section 20 stockpiles with sample collection locations represented by black dot. Samples with yellow star were sent for LA-ICP-MS analysis in addition to being analyzed by XRF. Appendix C provides numbered sample locations.

### X-Ray Fluorescence (XRF)

Elemental analyses were performed using the Thermo Nitron XL3t GOLDD+ XRF handheld analyzer on samples collected from each of the five stockpiles in Section 20. A total of 128 bauxite rock samples were analyzed along with the NIST-698 (Jamaican bauxite standard) sample. In addition to the rock samples, clasts and matrix material from each stockpile were separated and tested individually. All samples were crushed using a mortar and pestle then sieved through a 250-micron ( $\mu\text{m}$ ) filter (Figure 21). Approximately 10 grams of each crushed sample was stored into a sample bag and labeled with sample ID and weight in grams (g). Approximately 5g of each sample was packed into an XRF sample cup (Series 1500) covered with 0.4  $\mu\text{m}$  polypropylene x-ray film and charged by a cotton ball to fill any void space (Figure 21).

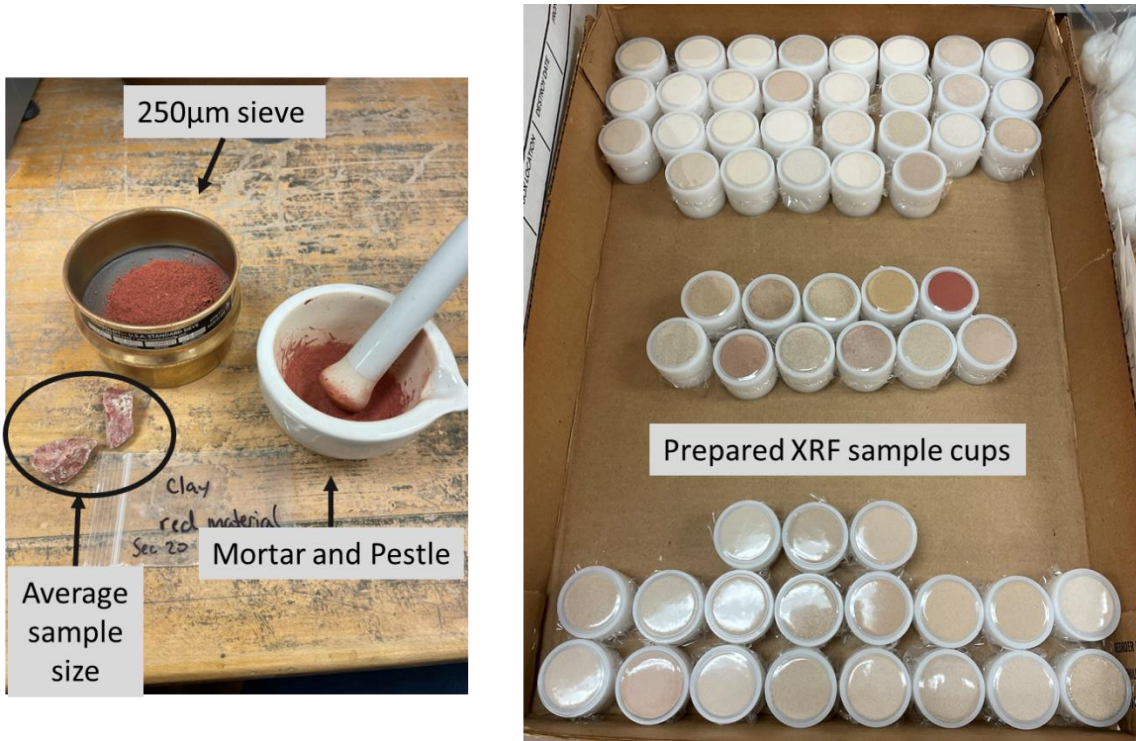


Figure 21: Example of sample size, mortar and pestle and 250-micron sieve (left). Sample cups prepared for XRF analysis (right).

Using the “Test All Geo Mode” of the Thermo Nitron handheld analyzer, samples were scanned for a total of 5 minutes per sample (30 seconds each for main, low and high range filters, and 180 for light filter). Each sample was scanned three times and an average was calculated in an attempt to reduce error stemming from the heterogeneity of bauxite. Elements that were able to be tested for in the “Test All Geo Mode” can be found in Figure 22. Once all samples were analyzed, results were downloaded from the Thermo Nitron analyzer into a Microsoft Excel spreadsheet for data analysis.

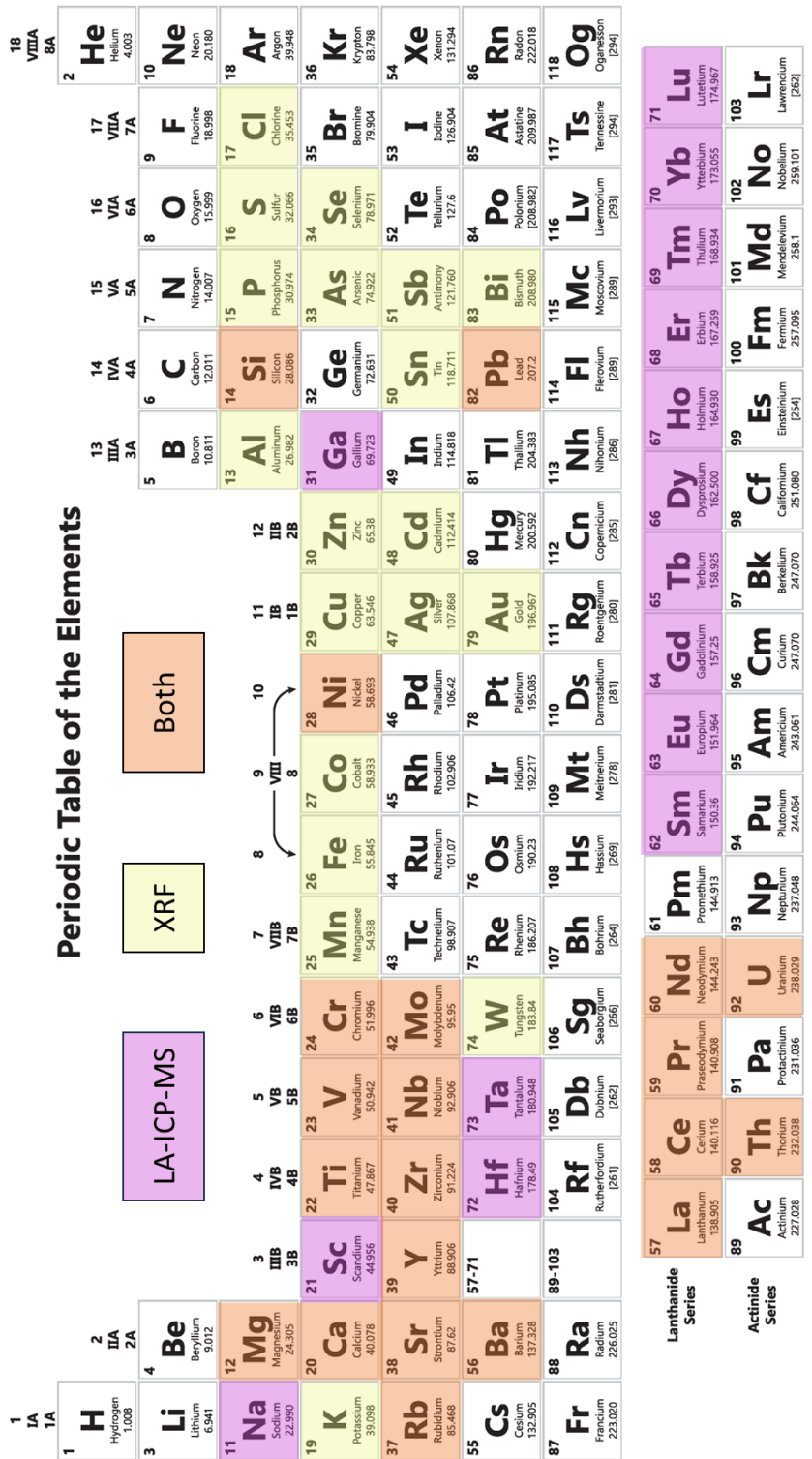


Figure 22: Reported elements using Thermo Niton XL3t GOLD+ portable XRF (yellow) and from Texas Tech GeoAnalytical Laboratory LA-ICP-MS (purple). Elements reported in both analytical methods (peach). Modified from (Helmstine, 2017)

## Laser Ablation – Inductively Coupled Plasma – Mass Spectrometry (LA-ICP-MS)

A total of twenty bauxite samples along with the NIST – 698 (Jamaican bauxite standard) sample were sent to Texas Tech GeoAnalytical Laboratory for LA-ICP-MS analysis. LA-ICP-MS is a method where a laser beam interacts with the surface of a prepped sample causing particles to be released (LA); those particles are then transported through the machine for rapid elemental and isotopic analysis (ICP-MS) (Woodhead et al., 2007). The methods of Paton et al. (2011) and Woodhead et al. (2007) were applied to obtain the quantity of trace elements of a solid material.

Elements that were detected in the samples using LA-ICP-MS can be found in Figure 22.

For fusions, a total of  $1.2000 \pm 0.0010$  grams of powdered sample was combined and mixed with  $4.8 \pm 0.0010$  grams of 49.75% Li-metaborate/49.75% Li-tetraborate/0.50% Lithium Bromide (LiBr) flux in a platinum crucible along with 40  $\mu\text{L}$  of Li Iodide solution. The platinum crucible was then heated using a M4 Fluxer for 13 minutes to create a melt. The melt was then poured into a platinum mold to create a glass disc. To complete the analysis, fused glass discs of the samples were made.

Each of the fused glass discs were analyzed by LA-ICP-MS for trace element compositions using a New Wave 213 nm solid-state laser ablation system equipped with a 2-volume sample cell and an Agilent 7500cs quadrupole mass spectrometer. Approximately 30 seconds of background signal was collected prior to each ablation.

The glasses were ablated using a spot size of 80 µm, laser pulse rate of 10 Hz, and fluence of 7-8 J/cm<sup>2</sup> and sample aerosol was transported to the ICP-MS system using a He gas with a flow rate of 800 mL/minute. Count times were set to 0.005 for Na, Al, and Si, 0.01 for Cr and Ni, 0.015 seconds for Mg, Ca, Sc, Ti, V, Ga, Rb, Sr, Y, Zr, Nb, Mo, Ba, La, Ce, Pr, Nd, Sm, Pb, Th, and U, 0.02 seconds for Tb, Dy, Ho, Er, Tm, Yb, Lu, Hf, and Ta. The United States Geological Survey (USGS) standard GSD-1G was analyzed as the external calibration standard and BHVO-2G and NIST-698 sample were used for monitoring precision and accuracy. A total of 3-4 spots were analyzed from each of the glass discs and averaged. The percent relative standard deviation is better than 10% for each of the elements measured in BHVO-2G and NIST-698. The percent difference from known values of BHVO-2G are better than 5% for most elements and between 5-11% for Tb, Na, Zr, Y, Nb, Th, Tm, and Ta.

#### Statistical Analysis of Elements

Statistical analyses conducted in Microsoft Excel using both XRF and LA-ICP-MS were completed to establish the presence and quantity of elements among the bauxite stockpiles. All major element results were converted from weight percent to parts per million (ppm) for LA-ICP-MS values and referenced data (Conversion factors, 2002). A simple linear regression was used to establish the strength and direction of a linear relationship between XRF and LA-ICP-MS values from the samples collected.

Scatterplots were created to ensure a linear relationship (Figure 23) was present before using Pearson's correlation coefficient ( $r$ ) values. Pearson's correlation coefficient value range is from -1 to 1, values closer to 1 or -1 denote a perfect positive or negative relationship, respectively, whereas zero represents no relationship between the two techniques (Laerd Statistics, 2016b). For this study, ranges for Pearson's correlation coefficient values and corresponding meaning have been defined in Table 1.

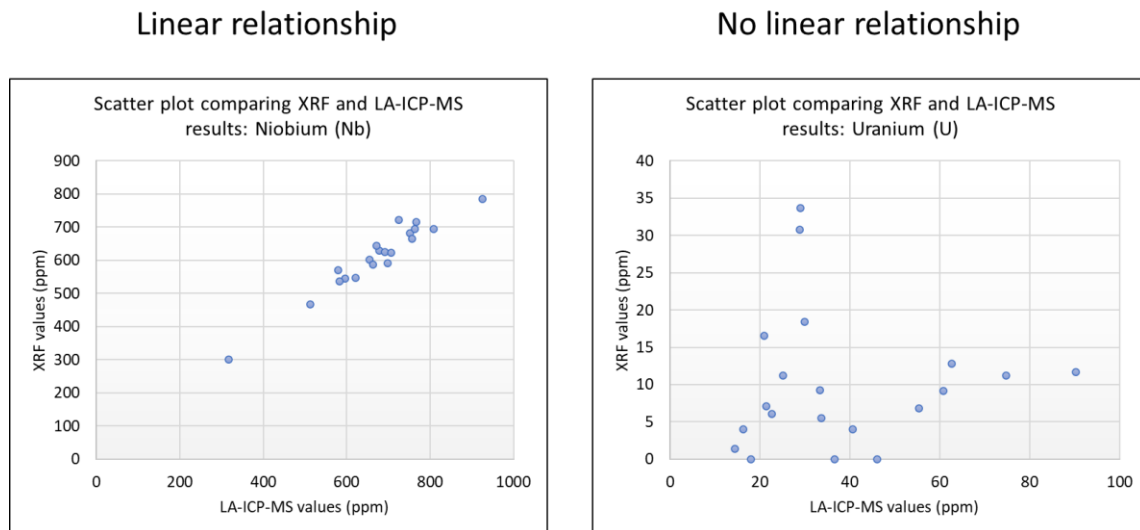


Figure 23. Examples of visually determined linearity used to evaluate if Pearson's correlation coefficient ( $r$ ) value could be used. If linear trend was present (left), correlation coefficient values could then be calculated. If a linear trend was not present (right), correlation coefficient values were not reliable, and therefore not calculated.

Table 1: Pearson's correlation coefficient values used for this study (LaMorte, 2021). Values closer to 1 or -1 reflect stronger correlations, positive or negative respectively, and values closer to 0 represent weaker correlations.

Pearson's correlation coefficient: $ r $	Correlation Description
1	Perfect
+0.8 to 0.99	Very strong
+0.6 to 0.8	Strong
+0.4 to 0.6	Moderate
+0.2 to 0.4	Weak
0 - 0.2	None

Scatterplots comparing XRF and LA-ICP-MS results for each element were used to establish a trendline, or line of best fit, to return an equation that was used for empirical calibration of the XRF data. Only elements where the trendline had a visible linear relationship on scatterplot and very strong or perfect Pearson's correlation coefficient values were used for empirical calibration. Microsoft Excel was used to compute the empirical calibration for each sample by inputting corresponding XRF values into "x" of the resultant equation, yielding a calibrated value.

The background concentrations of elements in the Earth's upper continental crust and the NIST – 698 sample were used as baselines to evaluate enrichment of elements within the Section 20 bauxite samples (Rudnick & Gao, 2014; Table 2).

Table 2. Values reported for background concentrations in Earth's upper continental crust and NIST-698 sample (Rudnick & Gao, 2014). For the NIST-698 sample, standard or LA-ICP-MS values were used if available, otherwise XRF values was used.

Baseline values (ppm) of continental crust and NIST-698 XRF values					
Symbol	Crustal Abundance	NIST-698	Symbol	Crustal Abundance	NIST-698
Mg*	24800	350 <sup>3</sup>	Sr	320	110 <sup>1</sup>
Al*	154000	255099 <sup>3</sup>	Y*	21	22
Si	666200	3225 <sup>3</sup>	Zr*	193	451.6 <sup>3</sup>
P	1500	1615 <sup>3</sup>	Nb*	12	24.5 <sup>1</sup>
S	621	573 <sup>3</sup>	Mo	1	13.4 <sup>1</sup>
Cl	370	0	Ag	53	1
K	28000	83 <sup>3</sup>	Cd	0.09	1
Ca	35900	4431 <sup>3</sup>	Sn*	2	3
Ti*	6400	14268 <sup>3</sup>	Sb*	0.4	1
V*	97	358 <sup>3</sup>	Ba*	624	71.6 <sup>3</sup>
Cr*	92	547 <sup>3</sup>	La*	31	32
Mn*	1000	2943 <sup>3</sup>	Ce*	63	300 <sup>3</sup>
Fe	50400	152353 <sup>3</sup>	Pr*	7	8
Co*	17	45 <sup>3</sup>	Nd*	27	28
Ni*	47	225 <sup>2</sup>	W*	2	3
Cu	28	46	Au	1.5	1
Zn*	67	233 <sup>3</sup>	Pb	17	29
As*	5	36	Bi*	0.2	1
Se	0.1	0	Th	11	12
Ga*	17.5	40.7 <sup>2</sup>	U	3	7.3
Rb*	84	2.2 <sup>1</sup>			

\*Critical element  
<sup>1</sup>Empirical calibration of XRF result using LA-ICP-MS data  
<sup>2</sup>LA-ICP-MS result  
<sup>3</sup>NIST-698 standard value

For LA-ICP-MS samples, Equation 5 was used to convey how many times greater the stockpile quantity was compared to the respective baseline value. For XRF samples, the percentage of enriched samples per each group (SP1, Clay, SP2, SP3, SP4, clasts, matrix) were calculated using Equation 6.

Equation 5:

$$\text{Percent Greater Value (\%)} = \left[ \left( \frac{\text{Baseline element value}}{\text{LAICPMS element value}} \right) - 1 \right] * 100$$

Equation 6:

$$\text{Enriched samples (\%)} = \frac{\text{number of enriched samples in stockpile}}{\text{total samples in stockpile}} * 100$$

Thereafter, sample data were separated by stockpiles, matrix, and clasts for individual elements that could be tested. Data, in parts per million (ppm), were compared to Fe, Ti, and Al for both XRF and LA-ICP-MS in ppm, again using the Pearson's correlation coefficient value only if a visual linear relationship via scatterplot was met prior. Al was excluded from LA-ICP-MS comparison because it was used as the internal standard to obtain LA-ICP-MS results. Fe results are rarely reported in LA-ICP-MS because values are typically high enough to measure using XRF. For this study, only values obtained from

LA-ICP-MS were compared to other LA-ICP-MS, therefore Fe was also excluded in the comparison.

### Spatial Distribution of Elements

Microsoft Excel tables of XRF and LA-ICP-MS data were uploaded into ArcGIS Pro. Points corresponding to each sample collection location were linked to corresponding elemental data from Microsoft Excel tables. Each sample collection site with associated elemental data were placed over a semi-transparent orthorectified image and DSM, using GPS coordinates with a projected coordinate system of WGS 1984 UTM Zone 15N.

Ordinary Kriging is a method of interpolation based on geostatistical models that use autocorrelation, a statistical comparison between measured points to create an estimated continuous surface layer reflecting the data extrapolated from each point (Raster Interpolation, 2023). This method was employed to view the spatial distribution of elements that had strong, very strong, or perfect correlation coefficient values when compared with LA-ICP-MS values. Ordinary Kriging is the most common method and assumes the constant mean is unknown (Raster Interpolation, 2023). The Kriging tool uses a statistical model among a specified number of points in a radius to determine the output for each location (Raster Interpolation, 2023). The geostatistical method Kriging was selected from the Geostatistical Wizard in ArcGIS Pro. Parameters and cross validation reports for the Kriging process can be viewed in Appendix D. Only elemental

data was changed between models for the Kriging process. Geoprocessing of the resultant Kriging raster layer, with a predictive output surface in the same coordinate system as the DSM, was clipped and masked to reflect only the surface of the stockpiles.

## **RESULTS**

Results from the investigation regarding residual mineral content of bauxite stockpiles are presented for both the UAV flight and elemental analysis. The stockpile volume and comparison of open source and commercial applications were addressed first, followed by elemental analysis. The elemental analysis included identifying the presence of elements by XRF and LA-ICP-MS, comparison of XRF and LA-ICP-MS data, evaluation of elemental enrichment compared to background values of the upper continental crust and NIST-698 sample, and a surficial spatial distribution of elements in each stockpile.

### **Stockpile Volume**

The volumes computed for each stockpile using QGIS and ArcGIS Pro can be found in Table 3. An independent sample t-test assuming unequal variance was run in Microsoft Excel for each stockpile to determine if there were differences in volume computations between QGIS and ArcGIS Pro (Table 4, Appendix E). The largest percent difference (Equation 4) comparing averaged stockpile volume results from QGIS and ArcGIS Pro was 4.2% (Table 5).

Table 3. Volume measurements from QGIS and ArcGIS Pro with averaged results for each stockpile at the bottom of each section (*shaded in tan*).

QGIS - Volume (m <sup>3</sup> )					
Results	SP1	Clay	SP2	SP3	SP4
1	17935.9	1886.28	42370.7	15363.5	7391.0
2	17884.3	1912.81	40727.2	15328.4	7505.4
3	17856.9	1916.32	40799.4	15294.9	7406.9
4	17952.9	1933.71	41035.8	15151.6	7426.8
5	17842.9	1934.82	40472.9	15266.1	7470.0
6	17956.4	1822.98	40937.9	15056.4	7489.8
7	17953.7	1865.05	40969.9	15289.1	7489.7
8	17592.6	1954.09	41132.0	15244.8	7478.9
9	17975.4	1842.62	40978.2	15210.9	7478.0
10	17832.3	1879.88	40378.1	15090.5	7440.1
Average	17878.3	1894.86	40980.2	15229.6	7457.7

ArcGIS Pro - volume (m <sup>3</sup> )					
Results	SP1	Clay	SP2	SP3	SP4
1	18582.8	1927.38	42340.2	15428.8	7547.1
2	18591.1	1945.8	42181.9	15660.2	7531.1
3	18738.1	1934.88	42382.8	15561.3	7533.5
4	18644.4	1964.68	42192.0	15685.3	7521.8
5	18634.4	1942.19	42295.8	15667.1	7617.8
6	18694.4	1971.47	42217.3	15584.4	7589.3
7	18657.1	1935.23	42054.6	16039.4	7618.8
8	18685.4	1927.8	42275.2	15710.2	7655.8
9	18528.6	1936.63	42258.2	15603.3	7519.0
10	18666.9	1991.98	42023.1	15113.1	7554.9
Average	18642.3	1947.8	42222.1	15605.3	7568.9

Table 4. Results from independent sample t-tests assuming unequal variance with confidence intervals (C.I.) showing statistically significant differences and p-values for volumes calculated for each stockpile from QGIS and ArcGIS Pro. A p-value less than 0.05 indicates a significant statistical difference in values. Full t-test results can be found in Appendix E.

Independent t-test results comparing QGIS and ArcGIS volumes				
Stockpile	Statistically Significant Differences	P(T<=t) two-tail values	95% C.I. Lower	95% C.I. Upper
SP1	763.99	2.56E-11	678.42	849.57
Clay	52.95	0.003902584	21.18	84.72
SP2	1241.92	0.000035238	871.50	1612.30
SP3	375.67	0.000537622	206.82	544.53
SP4	111.25	2.73E-05	70.08	152.41

\*C.I. – confidence interval

Table 5: Results averaged from ten volume measurements per stockpile using QGIS and ArcGIS Pro. The percent difference results between the two software analyses were calculated using Equation 4. A list of all volume measurements can be found in Table 3.

Volume results for stockpiles comparing QGIS and ArcGIS Pro					
	SP1 (m <sup>3</sup> )	Clay (m <sup>3</sup> )	SP2 (m <sup>3</sup> )	SP3 (m <sup>3</sup> )	SP4 (m <sup>3</sup> )
Open-source (QGIS)	17878.3	1894.9	40980.2	15229.6	7457.7
Commercial (ArcGIS Pro)	18642.3	1947.8	42222.1	15605.3	7569.0
Percent Difference (%)	4.2	2.8	3.0	2.4	1.5

## XRF Analyses: Elements Detected

XRF revealed the presence of important elements within each stockpile. For many of the elements, results varied between stockpiles and samples within each stockpile. This was not unexpected considering the heterogeneity of bauxite, which reinforced the rationale of each sample being examined three times during the XRF analysis (Appendix F). Elements identified during XRF analysis are shown in Table 6.

## LA-ICP-MS Analyses

Elements listed on the 2022 List of Critical Minerals (Burton, 2022), for LA-ICP-MS analysis can be found in Table 7. For a complete list of results see Appendix G.

Table 6: Elements identified during XRF analysis of samples from Section 20 stockpiles: elements present in at least one category (matrix, SP1, clasts, etc.) for over 80% of samples (left), 40-80% of samples (middle), less than 40% of samples (right).

Elements Detected: XRF Analyses					
Above 80% of samples		40-80% of samples		Less than 40% of samples	
Element	Symbol	Element	Symbol	Element	Symbol
Magnesium*	Mg	Phosphorus	(P)	Chlorine	(Cl)
Aluminum*	(Al)	Potassium	(K)	Vanadium*	(V)
Silicon	(Si)	Manganese*	(Mn)	Chromium*	(Cr)
Sulfur	(S)	Copper	(Cu)	Cobalt*	(Co)
Calcium	(Ca)	Tin*	(Sn)	Nickel*	(Ni)
Titanium*	(Ti)			Selenium	(Se)
Iron	(Fe)			Silver	(Ag)
Zinc*	(Zn)			Cadmium	(Cd)
Arsenic*	(As)			Antimony*	(Sb)
Rubidium*	(Rb)			Tungsten*	(W)
Strontium	(Sr)			Gold	(Au)
Yttrium*	(Y)			Bismuth*	(Bi)
Zirconium*	(Zr)				
Niobium*	(Nb)				
Molybdenum	(Mo)				
Barium*	(Ba)				
Lanthanum*	(La)				
Cerium*	(Ce)				
Praseodymium*	(Pr)				
Neodymium*	(Nd)				
Lead	(Pb)				
Thorium	(Th)				
Uranium	(U)				

\*Critical element

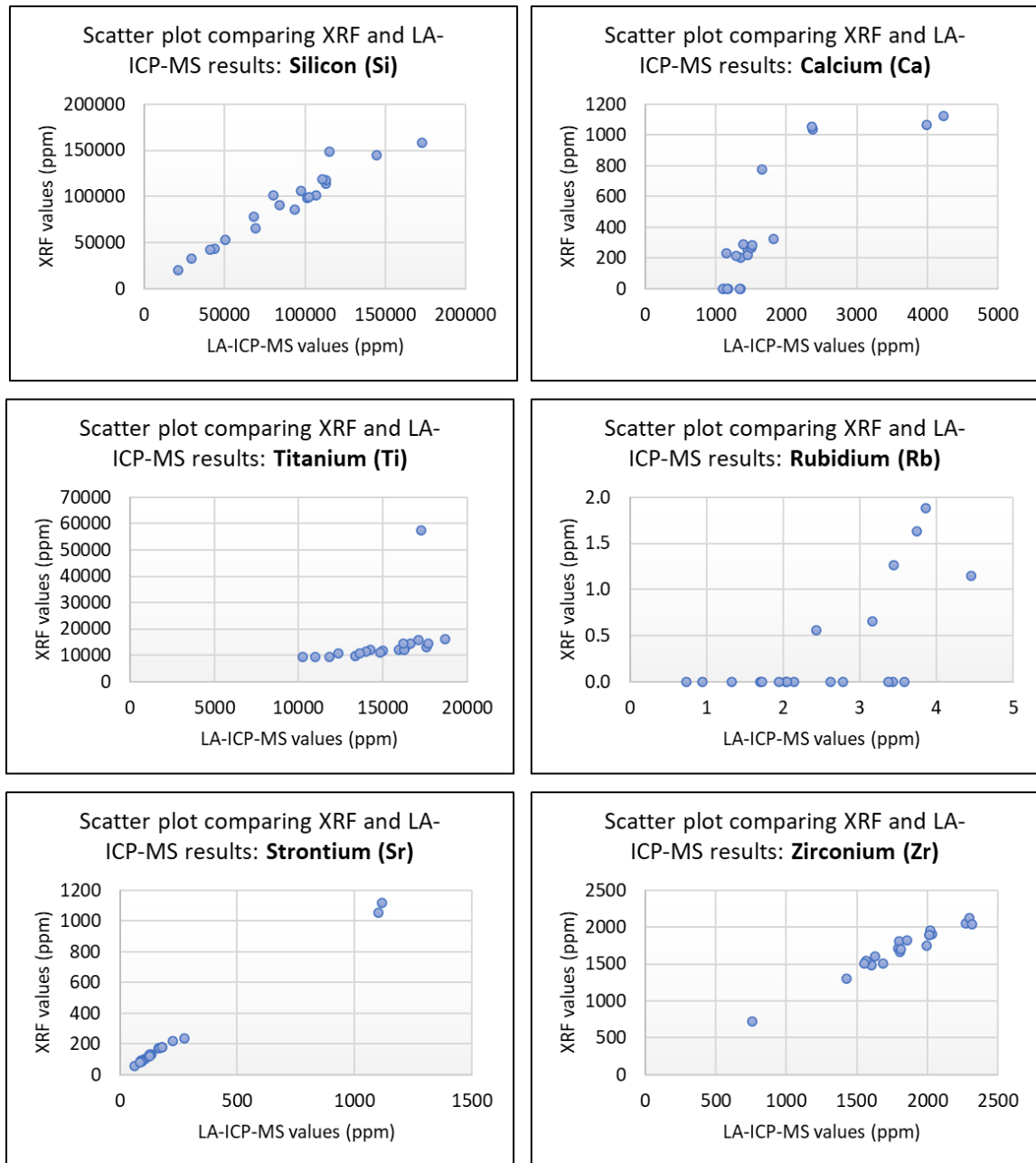
Table 7. LA-ICP-MS results in ppm for elements on the 2022 List of Critical Minerals (Burton, 2022). Values for concentrations of the Earth's upper continental crust are listed at the top of the Table 6 for reference (Rudnick & Gao, 2014). For a complete list of all elements found and associated data, see Appendix G.

Sample	LA-ICP-MS values for critical elements								
	Ti ppm	Ga ppm	Rb ppm	Zr ppm	Nb ppm	Ce ppm	Hf ppm	Ta ppm	Ba ppm
Upper Crust	3837	18	84	193	12	63	5	1	624
NIST-698	13633	41	0	461	50	256	12	3	55
SP1026	14246	59	2	1685	621	613	36	50	100
SP1018	17612	56	2	2015	752	252	43	64	69
SP1015	13977	54	3	1796	654	339	38	54	60
SP1006	15957	62	2	2036	763	527	43	60	51
Clay015	17290	39	3	2276	724	208	45	62	86
Clay006	16342	46	2	1998	678	226	42	57	68
SP2026	12371	49	4	1604	597	267	34	46	59
SP2022	11012	55	3	1425	513	572	31	41	53
SP2020	14993	58	4	1629	662	572	35	52	60
SP2017	18683	60	2	2296	926	221	47	67	53
SP2007	13351	48	3	1567	579	339	34	48	53
SP2005	10254	53	1	759	316	923	15	22	74
SP3026	14842	58	3	1808	697	506	38	56	52
SP3023	13604	53	3	1800	672	460	38	55	48
SP3008	11852	49	4	1553	583	455	34	49	46
SP3011	16245	57	4	1810	691	494	38	55	52
SP4018	16662	87	1	1859	707	787	40	56	199
SP4014	17133	61	2	2022	767	468	43	61	160
SP4012	16195	55	2	2017	756	257	44	61	50
SP4006	17707	82	1	2314	808	565	50	66	142

## Comparison of XRF and LA-ICP-MS Data

Elements present in both XRF and LA-ICP-MS analyses were compared to examine the reliability of quantitative data when using XRF. Figure 24 shows scatterplots with a visual linear relationship between XRF and LA-ICP-MS results. For each element that had a linear relationship present, a Pearson's correlation coefficient value was calculated (Table 8). A line of best fit equation was derived for correlation coefficient values that were very strong or perfect. These were later used to calibrate XRF results for the respective element. Figure 25 shows scatter plots of elements that were visually determined not to have a linear relationship, and therefore did not meet criteria to use a Pearson's coefficient correlation value. Tabular data for this comparison of XRF and LA-ICP-MS data can be found in Appendix H.

Figure 24. Scatter plots of XRF and LA-ICP-MS elemental results showing linear relationship.



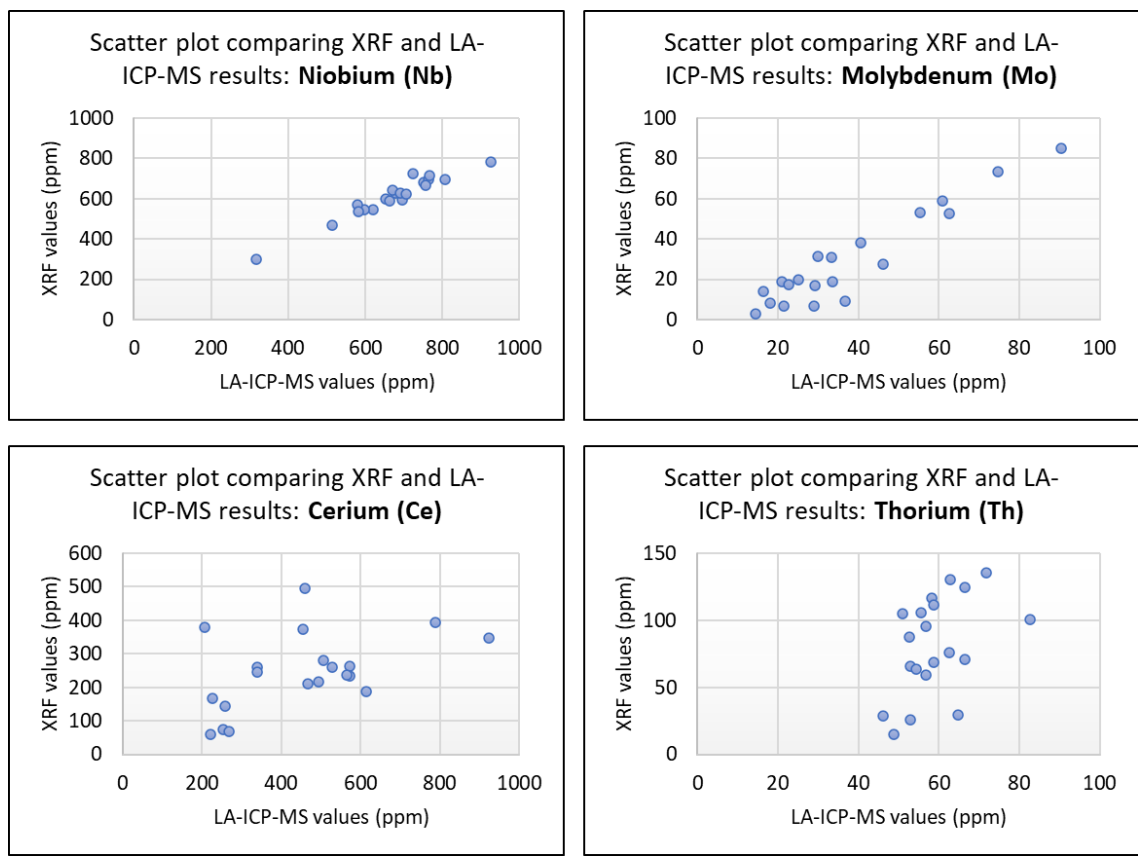
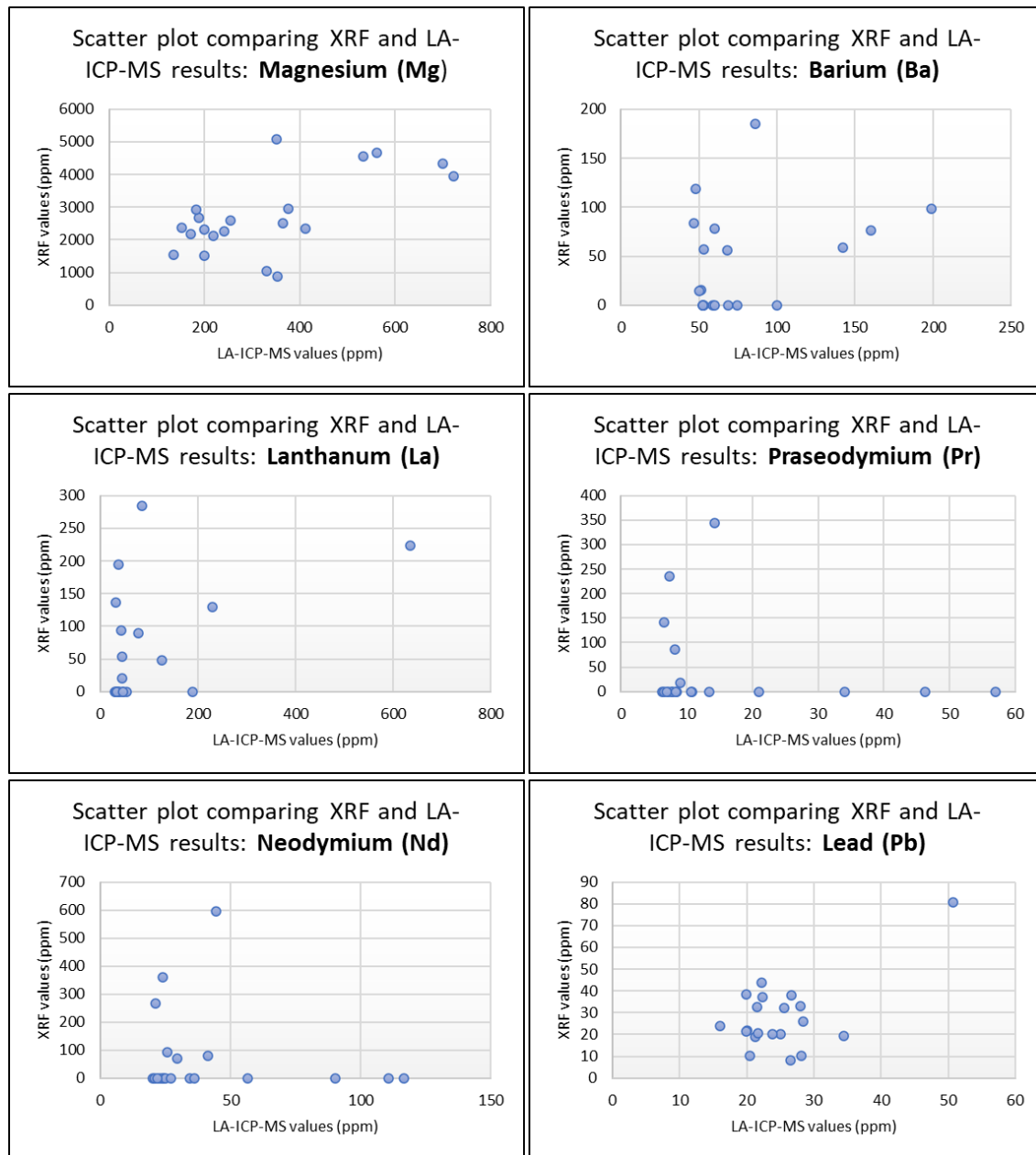


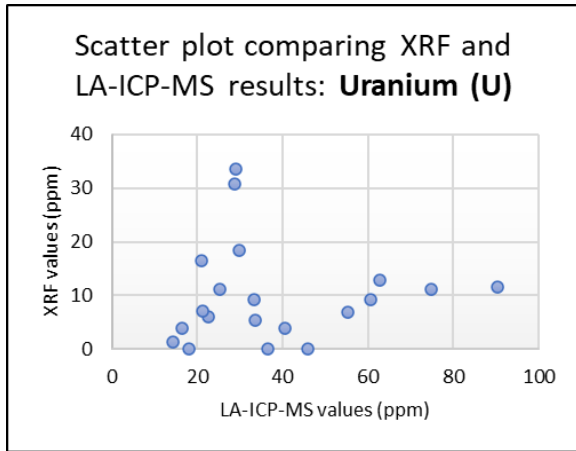
Table 8: Pearson's correlation coefficient values comparing elemental results from XRF and LA-ICP-MS analyses. Line of best fit equations were only shown for results with very strong or perfect correlation coefficients, and were used for calibrating XRF results. Tabular data of elemental results comparing the two analytical methods can be found in Appendix H and scatter plots in Figures 24 (linear) and 25 (non-linear).

Results comparing XRF and LA-ICP-MS values		
Element	Pearson's correlation coefficient value	Line of best fit equation
Mg*	No linear trend	-
Si	0.964	$y = 0.9857x + 4977.7$
Ca	0.855	$y = 0.3913x - 312.42$
Ti*	0.398	-
V*	Null	-
Cr*	Null	-
Ni*	Null	-
Rb*	0.648	$y = 0.3891x - 0.6443$
Sr	0.999	$y = 0.9833x - 1.9382$
Zr*	0.979	$y = 0.8717x + 120.1$
Nb*	0.968	$y = 0.8178x + 60.781$
Mo*	0.944	$y = 1.0684x - 11.1$
Ba*	No linear trend	-
La*	No linear trend	-
Ce*	0.486	-
Pr*	No linear trend	-
Nd*	No linear trend	-
Pb	No linear trend	-
Th	0.476	-
U	No linear trend	-

\*Critical element

Figure 25. Scatter plots of XRF and LA-ICP-MS elemental results showing non-linear relationship.





### XRF Sample Enrichment: Earth's Upper Continental Crust

Of the 128 samples analyzed using XRF, nineteen elements were determined to be enriched when compared to background concentrations of the Earth's upper continental crust (Equation 6). Table 9 lists elements if more than 40% of samples from at least one group (individual stockpiles, clasts, or matrix) were enriched and shows the percentage of enriched samples from XRF values compared to background elemental concentrations of the Earth's upper continental crust.

Table 9: Table showing percentage of enriched samples (>40%) from XRF elemental values per group compared to background elemental concentrations of the Earth's upper continental crust (Rudnick & Gao, 2014).

XRF: percentage (%) of samples enriched compared to Earth's upper continental crust							
Element	Clasts	Matrix	SP1	Clay	SP2	SP3	SP4
Mg*	100	0	0	0	0	0	0
Al*	100	100	100	100	100	100	100
P	38	0	7	63	14	11	26
S	63	50	57	38	28	25	47
Ti*	50	100	100	100	100	100	100
Mn*	50	17	0	0	7	0	5
Fe	75	67	43	44	31	47	42
Cu	13	50	18	0	14	14	11
As*	100	100	96	94	100	100	100
Sr <sup>1</sup>	25	33	14	0	0	14	47
Zr* <sup>1</sup>	100	100	100	100	100	100	100
Nb* <sup>1</sup>	100	100	100	100	100	100	100
Mo <sup>1</sup>	63	83	82	75	83	83	84
Sn*	38	0	43	19	38	33	42
La*	100	83	50	81	41	47	68
Ce*	100	100	93	94	100	100	100
Pr*	75	67	36	50	24	39	26
Nd*	88	67	32	56	31	42	32
Pb	50	67	100	100	100	100	100
Th	75	100	96	100	100	100	100
U	25	67	100	100	100	100	100

\*Critical element  
<sup>1</sup>Empirical calibration of XRF results using LA-ICP-MS data

## LA-ICP-MS Sample Enrichment: Earth's Upper Continental Crust

The twenty samples sent for LA-ICP-MS analysis at Texas Tech GeoAnalytical Laboratory showed enrichment in twenty-two elements. Of these samples, eighteen were reported as critical elements. Table 10 displays how many times greater the LA-ICP-MS stockpile quantities were compared to the Earth's upper continental crust (Rudnick & Gao, 2014).

Table 10: Values listed represent percent greater than background concentration of elements in Earth's upper continental crust from LA-ICP-MS results (Rudnick & Gao, 2014).

LA-ICP-MS: Percent greater than Earth's upper continental crust												
Sample	Ti*	V*	Ga*	Y*	Zr*	Nb*	Mo	La*	Ce*	Pr*	Gd*	
	%	%	%	%	%	%	%	%	%	%	%	%
SP1026	271	95	236	100	773	7657	75	507	873	380	609	
SP1018	359	96	222	119	944	9299	150	52	300	19	0	
SP1015	264	76	206	105	831	8073	88	39	439	15	76	
SP1006	316	67	252	105	955	9444	78	6	737	12	5	
Clay015	351	81	123	162	1079	8954	50	174	230	101	16	
Clay006	326	83	163	124	935	8371	180	151	259	89	13	
SP2026	222	56	178	119	731	7361	652	73	324	53	58	
SP2022	187	49	215	48	638	6315	238	17	808	1	45	
SP2020	291	63	231	76	744	8180	406	26	808	10	35	
SP2017	387	104	242	305	1090	11475	523	11	251	9	9	
SP2007	248	46	172	76	712	7140	20	41	438	28	16	
SP2005	167	5	205	29	293	3855	422	1952	1365	703	66	
SP3026	287	87	229	81	837	8615	178	1	704	7	31	
SP3023	255	128	204	81	833	8298	284	20	631	4	153	
SP3008	209	67	181	62	705	7193	205	2	622	7	17	
SP3011	323	61	227	81	838	8536	362	8	683	1	23	
SP4018	334	104	398	114	863	8735	142	639	1149	551	7	
SP4014	347	112	247	133	948	9482	110	50	643	50	16	
SP4012	322	127	213	124	945	9356	36	40	308	18	135	
SP4006	361	122	370	157	1099	10002	141	307	797	195	60	
Average	291	81	226	107	840	8317	217	205	618	110	25	
Upper Crust (ppm)	3837	97	18	21	193	8	12	31	63	7.1	4	
*Critical element Red values are negative												

LA-ICP-MS: Percent greater than Earth's upper continental crust												
Sample	Dy*	Ho*	Er*	Tm*	Yb*	Lu*	Hf*	Ta*	Pb	Th	U	
	%	%	%	%	%	%	%	%	%	%	%	%
SP1026	69	86	147	225	239	235	579	5451	17	429	326	
SP1018	54	82	151	259	266	276	706	7002	31	454	352	
SP1015	54	76	139	221	235	231	618	5955	47	441	211	
SP1006	52	81	146	243	268	260	710	6564	18	495	274	
Clay015	94	122	191	318	344	349	753	6741	103	365	171	
Clay006	76	92	159	252	290	294	687	6282	67	459	226	
SP2026	78	94	149	228	224	216	540	5056	27	386	243	
SP2022	13	26	67	123	142	129	490	4408	20	339	184	
SP2020	34	53	102	192	201	191	566	5661	57	403	257	
SP2017	227	282	388	534	511	498	790	7309	17	499	483	
SP2007	38	50	100	173	188	192	544	5214	25	417	141	
SP2005	5	23	12	5	5	11	191	2323	198	402	215	
SP3026	36	53	109	191	213	213	620	6157	50	459	238	
SP3023	36	58	117	194	220	212	610	5984	66	516	228	
SP3008	28	48	98	166	182	184	547	5390	56	404	194	
SP3011	31	52	109	189	211	209	614	6025	32	440	222	
SP4018	79	95	145	227	240	228	651	6112	6	533	498	
SP4014	84	100	162	266	284	275	703	6637	64	584	312	
SP4012	77	101	161	255	264	254	732	6723	40	532	266	
SP4006	107	131	195	300	318	303	835	7187	28	686	641	
Average	63	83	141	228	242	237	624	5909	48	462	284	
Upper Crust (ppm)	3.9	0.8	2.3	0.3	2	0.3	5.3	0.9	17	11	2.7	
<i>*Critical element</i> <i>Red values are negative</i>												

### Sample Enrichment Compared to NIST-698 (Jamaican Bauxite Standard) Sample

Arkansas bauxite sample values collected in Section 20 were compared to NIST-698, a Jamaican bauxite standard sample that was available for this study. Jamaican bauxite is a gibbsite-rich bauxite hosted in karstic material with a parent material derived from Miocene volcanic ash (Comer, 1974; Valeton, 1972). Enrichment for this study means that the values were higher than the NIST-698 sample.

### XRF Sample Enrichment: NIST-698

Of the 128 samples analyzed using XRF, sixteen elements were determined to be enriched when compared to the Jamaican bauxite standard NIST-698 sample. Table 11 lists elements if more than 40% of samples from at least one group were enriched. Table 11 also shows the percentage of enriched samples from XRF values compared to NIST-698 sample per group and associated element.

Table 11: Table showing percentage of enriched samples from XRF values per group and respective elements compared to NIST-698 sample (Equation 6). Elements were listed if more than 40% of samples from at least one group were enriched.

XRF: percentage (%) of samples enriched compared to NIST-698							
Element	Clasts	Matrix	SP1	Clay	SP2	SP3	SP4
Mg*	100	100	100	100	100	100	100
Si <sup>1</sup>	100	100	100	100	100	100	100
S	88	17	68	44	28	28	47
K	13	67	7	75	76	56	11
Fe	88	0	0	0	7	0	0
Ti*	13	67	21	25	10	19	63
As*	38	50	50	6	14	25	26
Sr <sup>1</sup>	38	83	57	19	34	36	74
Zr* <sup>1</sup>	88	100	100	100	100	100	100
Nb* <sup>1</sup>	100	100	100	100	100	100	100
Mo <sup>1</sup>	25	83	57	50	79	67	58
Ba*	100	83	32	31	21	33	53
La*	88	0	0	13	10	8	0
Ce*	100	33	32	19	41	47	21
Pr*	100	33	32	38	21	28	26
Nd*	100	33	25	25	21	31	21
Pb	0	67	7	13	10	8	5
Th	38	100	100	100	100	100	100
U	13	83	61	31	55	53	68

\*Critical element

<sup>1</sup>Empirical calibration of XRF results using LA-ICP-MS data

## LA-ICP-MS Sample Enrichment: NIST-698

The twenty samples sent for LA-ICP-MS analysis at Texas Tech GeoAnalytical Laboratory showed enrichment (Table 12); of these, nine were reported as critical elements. Table 13 displays how many times greater the LA-ICP-MS stockpile quantities were compared to the NIST-698 sample.

Table 12: List of enriched elements from LA-ICP-MS analyses compared to NIST-698 sample. Elements were listed if more than 40% of samples from at least one group were enriched.

LA-ICP-MS results: elements enriched compared to <b>NIST-698</b>	
Element	Symbol
Sodium	(Na)
Magnesium*	(Mg)
Silicon	(Si)
Titanium*	(Ti)
Gallium*	(Ga)
Rubidium*	(Rb)
Strontium	(Sr)
Zirconium*	(Zr)
Niobium*	(Nb)
Molybdenum	(Mo)
Barium*	(Ba)
Cerium*	(Ce)
Hafnium*	(Hf)
Tantalum*	(Ta)
Thorium	(Th)
Uranium	(U)
<i>*Critical element</i>	

Table 13: List of critical elements comparing LA-ICP-MS values to NIST-698 sample (Equation 5). A complete list of elements can be viewed in Appendix I.

LA-ICP-MS: percent greater than NIST-698									
Sample	Ti %	Ga %	Rb %	Zr %	Nb %	Ce %	Hf %	Ta %	Ba %
SP1026	0	45	302	273	1143	104	140	1353	40
SP1018	23	38	383	346	1407	-16	185	1759	-4
SP1015	-2	32	519	298	1210	13	154	1485	-16
SP1006	12	52	407	351	1430	76	186	1644	-28
Clay015	21	4	713	404	1351	-31	201	1690	20
Clay006	15	13	477	342	1258	-25	178	1570	-5
SP2026	-13	20	816	255	1096	-11	126	1249	-18
SP2022	-23	36	700	216	928	91	108	1080	-26
SP2020	5	42	954	261	1227	91	135	1408	-17
SP2017	31	47	309	408	1755	-26	214	1839	-26
SP2007	-6	17	650	247	1060	13	127	1291	-26
SP2005	-28	31	216	68	534	208	3	534	4
SP3026	4	42	716	300	1297	69	154	1537	-27
SP3023	-5	31	559	299	1246	53	151	1492	-33
SP3008	-17	21	750	244	1069	52	129	1337	-35
SP3011	14	41	787	301	1284	65	152	1503	-27
SP4018	17	115	75	312	1316	162	165	1526	177
SP4014	20	49	384	348	1436	56	184	1663	123
SP4012	14	35	361	347	1416	-14	194	1686	-30
SP4006	24	102	125	412	1519	88	230	1807	98
Average	5	40	510	302	1,249	51	156	1473	7
NIST-698 (ppm)	14268	41	0.42	452	50	300	15	3.4	71.7
<i>*Negative values in red</i>									

## Fe, Ti, and Al Correlations

Results from XRF elemental analyses were used to obtain Pearson's correlation coefficient values in stockpiles comparing elements tested (ppm) with Fe, Ti, and Al (ppm). Prior to computing the correlation coefficients from Microsoft Excel, a visual examination of scatterplots was conducted to ensure Pearson's correlation coefficient values could be used. For graphs that did not show a linear relationship upon visual inspection, no values were reported. Results from comparing Fe, Ti, and Al with the elements in the stockpiles can be found in Table 14. Similar results comparing the same elements to the matrix and clasts can be found in Table 15.

Scatterplots showing all linear and non-linear relationships of elements tested by XRF can be found in “Additional Files” section attached to this work.

Table 14: Pearson's correlation coefficient values comparing stockpile elements with Fe, Ti, and Al using XRF results. A complete list of elemental results can be found in Appendix J.

Pearson's correlation coefficient values comparing elements in <b>stockpiles</b> to Fe, Ti, and Al using XRF															
Group/ Element	SP1			Clay			SP2			SP3			SP4		
	Fe	Ti	Al	Fe	Ti	Al	Fe	Ti	Al	Fe	Ti	Al	Fe	Ti	Al
Mg*	-	-	0.5	-	-	-	-	-	-	0.6	-	0.6	-	0.4	0.8
Al*	0.8	-	1.0	0.6	0.6	1.0	0.8	-	1.0	-	-	1.0	0.6	-	1.0
Si	-	-	0.5	-	-	-	-	-	-	-	-	-	-	-	-
P	-	-	-	-	-	0.5	-	-	-	-	-	-	-	0.2	-
K	-	0.1	-	-	-	-	-	0.0	0.2	-	-	0.7	-	-	-
Ca	-	-	-	-	-	-	-	-	-	-	-	-	-	-	-
Ti*	0.4	1.0	-	0.9	1.0	0.6	-	1.0	-	0.4	1.0	-	0.6	1.0	-
Fe	1.0	0.4	0.8	1.0	0.9	0.6	1.0	-	0.8	1.0	0.4	0.8	1.0	0.6	0.6
Cu	-	-	-	-	-	-	-	-	-	-	-	-	-	-	0.6
Zn*	-	-	-	-	-	-	-	-	-	-	-	0.4	-	-	-
As*	-	-	-	-	-	-	-	-	-	-	-	-	-	-	-
Sr	-	-	-	-	-	-	-	-	-	-	-	-	-	-	-
Y*	0.5	0.6	0.3	-	-	-	-	0.8	-	0.7	0.8	0.4	0.8	0.9	-
Zr*	-	0.6	-	-	-	0.5	-	0.9	-	0.4	0.9	-	0.5	0.8	-
Nb*	-	0.6	-	-	-	0.6	-	0.9	-	0.5	0.9	0.3	0.3	0.8	-
Mo	-	-	-	-	-	-	-	-	0.1	-	-	-	-	-	-
Ba*	-	-	-	0.9	0.8	0.3	0.9	0.2	0.8	0.8	-	0.5	-	-	-
La*	0.8	-	0.7	0.9	-	-	0.8	0.3	-	0.9	-	0.6	-	-	-
Ce*	-	0.2	-	0.8	0.8	-	-	0.1	0.6	-	0.4	0.7	-	-	-
Pr*	0.9	-	-	0.9	0.9	0.5	0.9	0.3	0.8	0.9	0.3	0.6	0.9	0.6	-
Nd*	0.9	0.3	0.6	0.9	0.9	0.5	1.0	-	0.8	0.9	0.3	0.6	0.9	-	-
Pb	-	-	-	0.5	-	-	-	0.4	-	0.6	-	0.5	0.6	-	-
Th	-	0.4	0.5	0.8	-	0.4	-	0.5	0.4	0.7	0.2	0.6	-	-	-
U	0.6	0.5	-	-	-	-	-	0.8	-	-	-	-	-	-	-
<i>*Critical element</i>															

Table 15: Pearson's correlation coefficient (*r*) values comparing matrix and clasts elements with Fe, Ti, and Al using XRF results. A complete list of elemental results can be found in Appendix J.

Pearson's correlation coefficient values comparing elements in <b>clasts and matrix</b> to Fe, Ti, and Al using XRF						
Group/ Element	Clasts			Matrix		
	Fe	Ti	Al	Fe	Ti	Al
Mg*	-	-	-	-	-	-
Al*	-	-	1.00	0.12	-	1.00
Si	-	-	-	-	-	-
P	-	-	-	-	-	-
K	-	-	-	-	0.74	-
Ca	-	-	-	-	-	-
Ti*	0.78	1.00	-	-	1.00	0.48
Fe	1.00	0.89	-	1.00	-	-
Cu	-	-	-	-	-	0.66
Zn*	-	-	-	-	-	-
As*	-	-	-	-	-	0.81
Sr	0.76	0.76	-	0.68	-	-
Y*	0.67	0.97	-	-	-	-
Zr*	-	-	-	-	0.87	0.76
Nb*	0.68	0.92	-	-	0.89	0.78
Mo	-	-	-	0.05	-	0.70
Ba*	0.70	-	-	-	-	-
La*	0.74	-	-	-	-	-
Ce*	-	0.23	0.06	0.29	-	-
Pr*	0.91	0.70	-	-	-	-
Nd*	0.93	0.71	-	-	-	-
Pb	-	-	-	-	-	-
Th	-	0.74	-	0.80	0.93	-
U	-	-	-	-	-	-

\*Critical element

Results from LA-ICP-MS samples with strong, very strong, or perfect correlation coefficient values comparing Ti to elements across all stockpiles were recorded (Table 16). A full list of correlation coefficient (*r*) values for elements tested can be found in Appendix K.

**Table 16:** Summary of Pearson's correlation coefficient values from samples analyzed by LA-ICP-MS that had strong, very strong, or perfect correlations (Table 1). All elements listed are considered critical, the full list can be found in Appendix K.

Pearson correlation coefficient values comparing Ti to elements using LA-ICP-MS results			
Element	Ti	Element	Ti
Sc	0.733	Ho	0.723
Ti	1.000	Er	0.746
V	0.674	Tm	0.798
Y	0.775	Yb	0.827
Zr	0.898	Lu	0.830
Nb	0.907	Hf	0.878
Tb	0.639	Ta	0.895
Dy	0.694		

### Spatial Distribution of Elements

The maps generated in ArcGIS Pro were used to visualize surficial mobility of elements among the stockpiles in Section 20. Only XRF data was used to display mobility trends for the spatial analyses because the small sample (*n*=20) size for LA-ICP-MS made it difficult to view trends. Sr, Zr, Nb, Si, Ca, and Mo were chosen (Figures 26-31) because

they had very strong or perfect correlations when compared with LA-ICP-MS values. Though Rb had a strong correlation coefficient value, after calibration of the XRF data, the highest value was 1 ppm compared to background concentrations of the Earth's upper continental crust (83 ppm), therefore a map was not rendered for Rb. Of the remaining elements (Sr, Zr, Nb, Si, Ca, and Mo), Zr and Nb are critical elements (Appendix A).

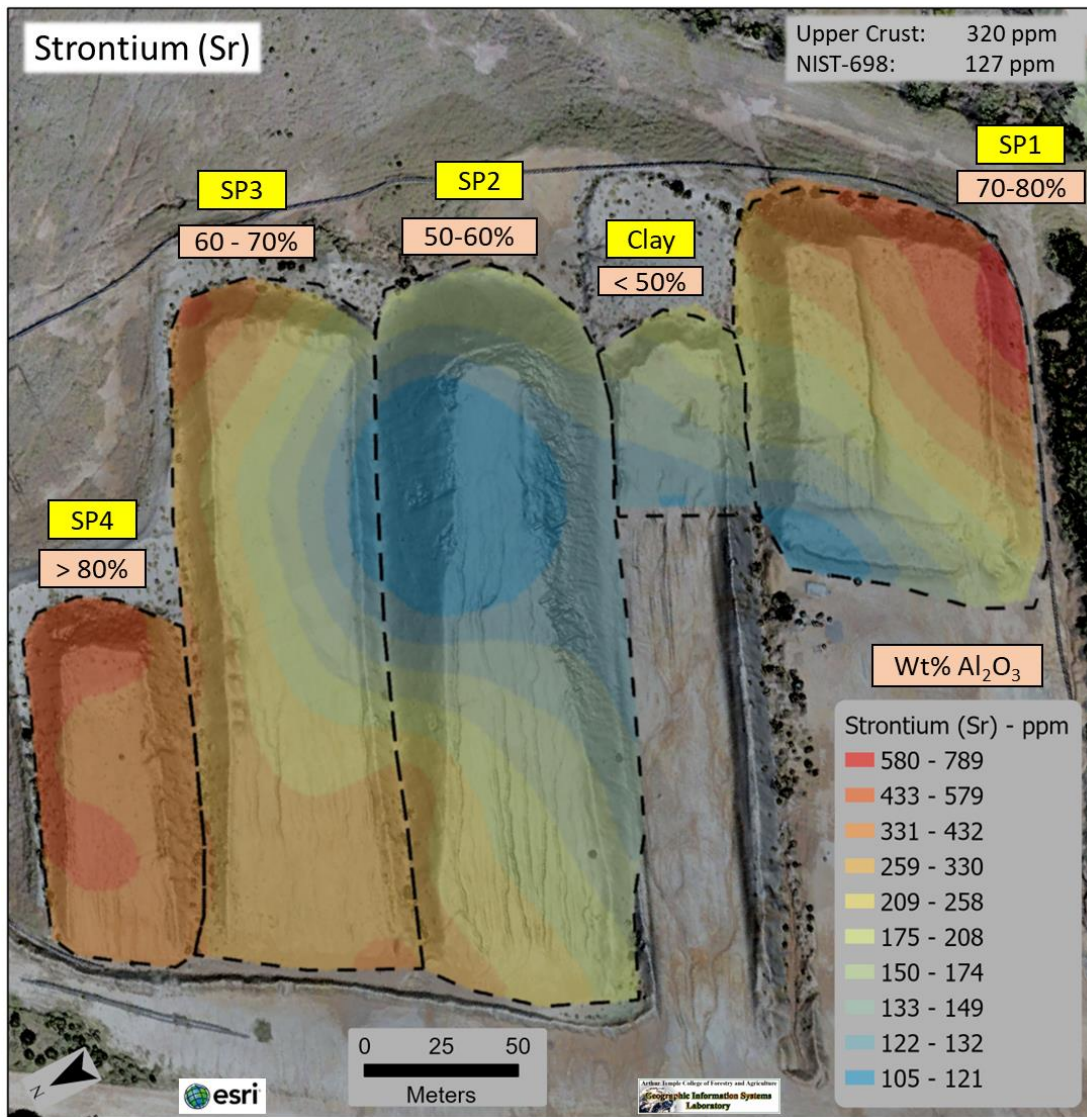


Figure 26: Spatial distribution map of strontium (Sr) in Section 20 of stockpiles with Kriging model applied. Higher values are shaded in red (580 - 789 ppm) as seen at the top of SP1 and lower values in blue (105-121 ppm) as seen in SP2. (Top right) Background concentrations in Earth's upper crust and the NIST-698 LA-ICP-MS values are provided for reference (Rudnick & Gao, 2014). Aluminum oxide ( $\text{Al}_2\text{O}_3$ ) weight percent data provided by McGeorge Contracting Company in 2021.

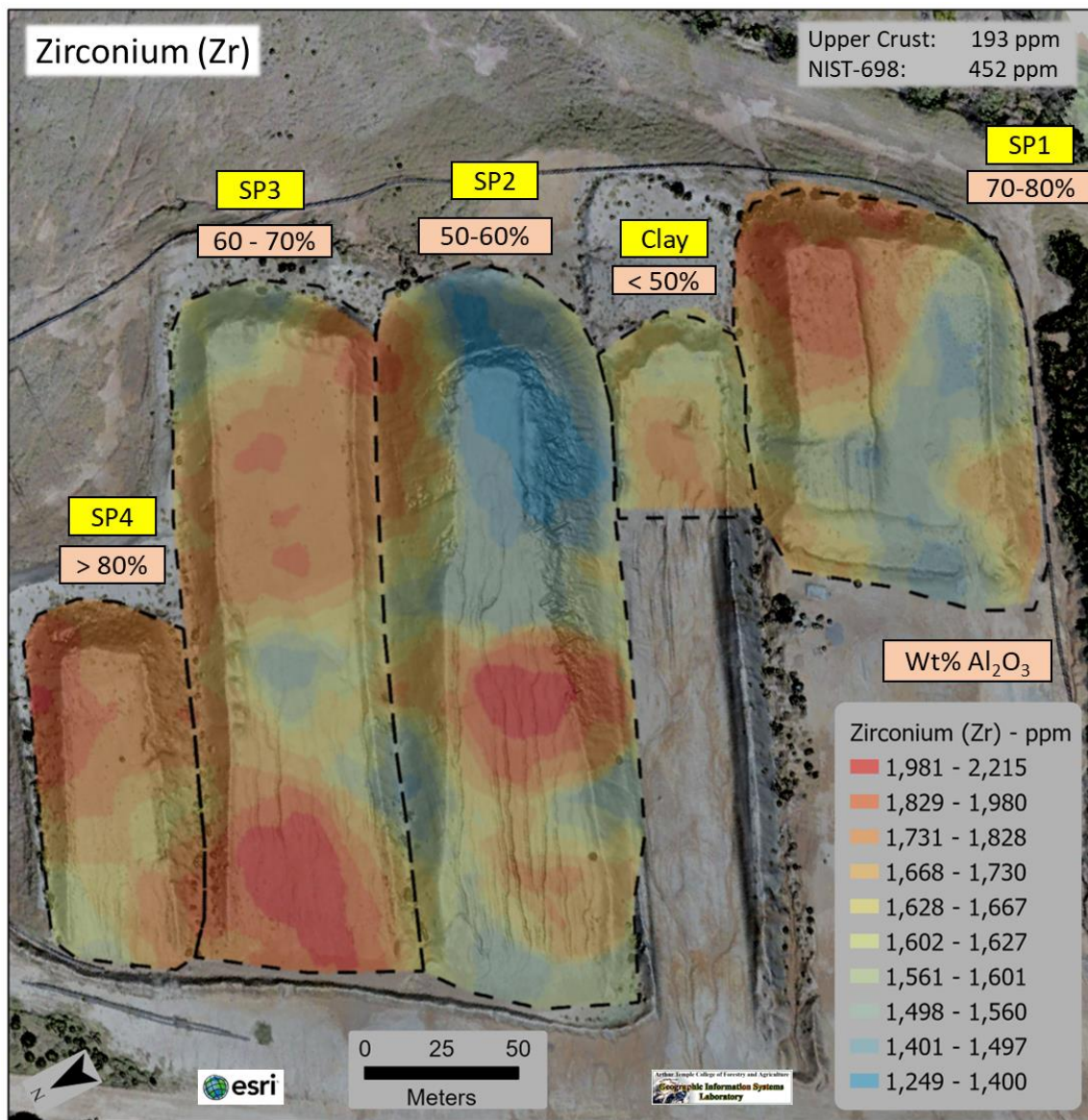


Figure 27: Spatial distribution map of zirconium (Zr) in Section 20 of stockpiles with Kriging model applied. Higher values are shaded in red (1,981 – 2,215 ppm) as seen at the top of SP1 and lower values in blue (1249 - 1400 ppm) as seen in SP2. (*Top right*) Background concentrations in Earth's upper crust and the NIST-698 LA-ICP-MS values are provided for reference (Rudnick & Gao, 2014). Aluminum oxide ( $\text{Al}_2\text{O}_3$ ) weight percent data provided by McGeorge Contracting Company in 2021.

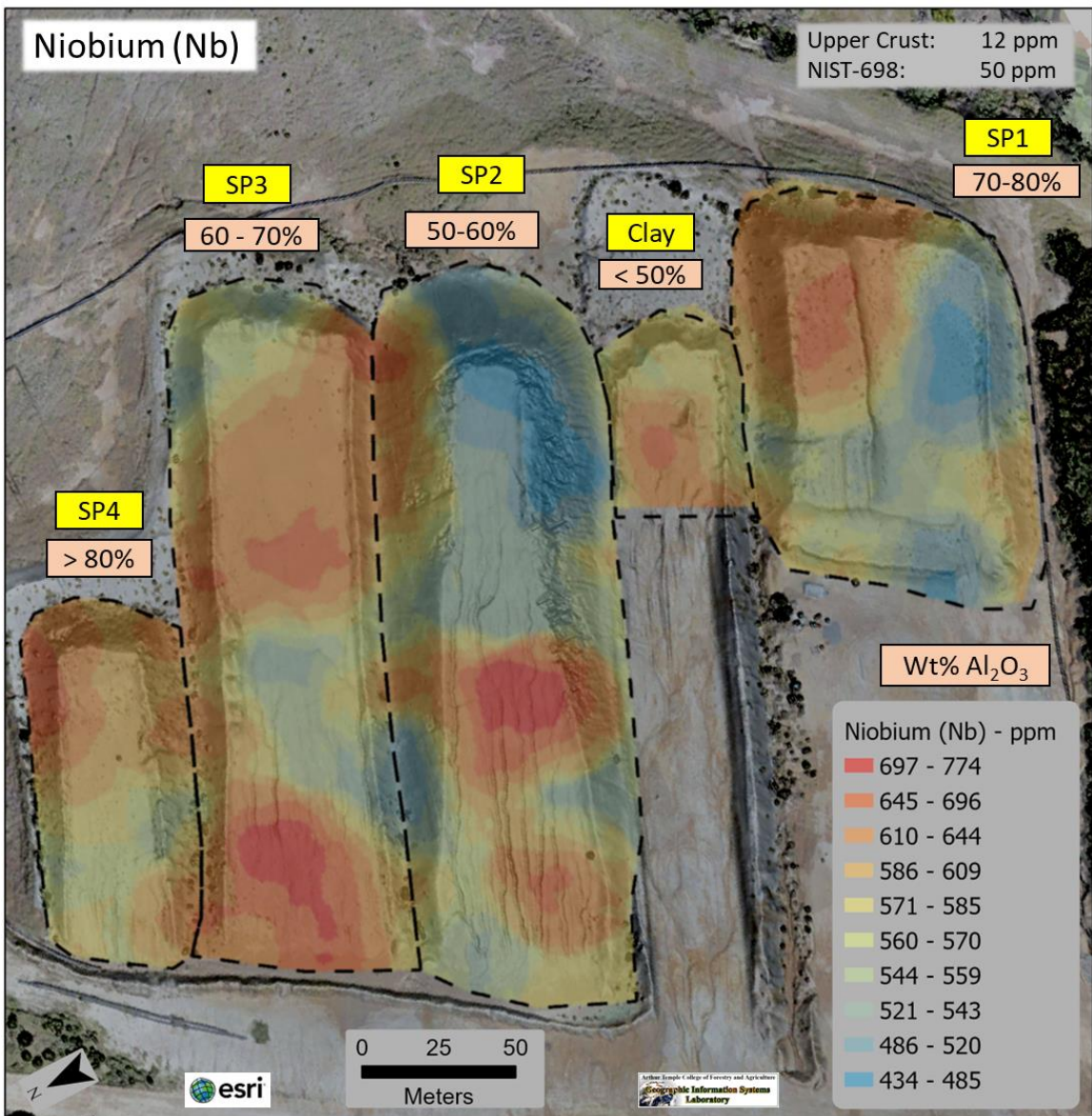


Figure 28: Spatial distribution map of niobium (Nb) in Section 20 of stockpiles with Kriging model applied. Higher values are shaded in red (697 - 774 ppm) as seen at the top of SP1 and lower values in blue (434 - 485 ppm) as seen in SP2. (Top right) Background concentrations in Earth's upper crust and the NIST-698 LA-ICP-MS values are provided for reference (Rudnick & Gao, 2014). Aluminum oxide (Al<sub>2</sub>O<sub>3</sub>) weight percent data provided by McGeorge Contracting Company in 2021.

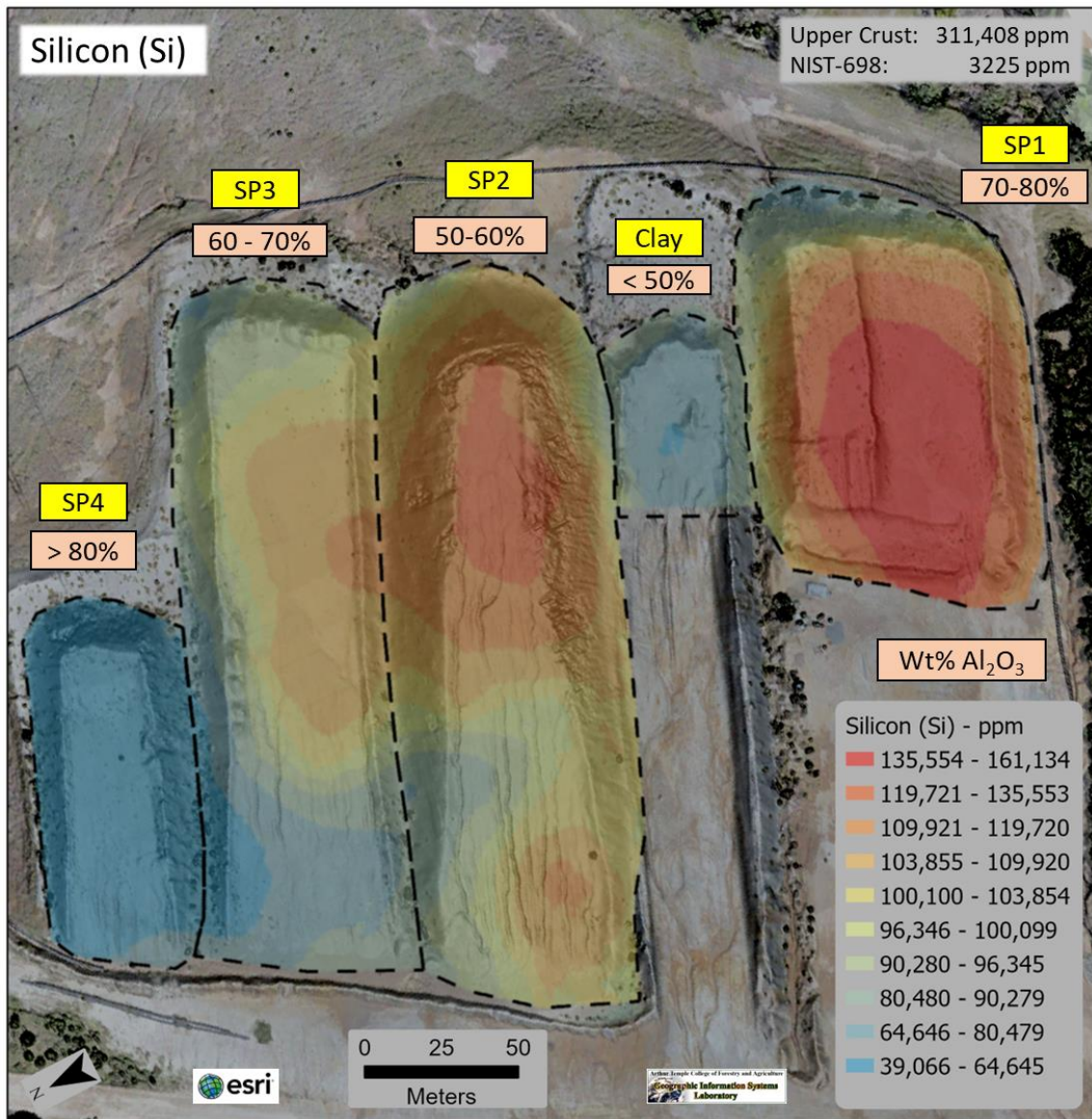


Figure 29: Spatial distribution map of silicon (Si) in Section 20 of stockpiles with Kriging model applied. Higher values are shaded in red (135,554 – 161,134 ppm) as seen at the top of SP1 and lower values in blue (39,066 – 64,645 ppm) as seen in SP2. (Top right) Background concentrations in Earth's upper crust and the NIST-698 LA-ICP-MS values are provided for reference (Rudnick & Gao, 2014). Aluminum oxide ( $\text{Al}_2\text{O}_3$ ) weight percent data provided by McGeorge Contracting Company in 2021.

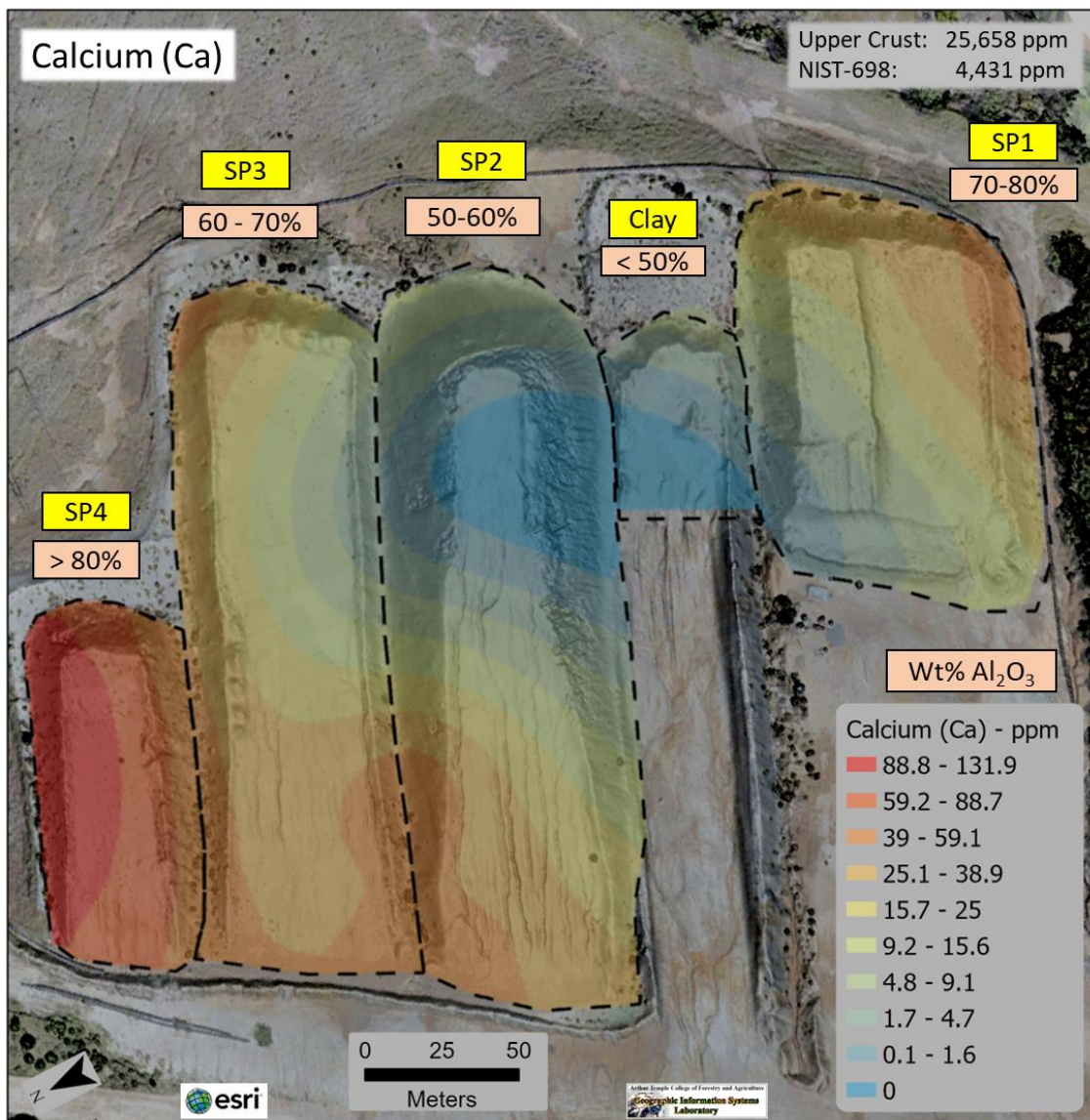


Figure 30: Spatial distribution map of calcium (Ca) in Section 20 of stockpiles with Kriging model applied. Higher values are shaded in red (88.8 – 131.9 ppm) as seen at the top of SP1 and lower values in blue (0 ppm) as seen in SP2. (Top right) Background concentrations in Earth's upper crust and the NIST-698 LA-ICP-MS values are provided for reference (Rudnick & Gao, 2014). Aluminum oxide ( $\text{Al}_2\text{O}_3$ ) weight percent data provided by McGeorge Contracting Company in 2021.

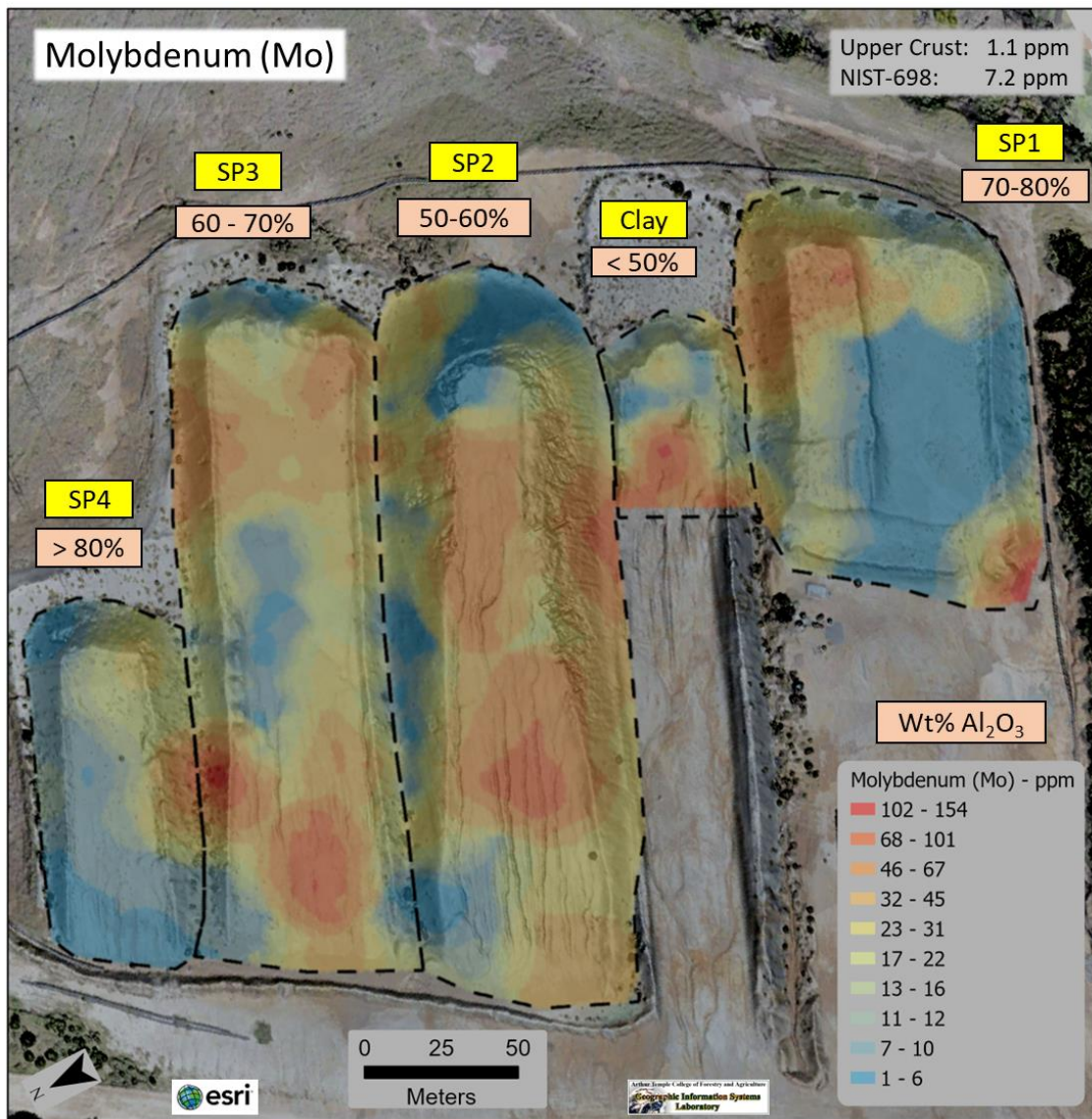


Figure 31: Spatial distribution map of molybdenum (Mo) in Section 20 of stockpiles with Kriging model applied. Higher values are shaded in red (102 - 154 ppm) as seen at the top of SP1 and lower values in blue (1-6 ppm) as seen in SP2. (Top right) Background concentrations in Earth's upper crust and the NIST-698 LA-ICP-MS values are provided for reference (Rudnick & Gao, 2014). Aluminum oxide ( $\text{Al}_2\text{O}_3$ ) weight percent data provided by McGeorge Contracting Company in 2021.

## **DISCUSSION**

### **Volume Analysis**

Volume data for stockpiles are often used to evaluate economic concentrations of minerals at present value. The five stockpiles in Section 20 represent a fraction of the material at the ALCOA reclamation site in Saline County, Arkansas. Mean volumes were consistently higher in ArcGIS Pro for each stockpile (Table 3). A statistically significant difference (p-value less than 0.05) in averaged volume calculations between QGIS and ArcGIS Pro was present for all stockpiles (Table 4). Confidence intervals did provide a range for which approximations can be made 95% of the time (Table 4). The largest percent difference between the averaged stockpile volumes using both QGIS and ArcGIS Pro was 4.2% (Table 5, Equation 4). Though QGIS is open-source, it did require additional steps to compute data and was therefore a more time-consuming process. QGIS did allow user more control over input variables and defining the base layer. ArcGIS Pro was quick and efficient however, it is a commercial software requiring users to pay for access.

### **Elemental Presence**

Elements detected using XRF can be viewed in Table 6. Among the elements detected during XRF analysis, over 80% of samples in at least one group contained Mg,

Al, Ti, Zn, As, Rb, Y, Zr, Nb, La, Ce, Pr, or Nd, which are considered critical elements (Appendix A). Of the elements detected on LA-ICP-MS, Mg, Ti, Sc, Zr, V, Cr, Ni, Ga, Rb, Y, Nb, Ba, La, Ce, Pr, Nd, Eu, Gd, Tb, Dy, Ho, Er, Sm, Tm, Yb, Lu, Hf, Ta were noted to be critical elements (Appendix G). Though critical elements were detected, it is important to note that many may not be significantly enriched in bauxite stockpiles to be considered economic. These elements were also detected in the underlying nepheline syenite in previous a study by Van Gosen and Choate (2021). Because many of these elements are present in the nepheline syenite parent material, it is likely the source for elements found in bauxite as suggested by previous authors (Gordon and Murata, 1952; Mead, 1915; Van Gosen and Choate, 2021). Erosion and weathering of sediments that once covered the bauxite deposit could have also contributed to the enrichment of elements in the area.

#### Comparison of XRF and LA-ICP-MS Results

Understanding the differences between results from XRF and LA-ICP-MS helped interpret elemental mobilization displayed on the surficial elemental spatial distribution maps. Several elements did not show a linear trend and Pearson's correlation coefficient values could not be used. For Si, Ca, Rb, Sr, Zr, Nb, and Mo values, very strong correlations were present and line of best fit equations were used to calibrate XRF data

for the respective element (Appendix K). Correlation values for Ce and Th were moderate, and Ti had a weak correlation between the two instruments.

#### Comparison of Elemental Values: Earth's Upper Continental Crust

The XRF percentage of samples enriched compared to the background element concentration of Earth's upper continental crust using XRF analysis is shown in Table 9. Twelve of the elements listed were reported as critical however, many may not have economic concentrations to be of value.

Clasts and matrix XRF results were compared to determine the source of elements in bauxite. This information could provide insight for extraction techniques if element concentrations are considered economically valuable in the future. Clasts were enriched in Mg, P, Mn, and Sn, while Ti, Cu, and U were concentrated in the matrix. All samples contained Al, As, Zr, Nb, and Ce in both matrix and clasts (Table 9).

Over 94% of stockpile samples were enriched in Al, Ti, Zr, Nb, Pb, Th, and U (Table 9). The Clay stockpile had the highest percentage of enriched elements overall, the clay minerals in that section likely sequestered elements utilizing cation exchange capacity. Future studies with X-ray diffraction would provide valuable information on how these elements are related.

Elemental results showing enriched values compared to Earth's upper continental crust using LA-ICP-MS analysis can be viewed in Table 10. Eighteen of the twenty-two elements listed were reported as critical elements. Because LA-ICP-MS was a quantitative method, Table 10 reflects the percent greater concentration of an element was in bauxite stockpile samples compared to the Earth's upper continental crust.

Nb and Ta values were over 5000% greater than elemental values estimated in Earth's upper continental crust and both are listed as critical elements (Table 1; Table 10). Other critical elements with values ranging from 500 - 1000% higher include Zr, Ce, and Hf (Table 10). Ga, Ti, Mo, La, Tm, Yb, Lu, and U were just over 200% greater than background concentrations of Earth's upper continental crust. Ti, V, Y, Nb, Tm, Yb, Lu, Hf, and U had increased elemental concentration as Al concentration increased; Mo, Ce, and Pb decreased in concentration as Al concentration increased.

#### Comparison of Elemental Values: NIST-698 (Jamaican Bauxite Standard) Sample

XRF analysis showed results from samples that were enriched compared to the NIST-698 sample (Table 11). Ten of the elements listed were reported as critical, however many may not have concentrations to be of economic value in the current market. The clasts had a higher percentage of samples enriched with critical elements (Table 11). A higher percentage of Fe, La, Pr and Nd were concentrated in clasts when

compared to other groups (Table 11). Over 88% of matrix and clast samples were enriched in Mg, Si, Zr, and Nb when compared to NIST-698 sample.

All stockpile samples were enriched with Mo, Nb, Th, Zr, and Si when compared to NIST-698 sample. As Al values increased throughout the stockpiles, the percentage of samples enriched increased for S, Ti, As, Sr, and U (Table 11). The percentage of samples enriched in K and La decreased with increasing Al content throughout the stockpiles. The remaining elements tested with XRF (Table 11) did not have any detectable pattern for sample enrichment.

Elemental results showing enriched values compared to NIST-698 (Jamaican bauxite standard) sample using LA-ICP-MS analysis can be viewed in Table 13. The nine elements listed were reported as critical elements. Because LA-ICP-MS was a quantitative method, Table 13 reflects how much greater the concentration of an element was by percent within the bauxite compared to the NIST-698 sample.

Values for Nb and Ta were over 1000% greater than NIST-698 sample, while Zr and Hf were enriched by over 100% (Table 13). Even though Rb is 500% greater than NIST-698 sample, it is important to note the value of Rb (0.42) ppm is lower than the elemental values reported for Earth's upper continental crust (8 ppm) (Rudnick & Gao, 2014).

## Fe, Ti, and Al Correlations

Pearson's correlation coefficient values derived from XRF data (Tables 14 - 15) showed the relationship of Fe, Ti, and Al with elements tested. Nb and Ti had strong and very strong positive correlations in all the groups except Clay because the Clay value did not meet criteria to use Pearson's correlation coefficient. This supports the theory from Gordon and Murata (1952) that suggested the Nb was likely associated with titanium-rich minerals. LA-ICP-MS results confirmed a very strong positive correlation between Ta-Nb (Figure 32) and Ta-Ti (Table 16). Ta and Nb commonly occur together because of the similarity of elemental properties including valence electrons, atomic size, and ionic size (Schulz et al., 2017). A scatterplot between Ta and Nb showed a positive linear relationship (Figure 32), with a correlation coefficient value of 0.9673.

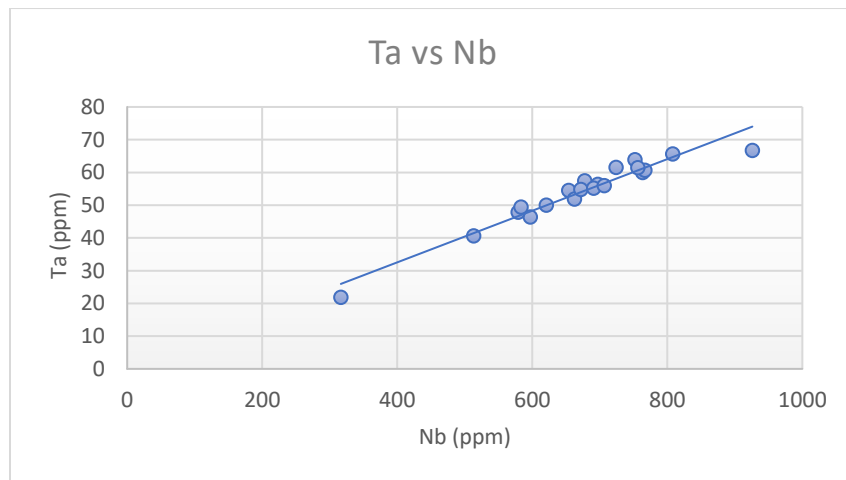


Figure 32: Scatterplot of Nb and Ta from LA-ICP-MS results, showing very strong positive correlation with a calculated correlation coefficient value of 0.9673.

Pr and Nd frequently reported strong and very strong correlations among Fe, Ti, and Al throughout the stockpiles, suggesting that there may be a connection between the two elements. A scatterplot between Pr-Nd revealed a positive linear relationship (Figure 33), with a correlation coefficient value of 0.9812, yielding a very strong correlation. This was not unexpected given their proximity on the periodic table of elements.

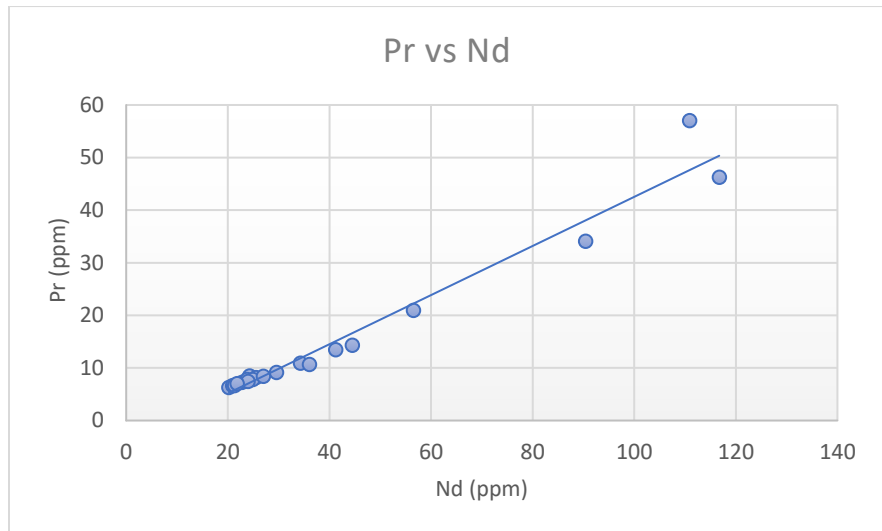


Figure 33: Scatterplot of Pr and Nd from LA-ICP-MS results, showing very strong positive correlation with a calculated correlation coefficient value of 0.9812.

Zr and Hf are another pair of elements that tend to be found in minerals together, both of which had very strong positive correlations with Ti using LA-ICP-MS (Hafnium, 2021). A scatterplot was used to verify a linear relationship, the resulting

correlation coefficient was 0.991, reflecting a very strong positive correlation (Figure 34).

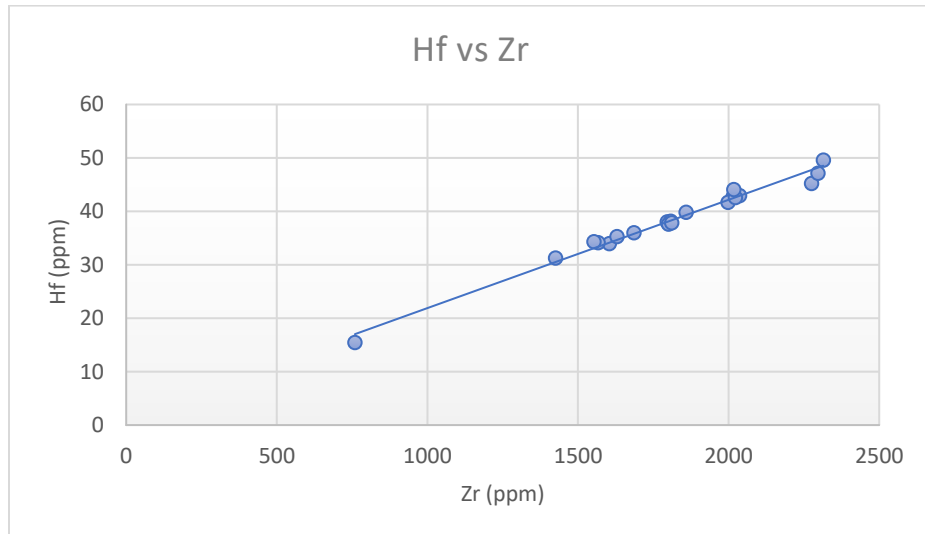


Figure 34: Scatterplot of Hf and Zr from LA-ICP-MS results, showing very strong positive correlation with a calculated correlation coefficient value of 0.991.

#### Spatial Distribution of Elements

This study emphasized elemental mobility in exposed stockpiles for the purpose of potential economic efforts in the future. Mobility of elements in stockpiles could be attributed to several factors including height, slope, differential weathering, heterogeneity of bauxite and time of emplacement of stockpiles at site. It would likely be prudent to examine samples from within the stockpile (i.e. core analysis) for further analysis of elemental movement within stockpiles.

Among the stockpiles analyzed, SP2 had higher element concentrations at the base and down slope (Figures 26-31). The hydrolysates (Zr and Nb) with the exception of Mo, mobilized around the base and down slope of SP2 (Figures 27, 28, 31). It is important to note that SP2 was the tallest, ~14 m (45 ft) above the ground, among all the stockpiles. Higher values of Sr, Zr, Nb, and Ca were noted in stockpiles with higher alumina ( $\text{Al}_2\text{O}_3$ ) content (Figures 26-28, 30). Highest values of Si were concentrated in SP1 and SP2 (Figure 30). No clear pattern or trend was seen among the stockpiles for Mo (Figure 29).

## **LIMITATIONS**

Stockpile volume can vary based on material, void space, and compaction; these characteristics should be considered when evaluating such data. XRF is not typically used for quantitative data analysis but is usually more affordable than LA-ICP-MS. The sample size for LA-ICP-MS was limited to twenty samples among all five stockpiles making interpretation difficult for mineral mobility; therefore, only XRF data was used for elemental mobility analysis. Many calculations for background concentrations of elements in the upper continental crust have been completed over the years and changes as new information is presented, therefore estimates may vary depending on the data source. The lack of ground control points with the drone could impact the volume results because the drone was calculating height from the takeoff point rather than a known elevation.

## **CONCLUSION**

The investigation into the residual minerals in bauxite stockpiles located in Section 20 of the former ALCOA mine in Bauxite, Arkansas revealed the following:

1. Mean volumes were consistently higher in ArcGIS for each stockpile (Table 3).

For all stockpiles, QGIS and ArcGIS had a statistically significant difference in averaged volume calculations (Table 4). The largest percent difference between each software for the averaged stockpile volumes was 4.2% (Table 5). Commercial software (ArcGIS Pro) was faster and more efficient than open source (QGIS) which required more steps to analyze data.
2. Twenty-seven critical elements were detected using both XRF and LA-ICP-MS analyses (Tables 6, 7).
3. Comparing XRF and LA-ICP-MS results, Si, Ca, Rb, Sr, Zr, Nb, and Mo had very strong correlations. The line of best fit from each of these were used to calibrate corresponding XRF values.
4. Analyses comparing XRF elemental values with values reported in Earth's upper continental crust revealed a higher percentage of samples enriched in Mg, P, Mn, and Sn in the clasts; while Ti, Cu, and U were concentrated in the matrix (Table 9). All samples, both matrix and clasts, contained Al, As, Zr, Nb,

and Ce (Table 9). Over 94% of stockpile samples were enriched in Al, Ti, Zr, Nb, Pb, Th, and U, with Clay yielding the highest percentage of enriched elements overall (Table 9).

5. Analyses comparing LA-ICP-MS elemental values against Earth's upper continental crust revealed eighteen critical elements that were enriched (Table 10). Values for Nb and Ta were over 5000% greater; for Zr, Ce, and Hf between 5000-1000% greater; and Ga, Ti, Mo, La, Tm, Yb, Lu, and U around 200% greater than values reported in the Earth's upper continental crust (Table 10).
6. Analyses comparing XRF values with the NIST-698 sample revealed a higher percentage of samples enriched in Fe, La, Pr, and Nd among the clasts (Table 11). Over 88% of samples in both matrix and clasts when compared to NIST-698 sample were enriched in Mg, Si, Zr, and Nb. All stockpile samples were enriched with Mo, Nb, Th, Zr, and Si when compared to NIST-698 sample (Table 11). As Al values increased throughout the stockpiles, the percentage of samples enriched increased for S, Ti, As, Sr, and U (Table 11).
7. Analyses comparing LA-ICP-MS elemental values against NIST-698 sample values revealed nine critical elements that were enriched (Table 13). Values for Nb and Ta were over 1000% greater while Zr and Hf were enriched by over 100% (Table 13). Though Rb was enriched by over 500%, concentrations are much lower than values reported Earth's upper continental crust (8 ppm) (Rudnick & Gao, 2014).

8. Analysis of XRF data reported several elements had varying correlations with Fe, Ti, and Al (Tables 14, 15). Other elements that showed very strong correlations were Ta-Nb, Pr-Nd, Hf-Zr (Figures 32-34).
9. Maps showing spatial distribution of elements (Sr, Zr, Nb, Si, Ca, and Mo), allowed for visual analysis of elemental mobility within stockpiles (Figures 26-31). Higher values of Sr, Zr, Nb, and Ca were noted in stockpiles with higher alumina ( $\text{Al}_2\text{O}_3$ ) content (Figures 26-28, 30). Highest values of Si were concentrated in SP1 and SP2 (Figure 30). The hydrolysates (Zr and Nb) with the exception of Mo, mobilized around the base and slope of SP2, the tallest stockpile among the five in this study (Figures 27, 28, 31). No clear pattern or trend was seen among the stockpiles for Mo (Figure 29).

## FUTURE WORK

Future work concentrated within Section 20 could focus on soil and water analysis near the stockpiles. Core analyses from the top of SP2 could provide better insight to understanding mineral mobility within the stockpiles by evaluating elemental concentrations within the stockpile. Comparing results from this study to other NIST bauxite standards with different parent material could provide more information about the relationship between critical minerals and Arkansas bauxite parent material.

Other avenues that may be worth exploring are the red muds from processed bauxite which have shown potential for critical minerals around the world. Investigating extraction methods for clasts/nodules may prove useful since some elements were concentrated there. Lastly, an economic evaluation of stockpiles with data provided from this study may prove helpful to meet future demand for critical minerals.

## REFERENCES

- ArcGIS Pro(a)- Image Mensuration | Documentation, 2023, Measure feature volume based on an elevation surface raster, <https://pro.arcgis.com/en/pro-app/latest/help/data/imagery/measure-feature-volume-based-on-an-elevation-surface-raster.htm> (accessed December 2023).
- ArcGIS Pro(b) - Raster Interpolation toolset concepts | Documentation, 2023, How Kriging works, <https://pro.arcgis.com/en/pro-app/latest/tool-reference/3d-analyst/how-kriging-works.htm> (accessed April 2024).
- Arkansas Watersheds, 2006, Arkansas Natural Resources Commission, <https://watersheds.cast.uark.edu/> (accessed December, 2022).
- Baksi, A.K., 1997, The timing of Late Cretaceous alkalic igneous activity in the northern Gulf of Mexico basin, Southeastern USA: The Journal of Geology, v. 105, p. 629–644, doi: 10.1086/515966.
- Bauxite, 2022, Encyclopedia Britannica, <https://www.britannica.com/science/bauxite#/media/1/56513/117378> (accessed December 2022).
- Bauxite, 2022, SHE Media Collective, <https://www.earth.com/earthpedia-articles/bauxite/> (accessed December 2022).
- Bramlette, M.N., 1936, Little Rock, AR, Arkansas Geological Survey, p.1-32 (accessed September 2020).
- Branner, J.C., 1897, The bauxite deposits of Arkansas: The Journal of Geology, v. 5, p. 263–289, doi: 10.1086/607775 (accessed August 2022).
- Bureau, U.C., 2021, 2010 decennial census guidance for Data Users: Census.gov, <https://www.census.gov/programs-surveys/decennial-census/guidance/2010.html> (accessed December 2023).

Bugaenko, L.T., Ryabykh, S.M., and Bugaenko, A.L., 2008, A nearly complete system of average crystallographic ionic radii and its use for determining ionization potentials: Moscow University Chemistry Bulletin, v. 63, p. 306–308, doi: 10.3103/s0027131408060011.

Burton, J., 2022, U.S. Geological Survey releases 2022 list of critical minerals: U.S. geological survey: U.S. Geological Survey Releases 2022 List of Critical Minerals | U.S. Geological Survey, <https://www.usgs.gov/news/national-news-release/us-geological-survey-releases-2022-list-critical-minerals> (accessed November 2023).

Bush, W.V., 1996, revised 2007, History of Bauxite in Arkansas, State of Arkansas Geological Commission, p. 1-7.

Comer, J.B., 1974, Genesis of Jamaican bauxite: Economic Geology, v. 69, p. 1251–1264, doi: 10.2113/gsecongeo.69.8.1251 (accessed February 2024).

Conversion factors, 2002, Molecular weights and conversion factors, <https://www.geol.umd.edu/~piccoli/probe/molweight.html> (accessed April 2024).

Cox, R.T., and Van Arsdale, R.B., 2002, The Mississippi Embayment, North America: A First Order continental structure generated by the cretaceous superplume mantle event: Journal of Geodynamics, v. 34, p. 163–176, doi: 10.1016/s0264-3707(02)00019-4 (accessed November 2022).

Cox, R.T., Lowe, C., Hao, Y., and Mahan, S.A., 2014, Use of small-scale liquefaction features to assess paleoseismicity: An example from the Saline River Fault Zone, Southeast Arkansas, USA: Frontiers in Earth Science, v. 2, p. 2, doi: 10.3389/feart.2014.00031 (accessed November 2022).

Eby, G.N., and Vasconcelos, P., 2009, Geochronology of the Arkansas Alkaline Province, Southeastern United States: The Journal of Geology, v. 117, p. 615, 620-624, doi: 10.1086/605779.

Flohr, M.J., and Howard, J.M., 1994, Geochemical data of drill core samples of carbonatites and associated igneous rocks, Benton, Arkansas: Open-File Report, doi: 10.3133/ofr94450.

Geologic History, 2020, General Geology of Arkansas,  
<https://www.geology.arkansas.gov/geology/general-geology.html> (accessed August 2022).

Goldman, M.I., 1955, Petrography of bauxite surrounding a core of kaolinized nepheline syenite in Arkansas: Economic Geology, v. 50, p. 599–600, doi: 10.2113/gsecongeo.50.6.586 (August 2022).

Goldschmidt, V.M., 1937, The Seventh Hugo Muller Lecture, Delivered Before the Chemical Society, in The principles of distribution of chemical elements in minerals and rocks, London, Chemical Society Journal, p. 660-661, 665.

Google, (2022), Google Maps directions from Little Rock, AR to Bauxite, AR:  
<https://goo.gl/maps/okqN8g84paWkhV9r8> (accessed August 2022).

Gordon, M., and Murata, K.J., 1952, Minor elements in Arkansas bauxite: Economic Geology, v. 47, p. 169–179, doi: 10.2113/gsecongeo.47.2.169 (accessed August 2022).

Gordon, M., Ellis, M.W., and Tracey, J.I., 1958, Washington, D.C., U.S. Govt. Print. Off, p. 2-5, 11-15, 38-46, 71, 99-148 (accessed August 2020).

Guccione, M.J., 1993, Geologic History of Arkansas Through Time and Space: Fayetteville, AR, National Science Foundation, p. 8-36 (accessed August 2022).

Hafnium, 2021, Virginia Energy - geology and mineral resources - hafnium,  
[https://energy.virginia.gov/geology/Hafnium.shtml#:~:text=Hafnium%20is%20almost%20always%20found,mineral%20hafnon%20\(tableo%201\)](https://energy.virginia.gov/geology/Hafnium.shtml#:~:text=Hafnium%20is%20almost%20always%20found,mineral%20hafnon%20(tableo%201)) (accessed January 2024).

Haley, B.R., Glick, E.E., Bush, W.V., Clardy, B.F., Stone, C.G., Woodward, M.B., and Zachry, D.L., 1993, Explore this publication in the NGMDB: National Geologic Database, [https://ngmdb.usgs.gov/ProdDesc/proddesc\\_16308.htm](https://ngmdb.usgs.gov/ProdDesc/proddesc_16308.htm) (accessed September 2022).

Helmenstine, T., 2017, Free Printable periodic tables (pdf and PNG): Science Notes and Projects, <https://sciencenotes.org/printable-periodic-table/> (accessed February 2024).

- Howard J.M., 1987, Geology of the Saline County Xenolith and surrounding area, A.G.E.S. Brochure Series 005, p. 3-5, Arkansas Geological Survey, chrome-extension://efaidnbmnnibpcajpcglclefindmkaj/https://www.geology.arkansas.gov/docs/pdf/education/xenolith.pdf (accessed September 2022).
- Laerd Statistics, 2016a, Independent-samples t-test using Stata: Statistical tutorials and software guides, <https://statistics.laerd.com/> (accessed April 2024).
- Laerd Statistics, 2016b, Pearson's product-moment correlation using Stata: Statistical tutorials and software guides, <https://statistics.laerd.com/> (accessed April 2024).
- LaMorte, W. W. (2021). PH717 module 9 - correlation and regression. The Correlation Coefficient (r). <https://sphweb.bumc.bu.edu/otlt MPH-Modules/PH717-QuantCore/PH717-Module9-Correlation-Regression/PH717-Module9-Correlation-Regression4.html>
- Matton, G., and Jébrak, M., 2009, The cretaceous Peri-Atlantic Alkaline Pulse (PAAP): Deep mantle plume origin or shallow lithospheric break-up?: Tectonophysics, v. 469, p. 1–12, doi: 10.1016/j.tecto.2009.01.001 (accessed November 2022).
- McFarland, J.D., 1998, revised 2004, Little Rock, AR, Arkansas Geological Commission, p. 2, 15-35 (accessed September 2022).
- Mead, W.J., 1915, Occurrence and origin of the bauxite deposits of Arkansas: Economic Geology, v. 10, p. 29-31, 40-21, 44-45, doi: 10.2113/gsecongeo.10.1.28 (accessed September 2022).
- Nepheline Syenite, 2024, Office of the State Geologist, <https://www.geology.arkansas.gov/minerals/industrial/nepheline-syenite.html> (accessed January 2024).
- Paton, C., Hellstrom, J., Paul, B., Woodhead, J. and Hergt, J. (2011) lolite: Freeware for the visualisation and processing of mass spectrometric data. Journal of Analytical Atomic Spectrometry. doi:10.1039/c1ja10172b.
- Plebuch, R.O., and Hines, M.S., 1967, in Water Resources of Pulaski and saline counties, Arkansas, Washington, D.C, United States Gov. Print. Office.

Proctor, P.D., Peterson, P.R., and Kackstaetter, U., 1991, Mineral-Rock Handbook: Rapid-Easy Mineral-rock determination: Written for anyone interested in minerals and rocks: New York, Macmillan Pub. Co., p. 98, 100, 106, 108, 112, 160

QGIS - How To Calculate Surface/Cut Volume - Advanced, 2018, Points North GIS, <https://www.pointsnorthgis.ca/blog/how-to-calculate-surfacecut-volume-qgis-advanced/> (accessed May 2023).

Rudnick, R.L., and Gao, S., 2014, Composition of the continental crust: Treatise on Geochemistry, p. 1–51, doi: 10.1016/b978-0-08-095975-7.00301-6.

Schulte, R.F., and Foley, N.K., 2014, Reston, VA, United States Geological Survey, p. 3-9 (accessed August 2022).

Schulz, K.J., Piatak, N.M., and Papp, J.F., 2017, Niobium and tantalum, chap. M of Schulz, K.J., DeYoung, J.H., Jr., Seal, R.R., II, and Bradley, D.C., eds., Critical mineral resources of the United States—Economic and environmental geology and prospects for future supply: U.S. Geological Survey Professional Paper 1802, p. M1–M34, <https://doi.org/10.3133/pp1802M> (accessed January 2024).

Soil Survey Staff, 1999, Washington, DC, U.S. Dept. of Agriculture, Natural Resources Conservation Service, 436, p. 420, 549.

Stearn, N. H., 1930, A Geomagnetic Survey of the Bauxite Region in Central Arkansas, 1928-1929: State of Arkansas Geological Survey Bulletin 5, p. 1-4, 15, 16 (accessed September 2022).

Stone, C.G., Howard, J.M., and Haley, B.R., 1986, Little Rock, AR, Arkansas Geological Commission, p. 49 (accessed December 2022).

The National Atlas of the United States of America, 2015, U.S. Geological Survey, <https://www.usgs.gov/publications/national-atlas-united-states-america> (accessed December 2023).

Thomas, W.A., 1991, The Appalachian-Ouachita rifted margin of Southeastern North America: Geological Society of America Bulletin, v. 103, p. 415–431, doi: 10.1130/0016-7606(1991)103<0415:taormo>2.3.co;2 (accessed November 2022).

Thomas, W.A., 2006, Tectonic inheritance at a continental margin: GSA Today, v. 16, p. 4–10, doi: 10.1130/1052-5173(2006)016[4:tiaacm]2.0.co;2 (accessed November 2022).

How To Calculate Surface/Cut Volume QGIS - Advanced, 2018, Points North GIS, <https://www.pointsnorthandgis.ca/blog/how-to-calculate-surfacecut-volume-qgis-advanced/> (accessed May 2023).

United States Department of Agriculture, 2012, USDA, [https://www.nass.usda.gov/Publications/Highlights/2014/Farm\\_Economics/index.php](https://www.nass.usda.gov/Publications/Highlights/2014/Farm_Economics/index.php) (accessed December 2023).

USA rivers and streams, 2004, ArcGIS Hub, <https://hub.arcgis.com/datasets/esri::usa-rivers-and-streams> (accessed December 2023).

Valeton, I., 1972, Developments in soil science: New York, NY, Elsevier, p. 1, 3-8, 23, 43-44, 122-128.

Van Arsdale, R. B. (1998). Seismic hazards of the upper Mississippi embayment, U.S. Army Corps of Engineers Waterways Experiment Station Contract Report GL-98-1, 55 (accessed November 2022).

Van Gosen, B.S., and Choate, L.M., 2021, Reconnaissance study of the major and trace element content of bauxite deposits in the Arkansas bauxite region, Saline and Pulaski Counties, Central Arkansas: U.S. Geological Survey Open-File Report 2021-1073, 18 p. 2, 4-5, 16, <https://doi.org/10.3133/ofr20211073> (accessed August 2022).

Vogt, P.R., and Jung, W.-T. 2007, Origin of the Bermuda volcanoes and Bermuda Rise: history, observations, models, and puzzles, In Foulger, G.R., and Iurdy D. M., eds. Plates, plumes and planetary processes. Geol. Soc. Am. Spec. Pap., 430:553-591.

Wang, Y., Zhang, T.-an, Lyu, G., Guo, F., Zhang, W., and Zhang, Y., 2018, Recovery of alkali and alumina from bauxite residue (red mud) and complete reuse of the

treated residue: Journal of Cleaner Production, v. 188, p. 456–457, doi: 10.1016/j.jclepro.2018.04.009 (accessed August 2022).

Woodhead, J., Hellstrom, J., Hergt, J., Greig, A. & Maas, R (2007) Isotopic and elemental imaging of geological materials by laser ablation Inductively Coupled Plasma mass spectrometry. Journal of Geostandards and Geoanalytical Research, 31, p. 331-343.

Wysor, D.C., and Fermor, L.L., 1916, Aluminum hydrates in the Arkansas bauxite deposits: Economic Geology, v. 11, p. 43–44, 50, doi: 10.2113/gsecongeo.11.1.42 (accessed August 2022).

## **APPENDICES**

### **LIST OF APPENDICES**

Appendix A. The 2022 List of Critical Minerals and uses from the U.S. Geological Survey (Burton, 2022).....	106
Appendix B. UAV flight log and flight information .....	108
Appendix C. Sample locations with associated number. Tables have either SP or Clay, respectively before the number of the sample .....	122
Appendix D. Statistical data for Kriging .....	127
Appendix E. T-test results from volume calculations .....	139
Appendix F. Consolidated results from XRF analysis on Section 20 bauxite samples from Arkansas. ....	142
Appendix G. Compiled results from LA-ICP-MS analysis at TexasTech GeoAnalytical Laboratory for Section 20 bauxite samples Arkansas.....	172
Appendix H. Values used for comparing XRF and LA-ICP-MS analyses .....	177
Appendix I. Complete list of LA-ICP-MS percent greater values .....	182
Appendix J. Complete list of correlation coefficient values from scatterplots comparing all minerals tested versus Fe, Ti, and Al using XRF....	186
Appendix K. Pearson correlation values from scatterplots of Ti to elements using results from LA-ICP-MS on Section 20 bauxite samples from Arkansas. ....	189

Appendix A. The 2022 List of Critical Minerals and uses from the U.S. Geological Survey (modified from Burton, 2022).

The 2022 List of Critical Minerals		
Number	Mineral Name	Use
1	Aluminum	almost all sectors of the economy
2	Antimony	lead-acid batteries and flame retardants
3	Arsenic	semi-conductors
4	Barite	hydrocarbon production
5	Beryllium	alloying agent in aerospace and defense industries
6	Bismuth	medical and atomic research
7	Cerium	catalytic converters, ceramics, glass, metallurgy, and polishing compounds
8	Cesium	research and development
9	Chromium	primarily in stainless steel and other alloys
10	Cobalt	rechargeable batteries and superalloys
11	Dysprosium	permanent magnets, data storage devices and lasers
12	Erbium	fiber optics, optical amplifiers, lasers, and glass colorants
13	Europium	phosphors and nuclear control rods
14	Fluorspar	the manufacture of aluminum, cement, steel, gasoline, and fluorine chemicals
15	Gadolinium	medical imaging, permanent magnets and steel making
16	Gallium	integrated circuits and optical devices like LEDs
17	Germanium	fiber optics and night vision applications
18	Graphite	lubricants, batteries and fuel cells
19	Hafnium	nuclear control rods, alloys, and high-temperature ceramics
20	Holmium	permanent magnets, nuclear control rods and lasers
21	Indium	liquid crystal display screens
22	Iridium	coating of anodes for electrochemical processes and as a chemical catalyst
23	Lanthanum	to produce catalysts, ceramics, glass, polishing, metallurgy, and batteries
24	Lithium	rechargeable batteries
25	Lutetium	scintillators for medical imaging, electronics and some cancer therapies
26	Magnesium	alloy and for reducing metals
27	Manganese	steelmaking and batteries

28	Neodymium	permanent magnets, rubber catalysts and in medical and industrial lasers
29	Nickel	to make stainless steel, super alloy and rechargeable batteries
30	Niobium	mostly in steel and superalloys
31	Palladium	catalytic converters and as a catalyst agent
32	Platinum	catalytic converters
33	Praseodymium	permanent magnets, batteries, aerospace alloys, ceramics and colorants
34	Rhodium	catalytic converters, electrical components and as a catalyst
35	Rubidium	for research and development in electronics
36	Ruthenium	as catalysts, as well as electrical contacts and chip resistors in computers
37	Samarium	permanent magnets, as an absorber in nuclear reactors and in cancer treatments
38	Scandium	for alloys, ceramics and fuel cells
39	Tantalum	electronic components, mostly capacitors and in superalloys
40	Tellurium	solar cells, thermoelectric devices and as alloying additive
41	Terbium	permanent magnets, fiber optics, lasers and solid-state devices
42	Thulium	various metal alloys and in lasers
43	Tin	as protective coatings and alloys for steel
44	Titanium	as a white pigment or metal alloys
45	Tungsten	primarily to make wear-resistant metals
46	Vanadium	primarily as alloying agent for iron and steel
47	Ytterbium	for catalysts, scintillometers, lasers, and metallurgy
48	Yttrium	for ceramic, catalysts, lasers, metallurgy, and phosphors
49	Zinc	Primarily metallurgy to produce galvanized steel
50	Zirconium	the high-temperature ceramics and corrosion-resistant alloys

## Appendix B. UAV flight log and flight information.

### Flight 1:

Programmed Flight Altitude	43.70 m
Altitude ATL	Max: 104.00 m, Min: 0.00 m
Altitude ASL	Max: 229.40 m, Min: 125.40 m
Waypoints Programmed	90
Waypoints Visited	54
Overlap	75/75
Duration	1159 s
Takeoff Point Elevation	125.43 m
Max Range	315.57 m
Max Speed	15.54 m/s
Total Distance Flown	4.1 km
Satellites	Min: 13, Max: 16, Avg: 15
App Version	MPP_pro_5.4.15_031420232
App Device	Device: iPhone 12 iOS: 16.4.1
Terrain Source	SRTM
Manual Restart Point Used	No
Switched Out of Flight Mode	No
Virtual Stick	No

### Timestamps

Started	May 2, 2023, 12:47 p.m.
Finished	May 2, 2023, 1:06 p.m.
Uploaded	May 2, 2023, 1:06 p.m.

**Camera**

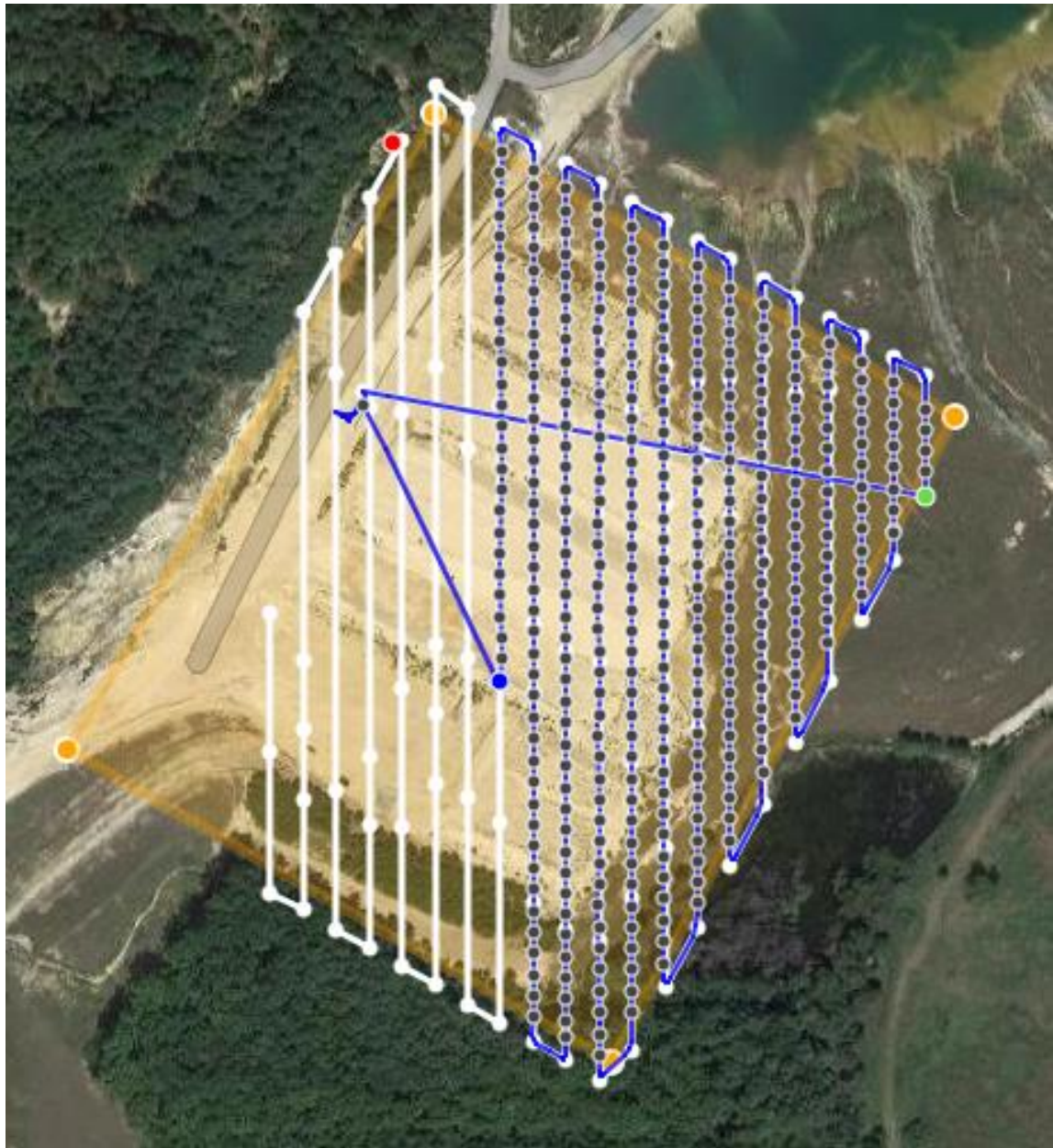
Camera	Mavic2ProCamera
Imaging Mode	Active Connect
Ground Smear	Max: 4.20 cm, Avg: 0.72 cm
Images Triggered	363
Images Received	362
Videos	0
Filename Range	DJI_0429.JPG to DJI_0790.JPG

**Aircraft**

Aircraft	Mavic 2 Pro
Aircraft Name	staffordk-Mavic2
Aircraft Firmware	01.00.0200
Aircraft Serial Number	163DFBM0016MJD
Aircraft Pitch	Max: 29.90°, Min: -32.60°
Aircraft Roll	Max: 26.70°, Min: -24.40°

**Battery**

Battery Temp	35 to 50°C
Battery Power	91% down to 16%
Battery Firmware	02.74.06.08
Battery Serial Number	0P2AFAP53405HS



## Flight 2:

Programmed Flight Altitude	43.60 m
Altitude ATL	Max: 105.10 m, Min: 0.00 m
Altitude ASL	Max: 230.30 m, Min: 125.20 m
Waypoints Programmed	90
Waypoints Visited	75
Overlap	75/75
Duration	1363 s
Takeoff Point Elevation	125.18 m
Max Range	301.67 m
Max Speed	12.28 m/s
Total Distance Flown	4.8 km
Satellites	Min: 13, Max: 16, Avg: 15
App Version	MPP_pro_5.4.15_031420232
App Device	Device: iPhone 12 iOS: 16.4.1
Terrain Source	SRTM
Manual Restart Point Used	No
Switched Out of Flight Mode	No
Virtual Stick	No

**Timestamps**

Started	May 2, 2023, 1:08 p.m.
Finished	May 2, 2023, 1:30 p.m.
Uploaded	May 2, 2023, 1:30 p.m.

**Camera**

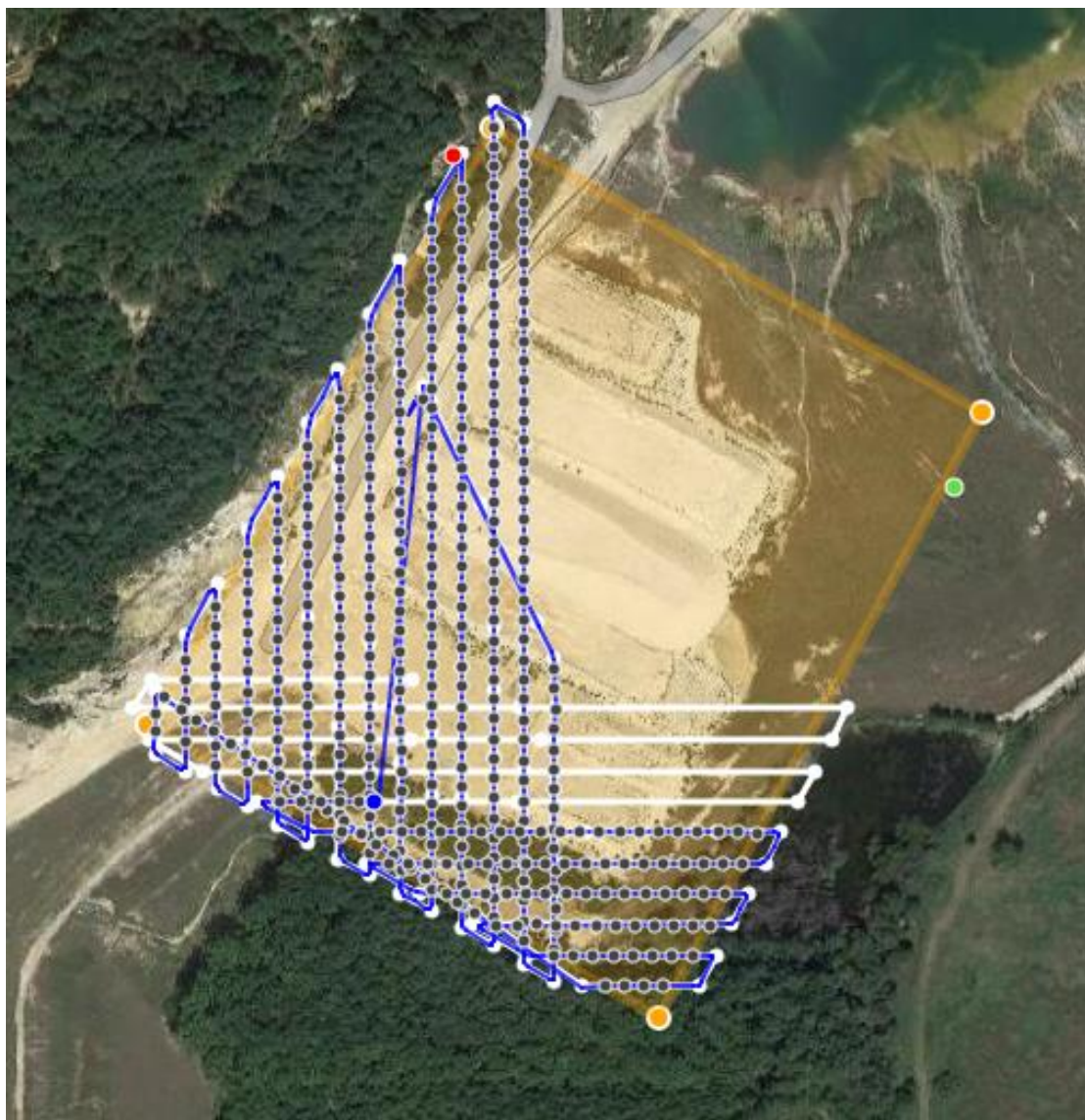
Camera	Mavic2ProCamera
Imaging Mode	Active Connect
Ground Smear	Max: 1.90 cm, Avg: 0.67 cm
Images Triggered	419
Images Received	417
Videos	0
Filename Range	DJI_0791.JPG to DJI_0208.JPG

**Aircraft**

Aircraft	Mavic 2 Pro
Aircraft Name	staffordk-Mavic2
Aircraft Firmware	01.00.0200
Aircraft Serial Number	163DFBM0016MJD
Aircraft Pitch	Max: 33.00°, Min: -34.20°
Aircraft Roll	Max: 38.30°, Min: -25.50°

## Battery

Battery Temp	31 to 49°C
Battery Power	100% down to 16%
Battery Firmware	02.74.06.08
Battery Serial Number	0P2AFBF53450LC



### Flight 3:

Programmed Flight Altitude	43.70 m
Altitude ATL	Max: 105.70 m, Min: 0.00 m
Altitude ASL	Max: 230.70 m, Min: 125.00 m
Waypoints Programmed	90
Waypoints Visited	54
Overlap	75/75
Duration	1312 s
Takeoff Point Elevation	124.99 m
Max Range	256.80 m
Max Speed	14.81 m/s
Total Distance Flown	4.7 km
Satellites	Min: 15, Max: 17, Avg: 17
App Version	MPP_pro_5.4.15_031420232
App Device	Device: iPhone 12 iOS: 16.4.1
Terrain Source	SRTM
Manual Restart Point Used	No
Switched Out of Flight Mode	No
Virtual Stick	No

**Timestamps**

Started	May 2, 2023, 1:31 p.m.
Finished	May 2, 2023, 1:53 p.m.
Uploaded	May 2, 2023, 1:53 p.m.

**Camera**

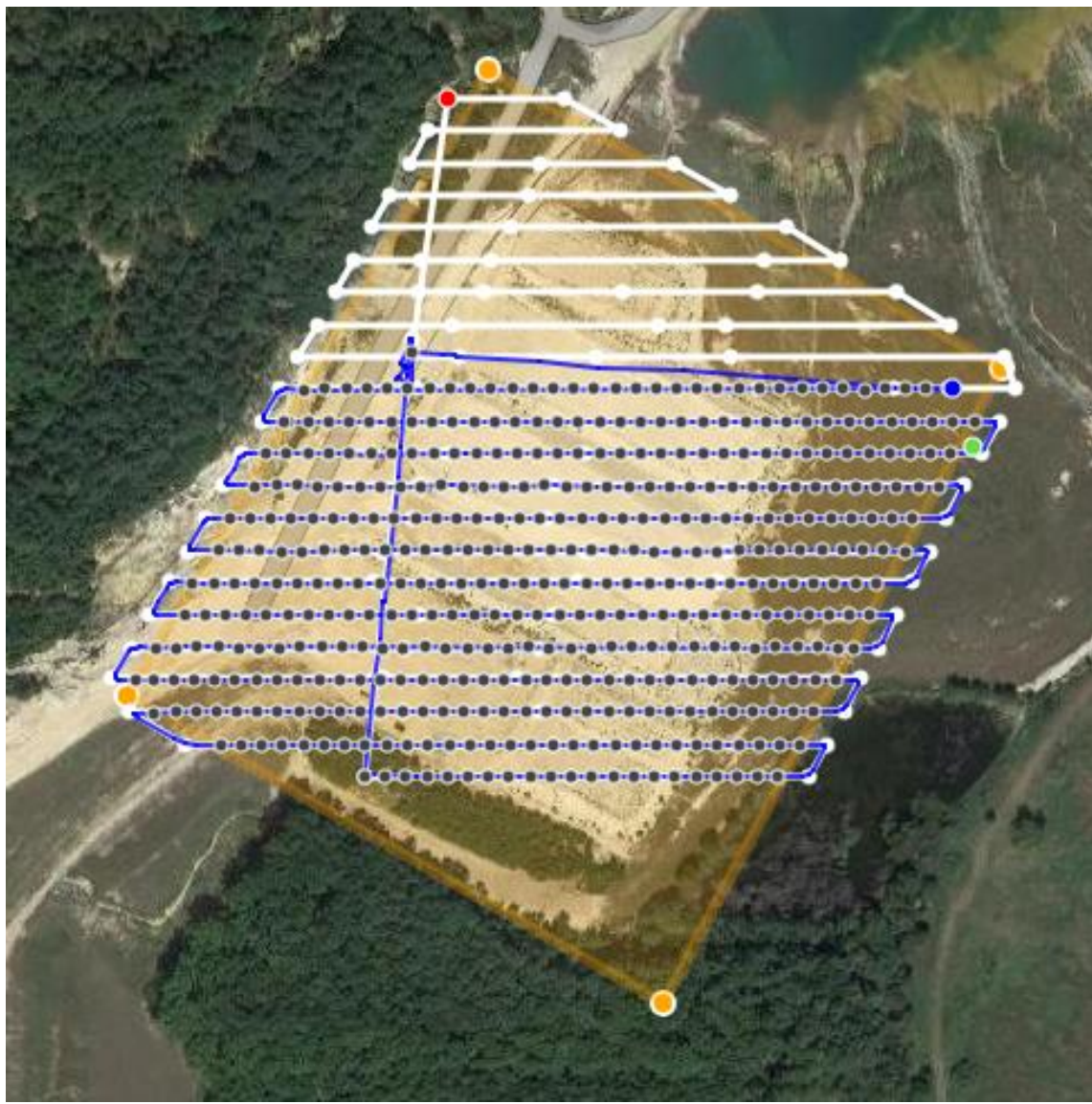
Camera	Mavic2ProCamera
Imaging Mode	Active Connect
Ground Smear	Max: 2.20 cm, Avg: 0.59 cm
Images Triggered	425
Images Received	424
Videos	0
Filename Range	DJI_0209.JPG to DJI_0632.JPG

**Aircraft**

Aircraft	Mavic 2 Pro
Aircraft Name	staffordk-Mavic2
Aircraft Firmware	01.00.0200
Aircraft Serial Number	163DFBM0016MJD
Aircraft Pitch	Max: 55.00°, Min: -34.10°
Aircraft Roll	Max: 25.50°, Min: -27.00°

**Battery**

Battery Temp	31 to 54°C
Battery Power	99% down to 14%
Battery Firmware	02.74.06.08
Battery Serial Number	0P2AFAP53405NY



#### Flight 4:

Programmed Flight Altitude	43.70 m
Altitude ATL	Max: 44.80 m, Min: 0.00 m
Altitude ASL	Max: 169.50 m, Min: 124.70 m
Waypoints Programmed	41
Waypoints Visited	40
Overlap	75/75
Duration	603 s
Takeoff Point Elevation	124.74 m
Max Range	262.72 m
Max Speed	14.44 m/s
Total Distance Flown	2.2 km
Satellites	Min: 16, Max: 17, Avg: 17
App Version	MPP_pro_5.4.15_031420232
App Device	Device: iPhone 12 iOS: 16.4.1
Terrain Source	SRTM
Manual Restart Point Used	No
Switched Out of Flight Mode	No
Virtual Stick	No

**Timestamps**

Started	May 2, 2023, 1:54 p.m.
Finished	May 2, 2023, 2:04 p.m.
Uploaded	May 2, 2023, 2:04 p.m.

**Camera**

Camera	Mavic2ProCamera
Imaging Mode	Active Connect
Ground Smear	Max: 3.30 cm, Avg: 0.72 cm
Images Triggered	171
Images Received	168
Videos	0
Filename Range	DJI_0633.JPG to DJI_0800.JPG

**Aircraft**

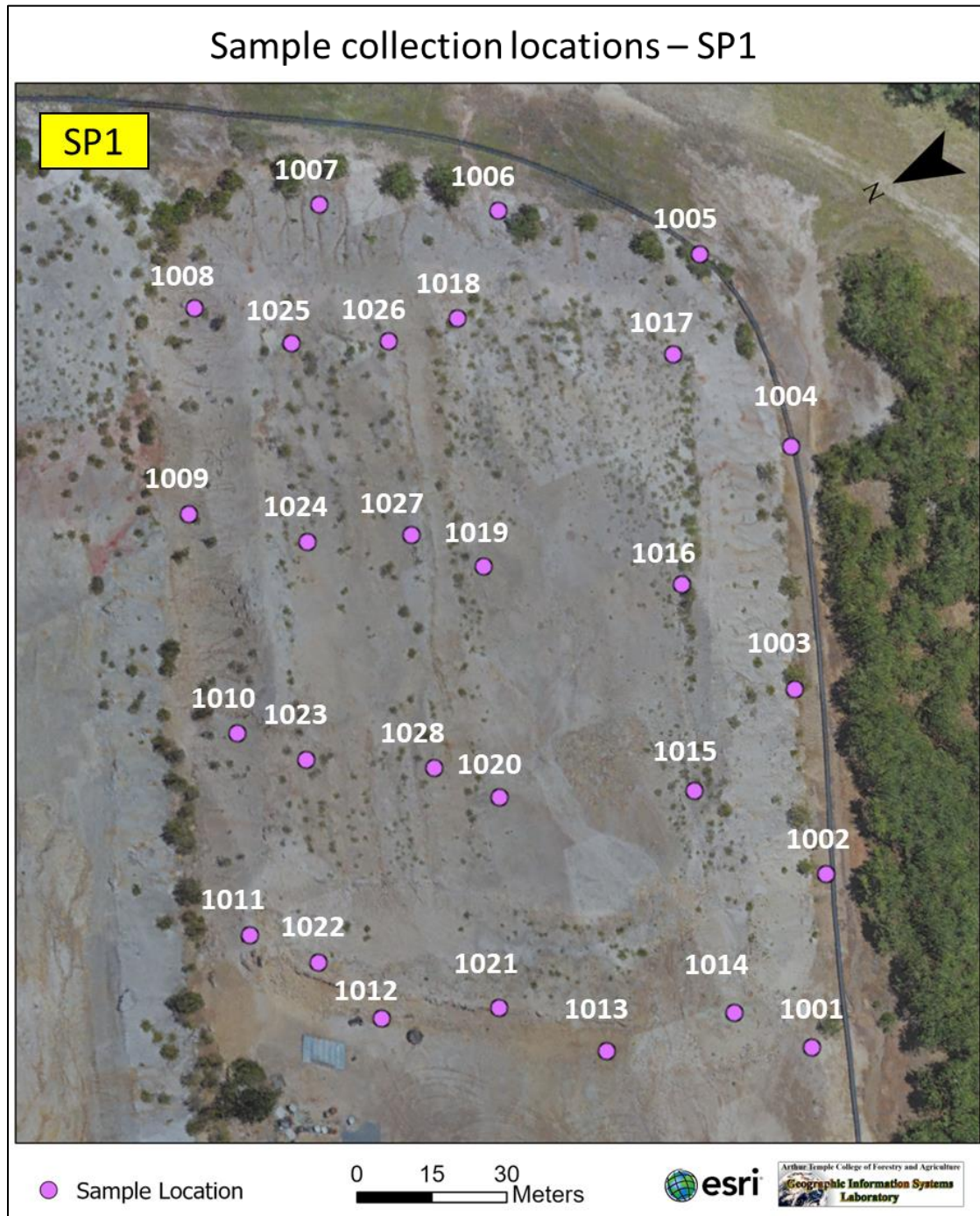
Aircraft	Mavic 2 Pro
Aircraft Name	staffordk-Mavic2
Aircraft Firmware	01.00.0200
Aircraft Serial Number	163DFBM0016MJD
Aircraft Pitch	Max: 24.20°, Min: -24.90°
Aircraft Roll	Max: 22.90°, Min: -25.40°

**Battery**

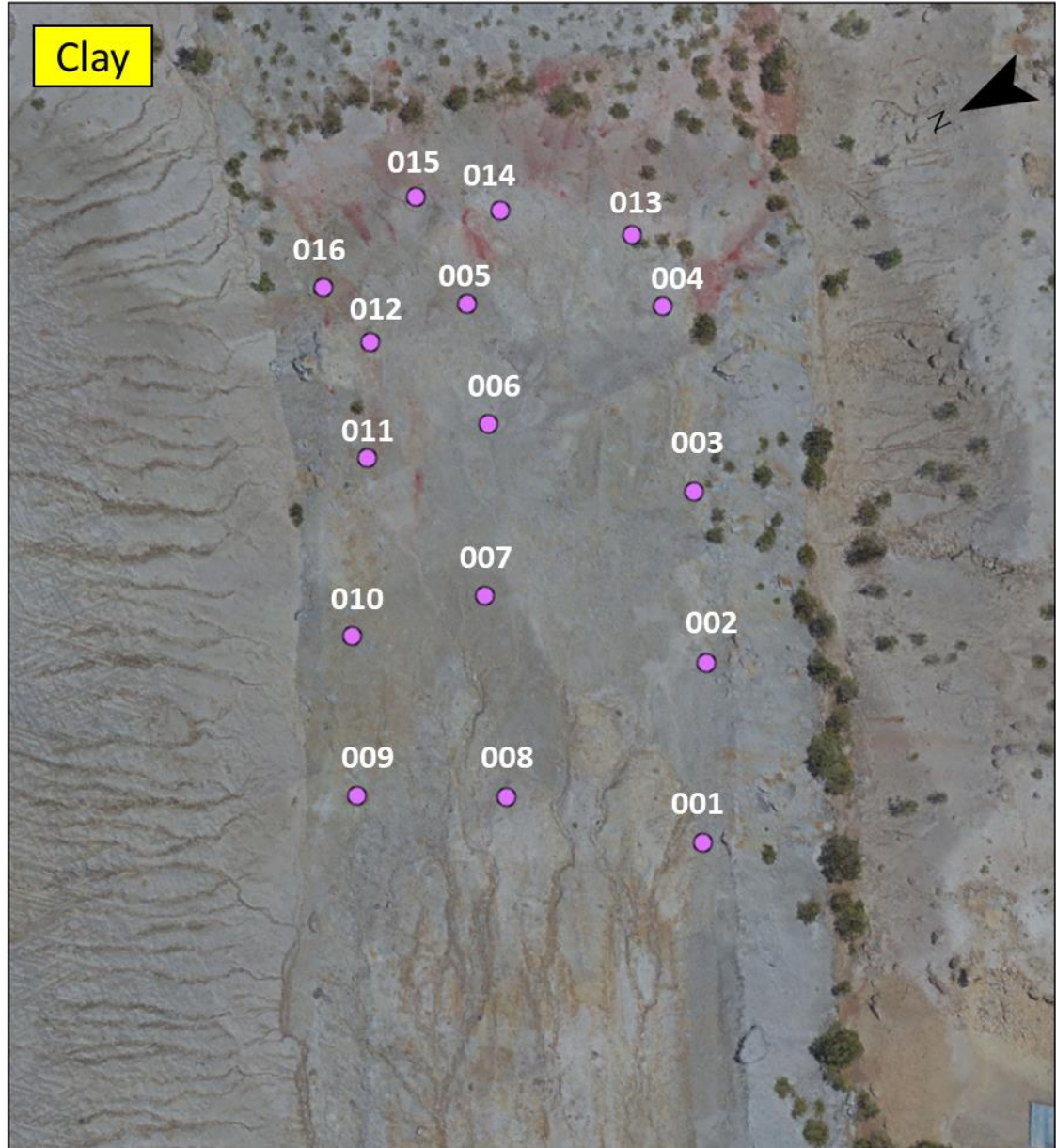
Battery Temp	30 to 44°C
Battery Power	100% down to 64%
Battery Firmware	02.74.06.08
Battery Serial Number	0P2AFB7534074V



Appendix C. Sample locations with associated number. Tables have either SP or Clay, respectively before the number of the sample.



## Sample collection locations – Clay



Arthur Temple College of Forestry and Agriculture  
Geographic Information Systems  
Laboratory

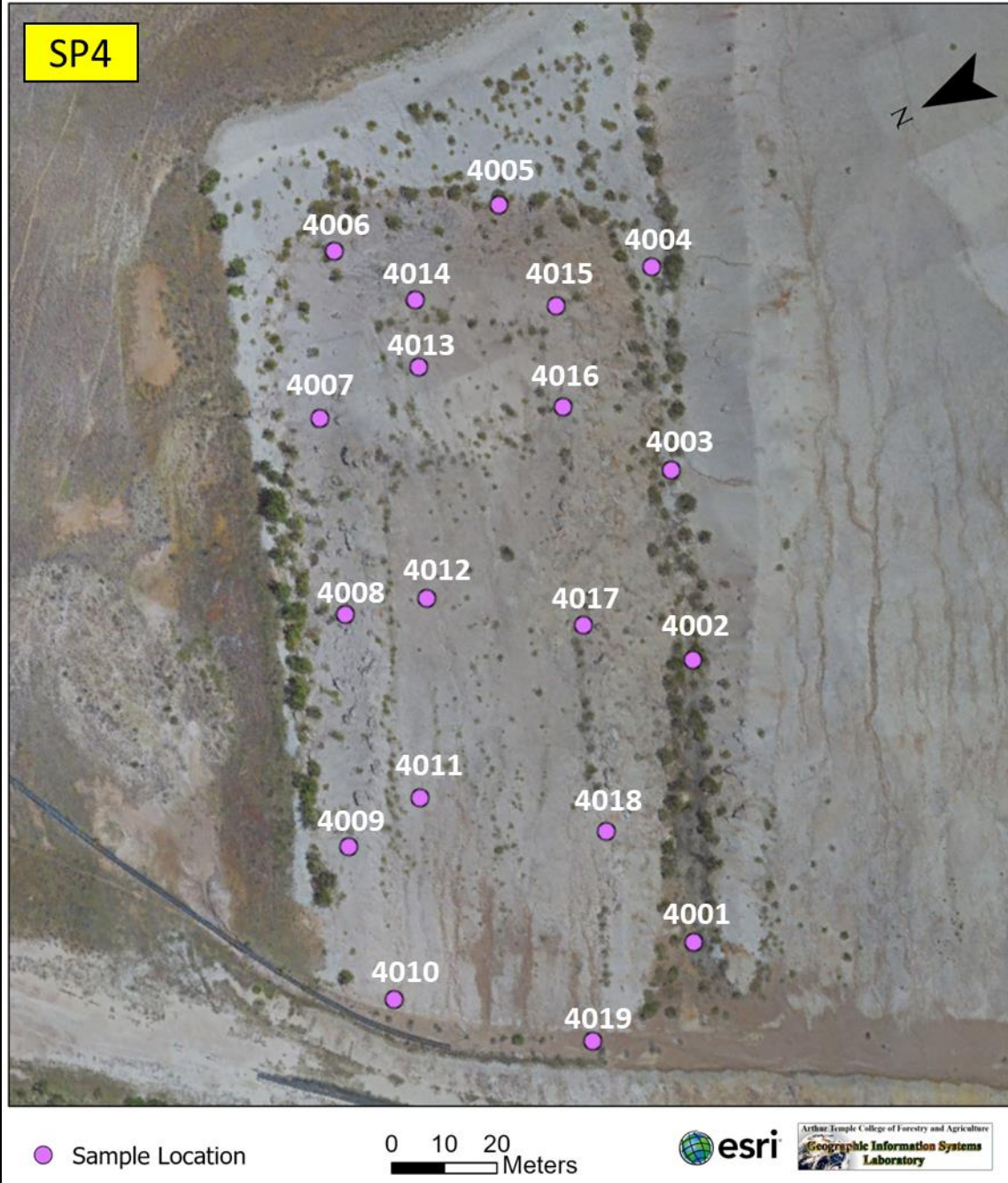
## Sample collection locations – SP2



### Sample collection locations – SP3



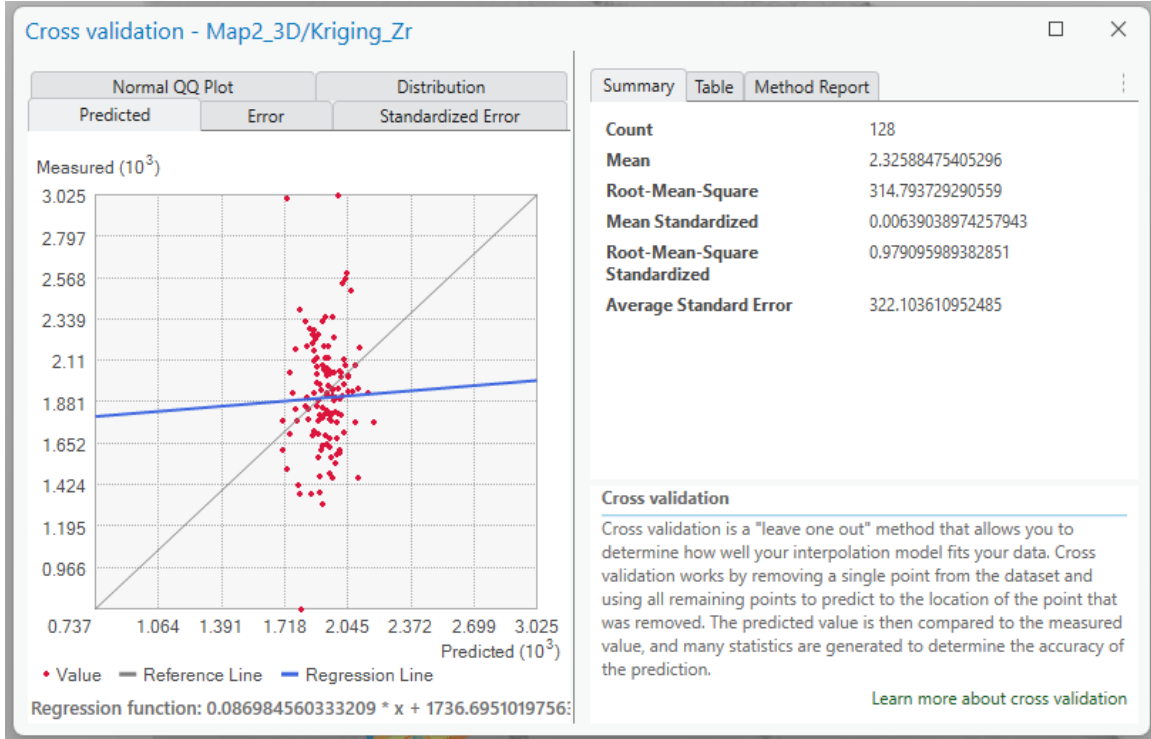
## Sample collection locations – SP4



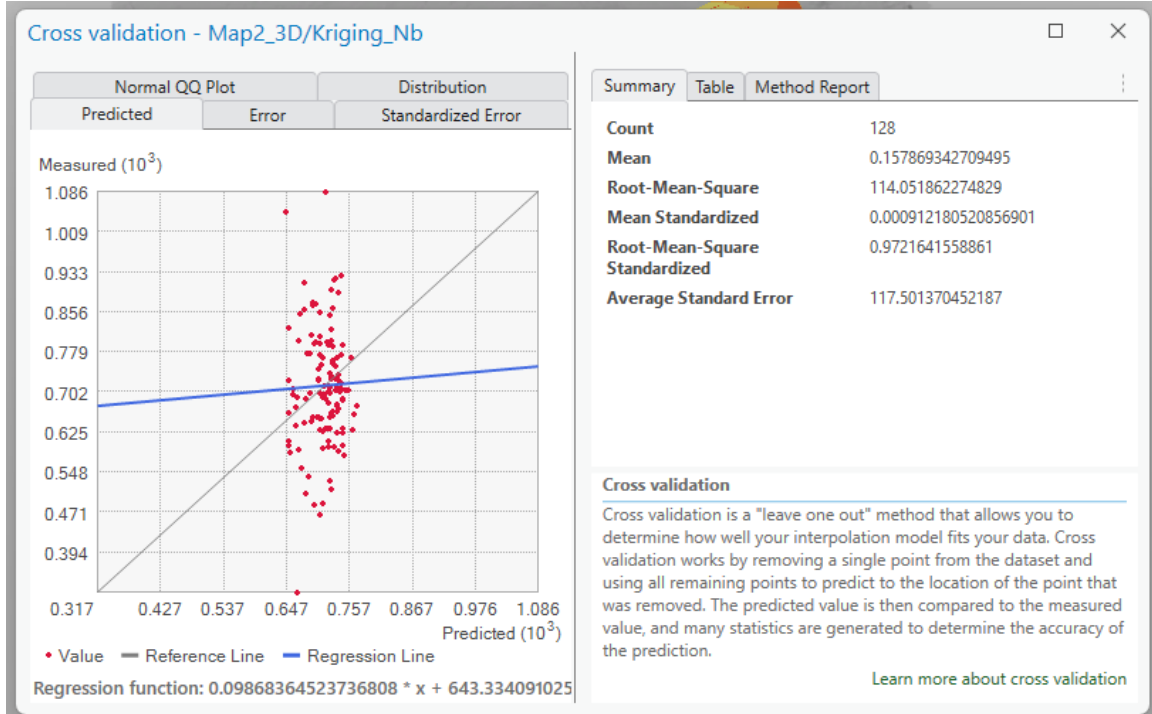
## Appendix D. Statistical data for Kriging method on spatial map.



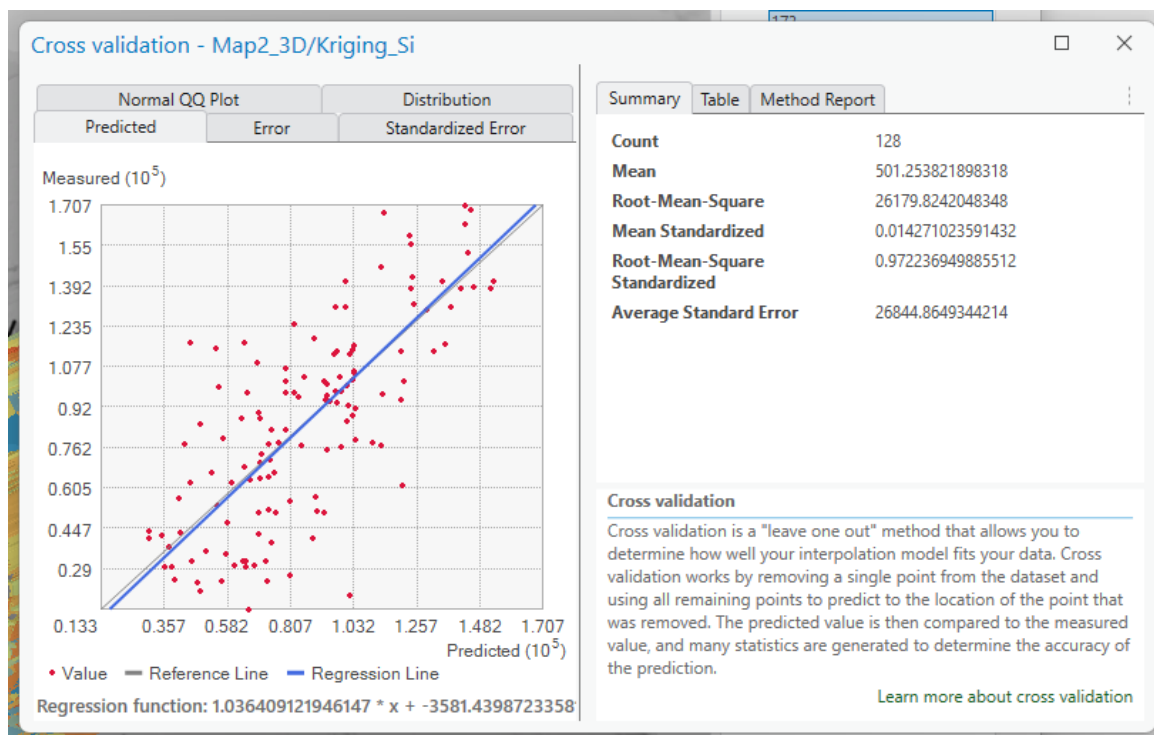
Strontium (Sr)			
Input datasets	Major semiaxis	Output type	147266.8786
-Dataset	0.000211986	Prediction	Measurement error %
C:\Users\melan\OneDrive\Documents\ArcGIS\Projects\Arkansas\Arkansas.gdb\All_new_elements	Minor semiaxis	-Dataset #	100
Type	0.000211986	1	-Model type
Feature Class	Angle	Trend type	Spherical
Data field 1	0	None	Range
Sr_calibrated_from_LAI_CPMs	-Variogram	-Searching neighborhood	0.000211986
Records	Semivariogram	Smooth	Anisotropy
128	Number of lags	Smoothing factor	No
-Method	12	0.2	Partial sill
Kriging	Lag size		0
Type	1.76655E-05		
Ordinary	Nugget		



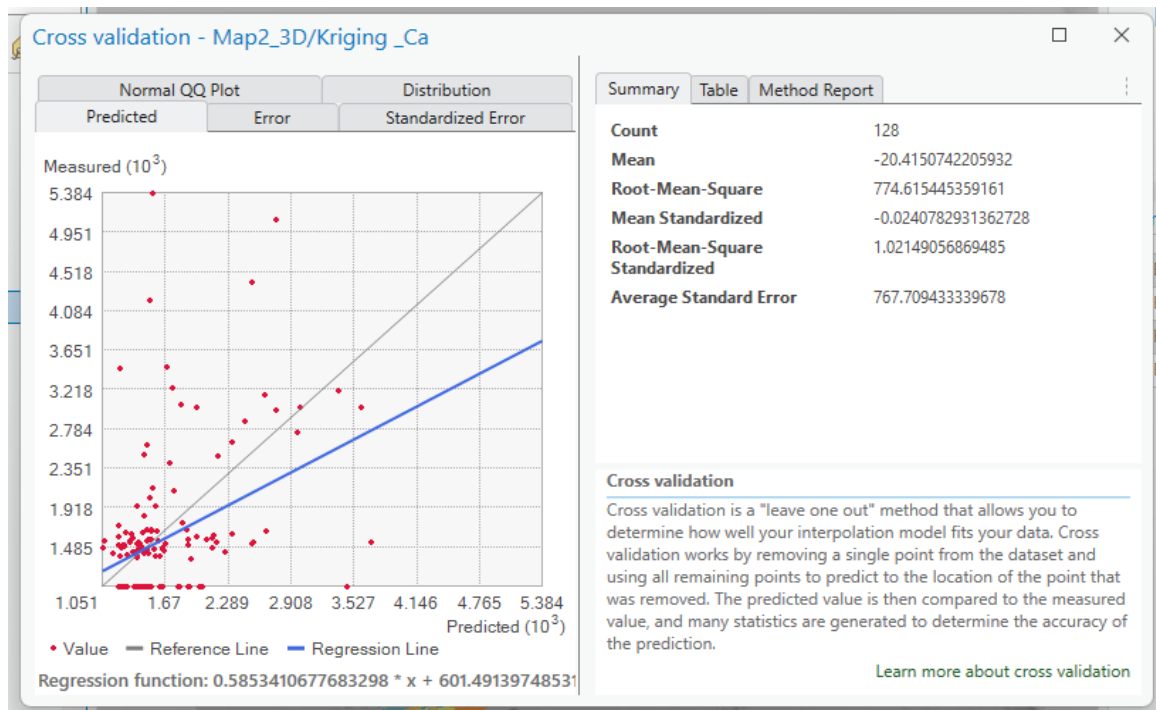
Zirconium (Zr)			
Input datasets	Major semiaxis	Output type	85848.24795
-Dataset	0.000430389	Prediction	Measurement error %
C:\Users\melan\OneDrive\Documents\ArcGIS\Projects\Arkansas\Arkansas.gdb\All_new_elements	Minor semiaxis	-Dataset #	100
Type	0.000430389	1	-Model type
Feature Class	Angle	Trend type	Spherical
Data field 1	0	None	Range
Zr_calibrated_from_LAICP MS	-Variogram	-Searching neighborhood	0.000430389
Records	Semivariogram	Smooth	Anisotropy
128	Number of lags	Smoothing factor	No
-Method	12	0.2	Partial sill
Kriging	Lag size		19581.32304
Type	3.58658E-05		
Ordinary	Nugget		



Niobium (Nb)			
Input datasets	Major semiaxis	Output type	12226.56795
-Dataset	0.000430389	Prediction	Measurement error %
C:\Users\melan\OneDrive\Documents\ArcGIS\Projects\Arkansas\Arkansas.gdb\All_new_elements	Minor semiaxis	-Dataset #	100
Type	0.000430389	1	-Model type
Feature Class	Angle	Trend type	Spherical
Data field 1	0	None	Range
Nb_calibrated_from_LAICPMS	-Variogram	-Searching neighborhood	0.000430389
Records	Semivariogram	Smooth	Anisotropy
128	Number of lags	Smoothing factor	No
-Method	12	0.2	Partial sill
Kriging	Lag size		1285.516617
Type	3.58658E-05		
Ordinary	Nugget		



Silicon (Si)			
Input datasets	Major semiaxis	Output type	407105106.5
-Dataset C:\Users\melan\OneDrive\Documents\ArcGIS\Projects\Arkansas\Arkansas.gdb\All_new_elements	0.00103285	Prediction	Measurement error %
Type	0.00103285	1	-Model type
Feature Class	Angle	Trend type	Spherical
Data field 1	0	None	Range
Si_calibrated_from_LICPMS	-Variogram	-Searching neighborhood	0.00103285
Records	Semivariogram	Smooth	Anisotropy
128	Number of lags	Smoothing factor	No
-Method	12	0.2	Partial sill
Kriging	Lag size		1418700890
Type	0.000145443		
Ordinary	Nugget		



Calcium (Ca)			
Input datasets	Major semiaxis	Output type	429693.1121
-Dataset	0.000189279	Prediction	Measurement error %
C:\Users\melan\OneDrive\Documents\ArcGIS\Projects\Arkansas\Arkansas.gdb\All_new_elements	Minor semiaxis	-Dataset #	100
Type	0.000189279	1	-Model type
Feature Class	Angle	Trend type	Spherical
Data field 1	0	None	Range
Ca_calibrated_from_LAICPMS	-Variogram	-Searching neighborhood	0.000189279
Records 128	Semivariogram	Smooth	Anisotropy
-Method Kriging	Number of lags	Smoothing factor	No
Type Ordinary	12	0.2	Partial sill
	Lag size		26868.04419
	1.76655E-05		
	Nugget		



Molybdenum (Mo)			
Input datasets	Major semiaxis	Output type	Measurement error %
-Dataset C:\Users\melan\OneDrive\Documents\ArcGIS\Projects\Arkansas\Arkansas.gdb\All_new_element	0.000308581	Prediction	100
Type	0.000308581	1	Spherical
Feature Class	Angle	Trend type	Range
Data field 1	0	None	0.000308581
Mo_calibrated_from_LAICPMS	-Variogram	-Searching neighborhood	Anisotropy
Records	Semivariogram	Smooth	No
128	Number of lags	Smoothing factor	Partial sill
	12	0.2	223.8755804
-Method	Lag size		
Kriging	5.11E-05		
Type	Nugget		
Ordinary	384.5705303		

Appendix E. T-test results for volume calculations with data from UAV, comparing ArcGIS (commercial software) and QGIS (open-source software) of stockpiles in Section 20, ALCOA bauxite mine, Arkansas.

#### SP1: t-Test results

t-Test: Two-Sample Assuming Unequal Variances		
	Variable 1	Variable 2
Mean	17878.33	18642.32
Variance	12842.63	3747.32
Observations	10	10
Hypothesized Mean Difference	0	
df	14	
t Stat	-18.75719588	
P(T<=t) one-tail	1.28061E-11	
t Critical one-tail	1.761310136	
P(T<=t) two-tail	2.56122E-11	
t Critical two-tail	2.144786688	

#### Clay: t-Test results

t-Test: Two-Sample Assuming Unequal Variances		
	Variable 1	Variable 2
Mean	1894.86	1947.80
Variance	1831.05	455.49
Observations	10	10
Hypothesized Mean Difference	0	
df	13	
t Stat	-3.501529473	
P(T<=t) one-tail	0.001951292	
t Critical one-tail	1.770933396	
P(T<=t) two-tail	0.003902584	
t Critical two-tail	2.160368656	

### SP2: t-Test results

t-Test: Two-Sample Assuming Unequal Variances		
	Variable 1	Variable 2
Mean	40980.21	42222.13
Variance	297566.62	13277.02
Observations	10	10
Hypothesized Mean Difference	0	
df	10	
t Stat	-7.044043087	
P(T<=t) one-tail	1.76189E-05	
t Critical one-tail	1.812461123	
P(T<=t) two-tail	0.000035238	
t Critical two-tail	2.228138852	

### SP3: t-Test results

t-Test: Two-Sample Assuming Unequal Variances		
	Variable 1	Variable 2
Mean	15229.62	15605.29
Variance	10315.44622	54281.23
Observations	10	10
Hypothesized Mean Difference	0	
df	12	
t Stat	-4.674174271	
P(T<=t) one-tail	0.000268811	
t Critical one-tail	1.782287556	
P(T<=t) two-tail	0.000537622	
t Critical two-tail	2.17881283	

#### SP4: t-Test results

t-Test: Two-Sample Assuming Unequal Variances		
	<i>Variable 1</i>	<i>Variable 2</i>
Mean	7457.717	7568.96211
Variance	1515.149846	2324.906025
Observations	10	10
Hypothesized Mean Difference	0	
df	17	
t Stat	-5.676911949	
P(T<=t) one-tail	1.36448E-05	
t Critical one-tail	1.739606726	
P(T<=t) two-tail	2.72897E-05	
t Critical two-tail	2.109815578	

Appendix F. Consolidated results from XRF analysis on Section 20 bauxite samples from Arkansas. Results are an average of three shots with the XRF per sample. Reference values for Earth's upper continental crust and NIST-698 sample (in red) at the top of each table.

Elemental XRF Values									
Sample	Nd*	Pr*	Ce*	La*	Ba*	Sb*	Sn*	Cd	Ag
Upper crust	27.0	7.1	63.0	31.0	624.0	0.40	2.10	0.09	53.00
NIST-698	138.32	34.91	300.00	218.16	71.65	0.00	0.00	9.45	0.00
SP1 matrix	0.00	0.00	154.40	83.82	72.24	0.00	0.00	0.00	0.00
Clay matrix	0.00	0.00	244.99	22.59	60.38	0.00	0.00	0.00	0.00
SP2 matrix	0.00	0.00	258.79	72.03	74.50	0.00	3.03	0.00	0.00
SP3 matrix	514.44	329.73	407.22	226.25	185.83	0.00	0.00	0.00	0.00
SP4 matrix	854.53	549.86	971.39	376.47	247.76	0.00	0.00	0.00	0.00
Clay red material	116.45	0.00	327.98	113.83	79.33	0.00	4.77	0.00	0.00
SP1 clasts	674.31	442.03	396.72	360.55	211.38	0.00	0.00	0.00	0.00
Clay clasts	1043.64	647.11	636.45	392.32	225.50	0.00	0.00	0.00	8.37
SP2 clasts	248.08	124.80	396.55	177.62	160.16	0.00	0.00	0.00	0.00
SP3 clasts	221.21	82.52	278.09	214.75	127.05	0.00	0.00	0.00	0.00
SP3 022 clast	763.89	487.58	735.52	321.49	214.33	0.00	0.00	0.00	0.00
SP3 032 clast	943.03	605.59	583.06	451.19	203.40	0.00	0.00	0.00	0.00
SP3 034 clast	669.08	437.70	405.05	291.36	176.45	0.00	6.74	0.00	0.00
SP4 clasts	235.25	132.07	445.89	111.14	72.73	0.00	0.00	0.00	0.00
SP1 matrix	0.00	0.00	154.40	83.82	72.24	0.00	0.00	0.00	0.00
Clay matrix	0.00	0.00	244.99	22.59	60.38	0.00	0.00	0.00	0.00

\*Critical element

<sup>1</sup>Empirical calibration of XRF result using LA-ICP-MS data

Elemental XRF Values								
Sample	Mo <sup>1</sup>	Nb* <sup>1</sup>	Th	Zr* <sup>1</sup>	Y*	Sr <sup>1</sup>	U	Rb* <sup>1</sup>
Upper crust	1.10	12.00	10.50	193.00	21.00	320.00	2.70	84.00
NIST-698	7.17	49.90	26.78	451.59	263.06	127.23	7.72	0.42
SP1 matrix	28.42	685.85	95.55	2038.19	7.47	430.50	15.01	0.00
Clay matrix	32.13	616.85	100.75	1793.01	8.21	199.55	11.51	0.39
SP2 matrix	48.23	708.84	152.28	2196.18	9.26	172.08	21.64	0.00
SP3 matrix	103.23	791.32	15.17	2512.06	5.18	118.25	14.83	0.00
SP4 matrix	16.04	717.19	41.60	2166.85	5.58	520.38	26.53	0.00
Clay red material	0.00	560.39	119.49	1518.37	10.87	140.43	0.00	0.23
SP1 clasts	4.42	311.48	28.94	847.68	5.15	59.95	0.00	0.00
Clay clasts	0.00	512.96	0.00	1476.54	1.61	212.01	0.00	0.00
SP2 clasts	20.16	503.87	103.45	1533.33	7.05	68.23	0.00	0.00
SP3 clasts	0.00	468.13	50.83	1438.76	7.11	547.98	0.00	0.00
SP3 022 clast	0.00	266.02	0.00	507.15	0.00	40.91	0.00	0.00
SP3 032 clast	2.27	369.78	21.42	733.08	1.04	49.88	0.00	0.00
SP3 034 clast	1.41	169.96	21.15	297.17	0.00	20.88	0.00	0.00
SP4 clasts	12.46	585.55	118.08	1769.77	9.10	575.39	26.59	0.00

\*Critical element  
<sup>1</sup>Empirical calibration of XRF result using LA-ICP-MS data

Elemental XRF Values									
Sample	Bi*	Au	Se	As*	Pb	W*	Zn*	Cu	Ni*
Upper crust	0.16	1.50	0.09	4.80	17.00	1.90	67.00	28.00	47.00
NIST-698	0.00	0.00	0.00	36.38	46.58	0.00	232.99	46.26	225.42
SP1 matrix	0.00	0.00	0.00	31.13	27.55	0.00	49.64	10.14	0.00
Clay matrix	0.00	0.00	0.00	30.50	50.50	0.00	7.80	0.00	0.00
SP2 matrix	0.00	0.00	0.00	39.25	51.08	0.00	24.72	12.75	0.00
SP3 matrix	0.00	0.00	0.00	167.24	65.31	0.00	33.48	0.00	0.00
SP4 matrix	0.00	0.00	0.00	136.22	48.22	0.00	76.45	38.39	46.72
Clay red material	0.00	0.00	0.00	45.20	21.98	0.00	141.98	38.90	0.00
SP1 clasts	0.00	0.00	0.00	15.34	0.00	0.00	32.21	9.32	0.00
Clay clasts	0.00	0.00	0.00	168.41	9.87	0.00	20.17	0.00	0.00
SP2 clasts	0.00	0.00	0.00	35.91	5.99	0.00	17.13	37.41	0.00
SP3 clasts	0.00	0.00	0.00	20.53	0.00	17.24	56.54	0.00	0.00
SP3 022 clast	0.00	0.00	0.00	12.59	0.00	0.00	23.80	0.00	0.00
SP3 032 clast	0.00	0.00	0.00	19.05	0.00	0.00	31.96	0.00	0.00
SP3 034 clast	0.00	0.00	0.00	21.75	21.44	0.00	37.80	0.00	28.28
SP4 clasts	0.00	0.00	0.00	89.39	28.33	0.00	114.69	50.69	0.00

\*Critical element  
<sup>1</sup>Empirical calibration of XRF result using LA-ICP-MS data

Elemental XRF Values							
Sample	Co*	Fe	Mn*	Cr*	V*	Ti*	Ca <sup>1</sup>
Upper crust	17.30	39176.47	774.46	92.00	97.00	3836.85	25657.77
NIST-698	45.00	152352.96	2942.94	547.36	358.51	14268.29	4431.15
SP1 matrix	0.00	36575.42	0.00	0.00	0.00	13911.62	0.00
Clay matrix	0.00	26295.89	0.00	0.00	0.00	14881.40	0.00
SP2 matrix	0.00	17035.25	0.00	0.00	0.00	16317.82	0.00
SP3 matrix	0.00	182564.59	0.00	0.00	0.00	9608.95	0.00
SP4 matrix	0.00	259088.45	2790.92	0.00	0.00	9666.55	0.00
Clay red material	0.00	30206.35	0.00	0.00	0.00	14351.40	0.00
SP1 clasts	0.00	173450.16	0.00	0.00	0.00	11758.75	459.26
Clay clasts	0.00	401917.94	1190.08	0.00	0.00	0.00	0.00
SP2 clasts	0.00	66070.30	0.00	0.00	0.00	14582.05	285.50
SP3 clasts	0.00	98809.36	0.00	0.00	0.00	11441.06	0.00
SP3 022 clast	0.00	310260.22	3586.02	0.00	0.00	0.00	72.95
SP3 032 clast	0.00	284717.23	1766.95	0.00	0.00	0.00	27.82
SP3 034 clast	0.00	208072.73	4921.15	0.00	0.00	0.00	123.85
SP4 clasts	0.00	61561.68	0.00	0.00	0.00	15908.31	468.62

\*Critical element  
<sup>1</sup>Empirical calibration of XRF result using LA-ICP-MS data

Elemental XRF Values							
Sample	K	Al <sup>1</sup> *	P	Si <sup>1</sup>	Cl	S	Mg*
Upper crust	23244.12	81504.65	654.63	311407.86	370.00	621.00	14955.29
NIST-698	83.01	255098.98	1614.76	3225.33	0.00	572.66	349.76
SP1 matrix	832.07	117039.44	0.00	44018.93	0.00	850.79	2294.35
Clay matrix	0.00	142355.18	0.00	136909.29	0.00	259.71	3143.13
SP2 matrix	0.00	140737.93	0.00	111301.75	0.00	272.77	4228.28
SP3 matrix	0.00	205870.56	2864.23	96873.54	0.00	339.56	2794.51
SP4 matrix	0.00	189076.76	0.00	47783.95	0.00	498.45	2864.04
Clay red material	391.14	141510.47	0.00	150387.36	0.00	203.10	3918.08
SP1 clasts	194.67	158300.98	0.00	24623.82	0.00	7918.67	5350.18
Clay clasts	0.00	161859.10	0.00	133570.25	0.00	186.04	6542.70
SP2 clasts	0.00	183685.31	0.00	71609.39	0.00	2075.29	6459.55
SP3 clasts	653.81	135463.75	1055.77	87379.54	0.00	2714.52	2301.12
SP3 022 clast	0.00	193955.74	0.00	40431.95	0.00	682.25	680.88
SP3 032 clast	0.00	186239.49	1316.25	43359.56	0.00	903.89	6732.89
SP3 034 clast	0.00	194600.50	130.42	22555.46	0.00	646.15	2518.63
SP4 clasts	179.77	165221.30	0.00	21390.84	0.00	659.46	1511.71

\*Critical element

<sup>1</sup>Empirical calibration of XRF result using LA-ICP-MS data

Elemental XRF Values									
Sample	Nd*	Pr*	Ce*	La*	Ba*	Sb*	Sn*	Cd	Ag
Upper crust	27.00	7.10	63.00	31.00	624.00	0.40	2.10	0.09	53.00
NIST-698	138.32	34.91	300.00	218.16	71.65	0.00	0.00	9.45	0.00
SP1 001	0.00	0.00	261.31	0.00	13.97	8.74	5.89	0.00	1.69
SP1 002	171.93	64.36	394.77	87.65	88.18	0.00	0.00	0.00	0.00
SP1 003	304.48	157.06	376.23	163.00	118.88	0.00	0.00	0.00	0.00
SP1 004	0.00	0.00	300.05	38.24	49.17	0.00	0.00	0.00	0.00
SP1 005	0.00	0.00	152.24	23.64	32.42	0.00	4.68	0.00	0.00
SP1 006	0.00	0.00	261.04	0.00	15.64	0.00	6.85	2.44	0.00
SP1 007	0.00	0.00	110.92	0.00	0.00	0.00	9.73	0.00	0.00
SP1 008	259.29	174.37	290.59	139.68	97.12	0.00	0.00	0.00	0.00
SP1 009	0.00	0.00	121.71	0.00	0.00	0.00	10.71	0.00	0.00
SP1 010	0.00	0.00	200.31	41.27	37.39	0.00	0.00	0.00	0.00
SP1 011	234.46	148.14	319.72	133.96	97.22	0.00	0.00	0.00	0.00
SP1 012	389.19	221.87	319.46	175.59	128.46	0.00	0.00	0.00	0.00
SP1 013	208.82	139.90	525.31	95.25	111.52	0.00	0.00	0.00	0.00
SP1 014	0.00	0.00	17.46	0.00	0.00	3.96	11.06	0.00	0.00
SP1 015	91.29	86.00	258.79	93.74	78.36	0.00	0.00	0.00	0.00
SP1 016	0.00	25.24	386.09	53.55	64.74	0.00	0.00	0.00	0.00
SP1 017	0.00	0.00	198.87	0.00	0.00	0.00	15.39	0.00	0.00
SP1 018	0.00	0.00	75.65	0.00	0.00	0.00	4.27	0.00	0.00
SP1 019	0.00	0.00	160.22	0.00	0.00	0.00	0.00	0.00	0.00
SP1 020	0.00	0.00	108.73	0.00	340.74	0.00	0.00	0.00	0.00
SP1 021	81.32	45.34	191.93	78.91	63.99	0.00	0.00	0.00	0.00
SP1 022	0.00	0.00	166.05	0.00	42.54	0.00	0.00	0.00	1.36
SP1 023	144.40	57.13	599.68	197.91	148.43	0.00	0.00	0.00	0.00
SP1 024	0.00	0.00	0.00	0.00	0.00	0.00	13.80	5.36	1.67
SP1 025	0.00	0.00	396.62	0.00	0.00	0.00	4.88	0.00	0.00
SP1 026	0.00	0.00	188.54	0.00	0.00	0.00	0.00	0.00	0.00
SP1 027	0.00	0.00	92.11	0.00	0.00	0.00	4.49	0.00	0.00
SP1 028	0.00	0.00	196.54	43.16	15.03	0.00	5.18	0.00	0.00

\*Critical element

<sup>1</sup>Empirical calibration of XRF result using LA-ICP-MS data

Elemental XRF Values								
Sample	Mo <sup>1</sup>	Nb* <sup>1</sup>	Th	Zr* <sup>1</sup>	Y*	Sr <sup>1</sup>	U	Rb* <sup>1</sup>
Upper crust	1.10	12.00	10.50	193.00	21.00	320.00	2.70	84.00
NIST-698	7.17	49.90	26.78	451.59	263.06	127.23	7.72	0.42
SP1 001	108.34	704.63	142.64	1954.26	7.57	166.93	9.73	0.00
SP1 002	5.58	550.00	62.07	1582.76	5.53	178.39	7.05	0.00
SP1 003	14.28	581.84	53.25	1611.08	6.51	212.45	0.00	0.00
SP1 004	7.06	574.90	122.35	1641.35	6.38	118.74	10.62	0.00
SP1 005	32.45	524.97	131.84	1392.41	4.91	78.34	14.31	0.00
SP1 006	0.00	628.89	76.11	1784.96	6.35	93.49	7.07	0.00
SP1 007	135.78	721.63	157.93	2015.26	8.03	175.32	18.26	0.00
SP1 008	54.75	588.89	70.40	1606.03	6.03	103.47	2.88	0.00
SP1 009	94.00	633.40	133.53	1809.27	6.86	71.09	10.86	0.11
SP1 010	2.83	660.13	115.63	1819.73	6.86	82.68	3.71	0.00
SP1 011	0.00	633.70	68.31	1737.42	6.21	118.45	3.40	0.00
SP1 012	5.28	572.94	69.18	1604.79	6.04	157.10	0.00	0.00
SP1 013	0.64	554.03	53.34	1502.08	5.35	459.23	11.70	0.00
SP1 014	21.84	608.20	81.38	1732.10	7.10	134.38	11.69	0.00
SP1 015	7.40	552.20	59.40	1618.08	6.17	126.09	6.10	0.00
SP1 016	15.08	589.46	62.58	1711.64	5.88	155.80	3.93	0.00
SP1 017	195.58	650.04	137.71	1812.37	7.13	82.50	15.13	0.00
SP1 018	22.64	617.79	116.46	1776.40	7.55	175.83	18.39	0.00
SP1 019	3.28	599.24	67.55	1687.92	6.64	163.54	7.37	0.00
SP1 020	0.00	582.59	30.33	1782.46	8.65	3579.55	30.41	0.00
SP1 021	4.21	590.56	77.30	1701.03	6.35	164.19	7.86	0.00
SP1 022	9.50	649.95	141.36	1951.86	8.54	776.44	22.36	0.00
SP1 023	14.56	573.90	118.97	1717.74	6.91	1105.40	31.42	0.00
SP1 024	34.58	645.51	126.68	1904.59	9.27	110.66	17.09	0.00
SP1 025	66.17	601.60	104.82	1666.24	6.79	205.09	15.41	0.00
SP1 026	9.18	508.55	105.59	1438.22	6.48	214.51	16.56	0.00
SP1 027	4.74	604.27	82.27	1709.65	6.69	103.04	9.37	0.00
SP1 028	0.00	754.39	0.00	1792.99	7.00	64.58	0.00	0.00

\*Critical element

<sup>1</sup>Empirical calibration of XRF result using LA-ICP-MS data

Elemental XRF Values									
Sample	Bi*	Au	Se	As*	Pb	W*	Zn*	Cu	Ni*
Upper crust	0.16	1.50	0.09	4.80	17.00	1.90	67.00	28.00	47.00
NIST-698	0.00	0.00	0.00	36.38	46.58	0.00	232.99	46.26	225.42
SP1 001	0.00	0.00	0.00	358.65	0.00	0.00	0.00	11.13	0.00
SP1 002	0.00	0.00	0.00	12.55	0.00	0.00	19.54	11.89	0.00
SP1 003	0.00	0.00	0.00	35.10	0.00	0.00	34.91	27.78	0.00
SP1 004	0.00	0.00	0.00	67.73	0.00	0.00	14.65	0.00	0.00
SP1 005	0.00	124.20	47.02	67.83	0.00	0.00	175.56	246.48	60.54
SP1 006	0.00	0.00	0.00	14.95	0.00	0.00	29.57	10.41	0.00
SP1 007	0.00	0.00	0.00	90.21	0.00	0.00	3.45	0.00	0.00
SP1 008	0.00	0.00	0.00	80.10	0.00	0.00	12.70	11.01	0.00
SP1 009	0.00	0.00	0.00	48.20	39.93	0.00	59.50	0.00	0.00
SP1 010	0.00	0.00	0.00	23.22	3.86	0.00	27.41	10.40	0.00
SP1 011	0.00	0.00	0.00	24.47	22.20	0.00	35.78	28.14	0.00
SP1 012	0.00	0.00	0.00	113.75	27.52	0.00	31.45	35.65	0.00
SP1 013	0.00	0.00	0.00	17.56	5.08	0.00	17.20	28.82	0.00
SP1 014	0.00	0.00	0.00	98.33	23.65	0.00	0.00	12.57	0.00
SP1 015	0.00	0.00	0.00	16.33	20.07	0.00	47.19	24.45	0.00
SP1 016	0.00	0.00	0.00	13.48	21.85	0.00	43.95	0.00	0.00
SP1 017	0.00	0.00	0.00	105.32	21.28	0.00	33.66	13.02	0.00
SP1 018	0.00	0.00	0.00	44.22	43.63	0.00	37.41	0.00	0.00
SP1 019	0.00	0.00	0.00	14.38	15.39	0.00	8.57	8.83	0.00
SP1 020	0.00	0.00	0.00	94.12	14.29	0.00	0.00	0.00	0.00
SP1 021	0.00	0.00	0.00	17.89	23.48	0.00	24.60	10.50	0.00
SP1 022	0.00	0.00	0.00	25.88	40.00	0.00	4.74	0.00	0.00
SP1 023	0.00	0.00	0.00	28.00	37.86	0.00	3.85	7.44	0.00
SP1 024	0.00	0.00	0.00	86.43	32.18	0.00	102.69	0.00	0.00
SP1 025	0.00	0.00	0.00	55.24	32.21	0.00	49.19	21.93	0.00
SP1 026	0.00	0.00	0.00	24.25	38.61	0.00	24.56	0.00	0.00
SP1 027	0.00	0.00	0.00	40.20	26.43	0.00	28.18	0.00	0.00
SP1 028	0.00	0.00	0.00	0.00	0.00	0.00	0.00	0.00	0.00

\*Critical element

<sup>1</sup>Empirical calibration of XRF result using LA-ICP-MS data

Elemental XRF Values							
Sample	Co*	Fe	Mn*	Cr*	V*	Ti*	Ca <sup>1</sup>
Upper crust	17.30	39176.47	774.46	92.00	97.00	3836.85	25657.77
NIST-698	45.00	152352.96	2942.94	547.36	358.51	14268.29	4431.15
SP1 001	0.00	12594.23	0.00	0.00	0.00	18148.03	0.00
SP1 002	0.00	54301.81	0.00	0.00	0.00	12245.25	0.00
SP1 003	0.00	94120.41	0.00	0.00	0.00	12701.90	0.00
SP1 004	0.00	23508.78	0.00	0.00	0.00	11932.21	0.00
SP1 005	354.87	28795.74	0.00	0.00	0.00	14088.70	0.00
SP1 006	0.00	30291.58	0.00	0.00	0.00	12214.38	0.00
SP1 007	0.00	10405.96	0.00	0.00	0.00	15399.41	0.00
SP1 008	0.00	77143.37	0.00	0.00	0.00	13189.99	0.00
SP1 009	0.00	11356.30	0.00	0.00	0.00	11832.80	0.00
SP1 010	0.00	55374.70	0.00	0.00	0.00	13451.34	0.00
SP1 011	0.00	84858.97	0.00	0.00	0.00	13491.20	0.00
SP1 012	0.00	145580.75	0.00	0.00	0.00	11314.80	0.00
SP1 013	0.00	103252.30	0.00	0.00	0.00	11792.80	0.00
SP1 014	0.00	9805.32	0.00	0.00	0.00	13542.49	0.00
SP1 015	0.00	74321.01	0.00	0.00	0.00	11544.49	0.00
SP1 016	0.00	55642.92	0.00	0.00	0.00	11923.02	0.00
SP1 017	0.00	25241.44	0.00	0.00	0.00	13584.71	0.00
SP1 018	0.00	11873.14	0.00	0.00	0.00	13162.03	0.00
SP1 019	0.00	26719.67	0.00	0.00	0.00	12793.27	0.00
SP1 020	0.00	14498.76	0.00	0.00	0.00	15591.07	348.24
SP1 021	0.00	49349.42	0.00	0.00	0.00	12048.03	0.00
SP1 022	0.00	15677.40	0.00	0.00	0.00	14978.77	0.00
SP1 023	0.00	46183.49	0.00	0.00	0.00	14542.23	146.05
SP1 024	0.00	12404.69	0.00	0.00	0.00	14657.68	0.00
SP1 025	0.00	35129.97	0.00	0.00	0.00	13197.90	0.00
SP1 026	0.00	9120.17	0.00	0.00	0.00	11999.05	0.00
SP1 027	0.00	12134.54	0.00	0.00	0.00	12767.31	0.00
SP1 028	0.00	56432.41	0.00	0.00	0.00	13623.40	0.00

\*Critical element

<sup>1</sup>Empirical calibration of XRF result using LA-ICP-MS data

Elemental XRF Values							
Sample	K	Al*	P	Si <sup>1</sup>	Cl	S	Mg*
Upper crust	23244.12	81504.65	654.63	311407.86	370.00	621.00	14955.29
NIST-698	83.01	255098.98	1614.76	3225.33	0.00	572.66	349.76
SP1 001	0.00	138745.17	0.00	75325.10	0.00	2095.89	2040.60
SP1 002	0.00	153699.30	0.00	56669.20	0.00	396.28	1755.65
SP1 003	0.00	167252.08	0.00	72993.46	0.00	400.88	2614.24
SP1 004	0.00	129738.07	0.00	76984.81	0.00	1574.06	1879.09
SP1 005	0.00	156079.43	0.00	48271.33	0.00	385.86	2516.80
SP1 006	50.77	163377.69	0.00	69320.15	0.00	507.32	2115.33
SP1 007	0.00	153417.92	0.00	34652.29	0.00	1432.19	2430.81
SP1 008	0.00	183308.17	0.00	31102.89	0.00	2878.11	2873.30
SP1 009	311.93	145322.20	0.00	93789.25	0.00	603.77	1563.53
SP1 010	0.00	177696.10	0.00	46628.43	0.00	338.20	2735.73
SP1 011	223.45	184338.21	0.00	78367.05	0.00	333.53	3034.36
SP1 012	0.00	205156.95	0.00	40194.91	0.00	985.09	4029.87
SP1 013	0.00	182615.27	0.00	35281.48	0.00	1820.10	1148.05
SP1 014	0.00	144703.55	0.00	87040.83	0.00	1976.90	1354.94
SP1 015	0.00	173107.96	0.00	95392.14	0.00	771.11	2327.34
SP1 016	0.00	173844.90	0.00	95380.98	0.00	310.51	1700.89
SP1 017	59.84	149827.75	0.00	69960.67	0.00	1080.28	2603.74
SP1 018	46.39	151951.74	0.00	90643.89	0.00	842.79	1536.40
SP1 019	0.00	156602.91	0.00	84746.74	0.00	611.18	2289.06
SP1 020	0.00	161167.11	4950.27	72915.19	0.00	1519.52	2174.63
SP1 021	0.00	170794.48	0.00	84652.65	0.00	750.90	3005.62
SP1 022	0.00	161187.42	0.00	36872.50	0.00	584.94	1968.11
SP1 023	0.00	182550.70	2049.74	37325.79	0.00	629.00	3244.02
SP1 024	63.03	151944.88	0.00	90769.47	0.00	2168.02	2060.73
SP1 025	176.68	179899.03	0.00	80441.74	0.00	566.64	2040.90
SP1 026	0.00	140898.21	0.00	117862.84	0.00	386.89	2670.79
SP1 027	193.40	157088.85	0.00	85068.41	0.00	771.40	1630.45
SP1 028	0.00	191167.36	0.00	35560.48	0.00	955.35	1735.52

\*Critical element

<sup>1</sup>Empirical calibration of XRF result using LA-ICP-MS data

Elemental XRF Values									
Sample	Nd*	Pr*	Ce*	La*	Ba*	Sb*	Sn*	Cd	Ag
Upper crust	27.00	7.10	63.00	31.00	624.00	0.40	2.10	0.09	53.00
NIST-698	138.32	34.91	300.00	218.16	71.65	0.00	0.00	9.45	0.00
Clay 001	0.00	0.00	113.72	39.89	13.47	0.00	0.00	0.00	0.00
Clay 002	103.43	43.02	123.04	84.25	71.05	0.00	0.00	0.00	0.00
Clay 003	0.00	0.00	179.28	113.00	53.68	0.00	0.00	0.00	0.00
Clay 004	191.84	115.99	216.29	156.99	107.57	0.00	0.00	0.00	0.00
Clay 005	118.11	82.33	178.00	117.95	93.74	0.00	0.00	0.00	0.00
Clay 006	79.12	0.00	166.19	89.42	55.74	0.00	0.00	0.00	0.00
Clay 007	34.56	22.30	109.05	85.17	37.73	0.00	5.03	0.00	0.00
Clay 008	0.00	0.00	88.96	19.17	0.00	0.00	0.00	0.00	0.00
Clay 009	0.00	0.00	139.51	82.23	27.01	0.00	5.07	0.00	0.00
Clay 010	0.00	0.00	69.11	62.81	14.79	0.00	0.00	0.00	0.00
Clay 011	0.00	0.00	44.85	17.42	0.00	0.00	0.00	0.00	0.00
Clay 012	269.01	177.52	356.66	190.38	126.80	0.00	0.00	0.00	0.00
Clay 013	66.30	27.44	145.85	91.52	57.59	0.00	0.00	0.00	0.00
Clay 014	0.00	0.00	0.00	0.00	0.00	0.00	5.15	0.00	0.00
Clay 015	596.10	343.21	379.56	283.86	184.54	0.00	0.00	0.00	0.00
Clay 016	176.02	101.03	302.77	225.12	147.54	0.00	0.00	0.00	0.00

\*Critical element

<sup>1</sup>Empirical calibration of XRF result using LA-ICP-MS data

Elemental XRF Values								
Sample	Mo <sup>1</sup>	Nb* <sup>1</sup>	Th	Zr* <sup>1</sup>	Y*	Sr <sup>1</sup>	U	Rb* <sup>1</sup>
Upper crust	1.10	12.00	10.50	193.00	21.00	320.00	2.70	84.00
NIST-698	7.17	49.90	26.78	451.59	263.06	127.23	7.72	0.42
Clay 001	6.70	427.75	80.97	1259.94	4.97	85.35	3.90	0.00
Clay 002	25.82	538.65	101.87	1628.13	6.43	66.98	6.15	0.00
Clay 003	1.23	571.57	97.32	1696.26	8.30	134.08	16.26	0.40
Clay 004	2.70	412.46	42.68	1343.15	6.28	82.91	0.00	1.06
Clay 005	23.84	465.90	46.12	1416.92	5.39	71.79	5.82	0.02
Clay 006	9.10	574.87	68.87	1640.66	6.43	85.90	5.48	0.00
Clay 007	5.16	535.81	54.00	1575.27	6.13	72.76	0.00	0.00
Clay 008	0.00	559.94	67.03	1629.13	6.45	125.02	0.00	0.00
Clay 009	0.00	552.53	70.61	1516.83	6.87	171.18	9.82	0.00
Clay 010	28.77	514.91	106.48	1575.72	5.73	63.67	0.00	0.00
Clay 011	17.49	597.42	110.11	1786.84	7.12	59.66	8.22	0.00
Clay 012	22.35	669.86	54.92	1889.47	7.26	88.23	7.94	0.00
Clay 013	57.40	634.43	56.24	1852.91	7.30	98.41	7.52	0.00
Clay 014	81.32	688.63	122.88	1980.11	10.98	120.78	18.64	0.18
Clay 015	0.00	651.63	14.71	1905.77	6.60	98.73	0.00	0.00
Clay 016	0.00	502.42	27.87	1254.60	6.05	177.52	0.00	0.00

\*Critical element

<sup>1</sup>Empirical calibration of XRF result using LA-ICP-MS data

Sample	Elemental XRF Values								
	Bi*	Au	Se	As*	Pb	W*	Zn*	Cu	Ni*
Upper crust	0.16	1.50	0.09	4.80	17.00	1.90	67.00	28.00	47.00
NIST-698	0.00	0.00	0.00	36.38	46.58	0.00	232.99	46.26	225.42
Clay 001	0.00	0.00	0.00	11.66	25.78	0.00	26.46	0.00	0.00
Clay 002	0.00	0.00	0.00	31.69	42.55	0.00	41.88	0.00	0.00
Clay 003	0.00	0.00	0.00	21.65	45.13	0.00	988.49	0.00	0.00
Clay 004	0.00	0.00	0.00	8.68	18.15	0.00	343.21	0.00	0.00
Clay 005	0.00	0.00	0.00	17.01	25.14	0.00	45.39	11.46	0.00
Clay 006	0.00	0.00	0.00	19.61	25.88	0.00	29.37	10.75	0.00
Clay 007	0.00	0.00	0.00	12.12	22.24	0.00	26.48	0.00	0.00
Clay 008	0.00	0.00	0.00	16.45	22.23	0.00	23.60	0.00	0.00
Clay 009	0.00	0.00	0.00	12.36	28.24	0.00	28.85	0.00	0.00
Clay 010	0.00	0.00	0.00	23.64	31.12	0.00	70.06	9.06	0.00
Clay 011	0.00	0.00	0.00	19.83	49.21	0.00	34.77	10.90	0.00
Clay 012	0.00	0.00	0.00	17.18	35.17	0.00	41.33	10.33	0.00
Clay 013	0.00	0.00	0.00	37.34	37.14	0.00	43.88	0.00	0.00
Clay 014	0.00	0.00	0.00	35.37	47.51	0.00	158.61	7.41	0.00
Clay 015	0.00	0.00	0.00	0.00	19.40	0.00	24.27	23.81	0.00
Clay 016	0.00	0.00	0.00	13.56	13.06	0.00	27.90	0.00	0.00

\*Critical element  
<sup>1</sup>Empirical calibration of XRF result using LA-ICP-MS data

Elemental XRF Values							
Sample	Co*	Fe	Mn*	Cr*	V*	Ti*	Ca <sup>1</sup>
Upper crust	17.30	39176.47	774.46	92.00	97.00	3836.85	25657.77
NIST-698	45.00	152352.96	2942.94	547.36	358.51	14268.29	4431.15
Clay 001	0.00	24845.50	0.00	0.00	0.00	9936.01	0.00
Clay 002	0.00	35789.14	0.00	0.00	0.00	11267.58	0.00
Clay 003	0.00	9767.20	0.00	0.00	0.00	6518.84	0.00
Clay 004	0.00	46579.40	0.00	0.00	0.00	9734.58	0.00
Clay 005	0.00	38524.06	0.00	0.00	0.00	10309.01	0.00
Clay 006	0.00	56182.74	0.00	0.00	0.00	12704.01	0.00
Clay 007	0.00	40277.37	0.00	0.00	0.00	11099.53	0.00
Clay 008	0.00	17865.28	0.00	0.00	0.00	12022.03	0.00
Clay 009	0.00	8945.86	0.00	0.00	0.00	12044.78	0.00
Clay 010	0.00	37393.70	0.00	0.00	0.00	10115.78	0.00
Clay 011	0.00	10923.56	0.00	0.00	0.00	13975.72	0.00
Clay 012	0.00	77427.28	0.00	0.00	0.00	35757.30	0.00
Clay 013	0.00	44124.10	0.00	0.00	0.00	23564.45	0.00
Clay 014	0.00	7995.94	0.00	0.00	0.00	13007.16	0.00
Clay 015	0.00	146523.40	0.00	0.00	0.00	57612.69	0.00
Clay 016	0.00	86875.81	0.00	0.00	0.00	36068.89	0.00

\*Critical element

<sup>1</sup>Empirical calibration of XRF result using LA-ICP-MS data

Elemental XRF Values							
Sample	K	Al*	P	Si <sup>1</sup>	Cl	S	Mg*
Upper crust	23244.12	81504.65	654.63	311407.86	370.00	621.00	14955.29
NIST-698	83.01	255098.98	1614.76	3225.33	0.00	572.66	349.76
Clay 001	295.84	119519.89	4543.83	178835.06	0.00	882.55	2395.99
Clay 002	0.00	126896.27	666.89	139148.64	0.00	164.63	2874.59
Clay 003	463.55	97702.00	745.30	166077.23	0.00	707.24	3107.00
Clay 004	2045.56	113915.88	4864.98	169572.22	0.00	708.67	4161.32
Clay 005	925.58	132004.71	2321.72	140655.67	0.00	708.85	2993.06
Clay 006	255.20	154482.47	666.71	148457.77	0.00	236.54	5079.60
Clay 007	0.00	147797.92	638.39	147804.93	0.00	60.66	3942.32
Clay 008	224.13	133605.71	1660.61	180146.53	0.00	71.44	4474.51
Clay 009	372.82	121195.88	1571.78	181810.66	0.00	0.00	5055.33
Clay 010	0.00	140350.37	1165.68	150888.43	0.00	64.05	4589.97
Clay 011	0.00	131294.10	692.78	174276.94	0.00	1412.20	2835.44
Clay 012	83.84	159440.16	0.00	148195.74	0.00	356.08	4338.57
Clay 013	289.27	149033.54	0.00	147886.35	0.00	614.47	1991.53
Clay 014	317.33	139797.47	0.00	122587.16	0.00	920.63	1867.74
Clay 015	377.10	168189.08	0.00	152703.84	0.00	188.78	4322.23
Clay 016	665.02	131767.45	228.07	150754.56	0.00	366.99	2161.61

\*Critical element

<sup>1</sup>Empirical calibration of XRF result using LA-ICP-MS data

Elemental XRF Values									
Sample	Nd*	Pr*	Ce*	La*	Ba*	Sb*	Sn*	Cd	Ag
Upper crust	27.00	7.10	63.00	31.00	624.00	0.40	2.10	0.09	53.00
NIST-698	138.32	34.91	300.00	218.16	71.65	0.00	0.00	9.45	0.00
SP2001	0.00	0.00	327.54	0.00	13.92	0.00	5.71	0.00	0.00
SP2002	0.00	0.00	178.34	27.55	14.67	0.00	0.00	0.00	0.00
SP2003	0.00	0.00	191.37	0.00	0.00	0.00	0.00	2.56	0.00
SP2004	337.54	199.94	517.78	168.77	108.73	0.00	0.00	0.00	0.00
SP2005	0.00	0.00	346.24	222.83	0.00	0.00	0.00	0.00	0.00
SP2006	0.00	0.00	195.98	16.65	0.00	0.00	10.70	5.05	1.64
SP2007	71.05	18.04	247.05	53.97	56.96	0.00	0.00	0.00	0.00
SP2029	577.05	343.18	699.78	267.92	176.36	0.00	0.00	0.00	0.00
SP2008	0.00	0.00	125.47	0.00	0.00	0.00	4.10	0.00	0.00
SP2009	0.00	0.00	142.25	0.00	0.00	0.00	18.56	2.31	0.00
SP2010	0.00	0.00	209.03	0.00	0.00	0.00	0.00	0.00	0.00
SP2011	0.00	0.00	191.48	0.00	0.00	0.00	4.60	0.00	0.00
SP2012	338.47	231.51	429.86	152.62	119.43	0.00	0.00	0.00	0.00
SP2013	0.00	0.00	208.45	0.00	0.00	0.00	4.16	0.00	2.35
SP2014	31.55	0.00	344.46	74.00	43.13	0.00	0.00	0.00	0.00
SP2015	508.79	313.92	414.62	229.75	153.62	0.00	0.00	0.00	2.64
SP2016	0.00	0.00	306.84	0.00	49.23	0.00	0.00	0.00	0.00
SP2017	0.00	0.00	59.59	0.00	0.00	0.00	9.03	0.00	0.00
SP2018	0.00	0.00	110.24	17.13	12.94	0.00	4.60	2.60	0.00
SP2019	0.00	0.00	247.99	0.00	0.00	0.00	0.00	0.00	0.00
SP2020	0.00	0.00	235.32	0.00	0.00	0.00	0.00	0.00	0.00
SP2021	296.61	192.48	567.30	181.09	110.60	0.00	0.00	0.00	0.00
SP2022	0.00	0.00	263.49	0.00	0.00	0.00	0.00	0.00	0.00
SP2023	32.95	0.00	326.73	58.00	53.37	0.00	0.00	0.00	2.21
SP2024	193.32	109.09	459.44	134.65	80.42	0.00	0.00	0.00	0.00
SP2025	0.00	0.00	582.38	0.00	13.60	0.00	5.88	0.00	0.00
SP2026	0.00	0.00	68.58	0.00	0.00	0.00	4.34	0.00	1.67
SP2027	0.00	0.00	124.41	67.88	31.55	0.00	4.22	2.37	0.00
SP2028	0.00	0.00	118.96	0.00	0.00	0.00	0.00	2.32	0.00

\*Critical element  
<sup>1</sup>Empirical calibration of XRF result using LA-ICP-MS data

Elemental XRF Values								
Sample	Mo <sup>1</sup>	Nb* <sup>1</sup>	Th	Zr* <sup>1</sup>	Y*	Sr <sup>1</sup>	U	Rb* <sup>1</sup>
Upper crust	1.10	12.00	10.50	193.00	21.00	320.00	2.70	84.00
NIST-698	7.17	49.90	26.78	451.59	263.06	127.23	7.72	0.42
SP2001	23.62	529.66	61.06	1512.95	5.38	77.14	4.23	0.00
SP2002	28.64	558.55	97.69	1607.70	8.07	146.07	13.04	0.09
SP2003	33.34	547.32	107.50	1599.13	6.60	99.95	9.63	0.00
SP2004	68.24	585.02	58.10	1680.55	5.77	106.35	8.07	0.00
SP2005	45.29	306.42	87.19	749.33	2.41	232.26	12.83	0.00
SP2006	0.00	578.84	66.02	1701.00	7.40	216.46	10.79	0.00
SP2007	0.00	528.02	63.59	1470.60	5.70	168.16	1.40	0.00
SP2029	35.98	459.43	18.61	1332.78	3.72	64.05	0.00	0.00
SP2008	34.79	694.50	133.72	2009.20	7.97	87.19	10.88	0.14
SP2009	58.13	578.79	129.37	1682.33	6.18	49.25	11.29	0.02
SP2010	21.49	530.83	101.00	1473.80	5.28	84.06	3.91	0.00
SP2011	0.63	514.85	113.84	1513.51	5.72	84.75	2.95	0.00
SP2012	0.00	428.05	42.31	1209.64	3.76	64.15	0.00	0.00
SP2013	37.28	504.86	115.59	1450.18	5.24	84.11	9.76	0.00
SP2014	0.00	554.85	38.37	1578.40	5.71	90.87	2.93	0.00
SP2015	12.24	526.63	53.78	1448.05	4.52	90.34	0.00	0.00
SP2016	9.51	566.59	58.62	1635.21	7.37	111.43	9.89	0.00
SP2017	67.49	702.56	130.19	1974.66	12.62	53.23	11.19	0.00
SP2018	39.83	647.57	97.25	1836.62	10.07	180.13	11.93	0.13
SP2019	67.11	545.92	88.28	1601.19	5.48	101.10	5.92	0.00
SP2020	52.04	541.21	65.41	1521.09	5.86	125.64	9.19	0.00
SP2021	2.81	476.42	18.61	1294.27	5.45	129.83	2.87	0.00
SP2022	29.63	442.07	28.51	1255.62	4.60	166.94	3.97	0.00
SP2023	40.08	498.48	71.10	1367.47	4.96	124.30	3.06	0.26
SP2024	15.58	507.75	26.65	1447.46	5.69	141.99	3.73	0.00
SP2025	64.97	829.25	148.84	2548.12	10.26	175.55	24.71	0.00
SP2026	79.64	506.75	104.94	1416.46	6.87	118.53	11.67	0.09
SP2027	28.38	699.59	112.66	1913.92	10.86	118.13	19.10	0.42
SP2028	34.11	580.24	114.01	1581.84	8.95	193.82	14.40	0.27

\*Critical element  
<sup>1</sup>Empirical calibration of XRF result using LA-ICP-MS data

Elemental XRF Values									
Sample	Bi*	Au	Se	As*	Pb	W*	Zn*	Cu	Ni*
Upper crust	0.16	1.50	0.09	4.80	17.00	1.90	67.00	28.00	47.00
NIST-698	0.00	0.00	0.00	36.38	46.58	0.00	232.99	46.26	225.42
SP2001	0.00	0.00	0.00	11.19	24.28	0.00	43.88	0.00	0.00
SP2002	0.00	0.00	0.00	19.78	44.83	0.00	127.58	0.00	0.00
SP2003	0.00	0.00	0.00	53.83	35.80	0.00	67.02	0.00	0.00
SP2004	0.00	0.00	0.00	21.34	30.54	0.00	126.94	24.32	0.00
SP2005	0.00	0.00	0.00	365.12	80.81	0.00	148.22	0.00	0.00
SP2006	0.00	0.00	0.00	18.33	30.36	0.00	4.87	0.00	0.00
SP2007	0.00	0.00	0.00	10.56	18.86	0.00	49.06	13.43	0.00
SP2029	0.00	0.00	0.00	12.36	8.21	0.00	37.76	10.51	0.00
SP2008	0.00	0.00	0.00	28.62	44.05	0.00	64.06	0.00	0.00
SP2009	0.00	0.00	0.00	96.75	35.16	0.00	75.40	0.00	0.00
SP2010	0.00	0.00	0.00	19.66	29.66	0.00	76.55	11.17	0.00
SP2011	0.00	0.00	0.00	10.65	16.01	0.00	45.08	0.00	0.00
SP2012	0.00	0.00	0.00	13.96	0.00	0.00	42.21	30.63	0.00
SP2013	0.00	0.00	0.00	7.30	38.74	0.00	67.52	9.75	0.00
SP2014	0.00	0.00	0.00	19.09	12.43	0.00	27.88	0.00	0.00
SP2015	0.00	0.00	0.00	24.39	7.08	0.00	46.07	56.20	0.00
SP2016	0.00	0.00	0.00	12.96	14.77	0.00	26.29	19.53	0.00
SP2017	0.00	0.00	0.00	34.94	21.40	0.00	14.63	22.70	0.00
SP2018	0.00	0.00	0.00	19.93	34.21	0.00	144.75	9.31	0.00
SP2019	0.00	0.00	0.00	16.80	31.01	0.00	59.65	0.00	0.00
SP2020	0.00	0.00	0.00	15.32	38.19	0.00	115.39	0.00	0.00
SP2021	0.00	0.00	0.00	6.06	9.24	0.00	34.26	15.10	0.00
SP2022	0.00	0.00	0.00	3.99	10.40	0.00	23.97	0.00	0.00
SP2023	0.00	0.00	0.00	11.01	36.09	0.00	125.28	20.99	0.00
SP2024	0.00	0.00	0.00	23.38	11.55	0.00	36.26	12.82	0.00
SP2025	0.00	0.00	0.00	72.30	54.42	20.75	50.42	56.17	0.00
SP2026	0.00	0.00	0.00	15.89	32.46	0.00	72.71	0.00	0.00
SP2027	0.00	0.00	0.00	34.75	49.68	0.00	232.04	28.16	0.00
SP2028	0.00	0.00	0.00	17.59	31.41	0.00	115.48	0.00	0.00

\*Critical element  
¹Empirical calibration of XRF result using LA-ICP-MS data

Elemental XRF Values							
Sample	Co*	Fe	Mn*	Cr*	V*	Ti*	Ca <sup>1</sup>
Upper crust	17.30	39176.47	774.46	92.00	97.00	3836.85	25657.77
NIST-698	45.00	152352.96	2942.94	547.36	358.51	14268.29	4431.15
SP2001	0.00	36036.27	0.00	0.00	0.00	10915.83	0.00
SP2002	0.00	24970.23	0.00	0.00	0.00	11808.61	0.00
SP2003	0.00	8851.12	0.00	0.00	0.00	10147.05	0.00
SP2004	0.00	88632.29	0.00	0.00	0.00	11959.50	0.00
SP2005	0.00	14550.19	0.00	0.00	0.00	9351.11	0.00
SP2006	0.00	9720.35	0.00	0.00	0.00	12936.00	0.00
SP2007	0.00	36851.43	0.00	0.00	0.00	9770.01	0.00
SP2029	0.00	173034.32	1227.09	0.00	0.00	9284.30	0.00
SP2008	0.00	8803.97	0.00	0.00	0.00	13132.60	0.00
SP2009	0.00	9854.78	0.00	0.00	0.00	11323.16	0.00
SP2010	0.00	32985.05	0.00	0.00	0.00	9797.45	0.00
SP2011	0.00	13123.70	0.00	0.00	0.00	9271.88	0.00
SP2012	0.00	121374.67	0.00	0.00	0.00	7917.56	0.00
SP2013	0.00	6911.19	0.00	0.00	0.00	9128.33	0.00
SP2014	0.00	34151.25	0.00	0.00	0.00	10111.62	0.00
SP2015	0.00	177611.29	7664.85	0.00	0.00	11582.41	193.73
SP2016	0.00	51509.62	0.00	0.00	0.00	13040.13	0.00
SP2017	0.00	9659.51	0.00	0.00	0.00	16137.18	0.00
SP2018	0.00	9345.30	0.00	0.00	0.00	13087.49	0.00
SP2019	0.00	41970.35	0.00	0.00	0.00	12029.97	0.00
SP2020	0.00	24253.42	0.00	0.00	0.00	11864.15	0.00
SP2021	0.00	93733.77	0.00	0.00	0.00	10017.68	0.00
SP2022	0.00	28496.81	0.00	0.00	0.00	9440.33	0.00
SP2023	0.00	67588.03	0.00	0.00	0.00	10335.87	0.00
SP2024	0.00	61503.10	0.00	0.00	0.00	10839.53	0.00
SP2025	0.00	23091.33	0.00	0.00	0.00	20012.67	0.00
SP2026	0.00	15014.34	0.00	0.00	0.00	10595.32	0.00
SP2027	0.00	8902.38	0.00	0.00	0.00	15440.01	0.00
SP2028	0.00	10402.71	0.00	0.00	0.00	11837.12	0.00

\*Critical element  
Empirical calibration of XRF result using LA-ICP-MS data

Elemental XRF Values							
Sample	K	Al*	P	Si <sup>1</sup>	Cl	S	Mg*
Upper crust	23244.12	81504.65	654.63	311407.86	370.00	621.00	14955.29
NIST-698	83.01	255098.98	1614.76	3225.33	0.00	572.66	349.76
SP2001	108.20	132454.99	0.00	83284.13	0.00	238.50	2494.21
SP2002	302.46	137470.93	0.00	114440.95	0.00	153.86	1903.31
SP2003	221.73	134375.14	0.00	113692.49	0.00	720.08	1931.95
SP2004	267.58	153809.11	0.00	122457.61	0.00	55.32	4003.70
SP2005	0.00	121409.24	5137.59	162379.58	0.00	1538.55	2592.18
SP2006	0.00	145523.31	0.00	110138.30	0.00	139.22	2154.92
SP2007	285.63	152360.09	0.00	122787.34	0.00	45.21	2357.59
SP2029	0.00	213281.65	1175.09	57390.18	0.00	1088.76	1080.66
SP2008	286.63	153365.62	0.00	105961.90	0.00	913.40	2336.02
SP2009	228.98	150795.98	0.00	101605.46	0.00	1868.18	2287.98
SP2010	239.45	157761.80	0.00	140297.47	0.00	72.45	3164.24
SP2011	172.69	148617.40	0.00	99265.55	0.00	205.95	2179.04
SP2012	0.00	186199.02	4379.13	105957.44	0.00	735.21	2194.33
SP2013	213.04	156316.24	0.00	110399.77	0.00	381.17	2184.59
SP2014	253.20	149009.80	0.00	125975.47	0.00	94.07	1651.32
SP2015	0.00	213994.07	0.00	71103.45	0.00	320.89	2873.83
SP2016	435.65	175571.93	0.00	105840.80	0.00	357.40	2350.40
SP2017	0.00	157090.42	0.00	56809.63	0.00	784.06	2376.15
SP2018	451.84	140730.34	0.00	140618.92	0.00	378.25	1369.47
SP2019	208.12	168469.56	0.00	122981.04	0.00	208.54	2908.44
SP2020	374.02	167786.31	0.00	121602.76	0.00	179.86	885.72
SP2021	262.52	179948.39	0.00	157010.18	0.00	60.39	1999.15
SP2022	168.82	136696.51	699.40	102654.38	0.00	393.68	1051.00
SP2023	373.83	177058.33	0.00	141927.26	0.00	55.17	3453.13
SP2024	223.79	156311.96	0.00	125684.02	0.00	162.97	1890.47
SP2025	0.00	168450.23	0.00	68101.21	0.00	742.12	2841.45
SP2026	223.21	143390.59	0.00	105279.04	0.00	236.94	1511.00
SP2027	458.73	141323.36	0.00	151192.02	0.00	397.30	2035.42
SP2028	263.05	152434.86	0.00	115819.86	0.00	374.49	1488.41

\*Critical element  
<sup>1</sup>Empirical calibration of XRF result using LA-ICP-MS data

Sample	Elemental XRF Values								
	Nd*	Pr*	Ce*	La*	Ba*	Sb*	Sn*	Cd	Ag
Upper crust	27.00	7.10	63.00	31.00	624.00	0.40	2.10	0.09	53.00
NIST-698	138.32	34.91	300.00	218.16	71.65	0.00	0.00	9.45	0.00
SP3001	222.51	128.07	523.79	129.61	98.29	0.00	0.00	0.00	0.00
SP3002	511.95	305.57	347.12	226.20	261.07	0.00	0.00	0.00	0.00
SP3003	0.00	0.00	44.83	0.00	0.00	0.00	5.94	0.00	0.00
SP3004	284.30	186.61	593.76	218.63	135.03	0.00	0.00	0.00	0.00
SP3005	0.00	0.00	118.86	18.41	14.63	0.00	6.34	2.59	0.00
SP3006	0.00	0.00	161.82	0.00	0.00	0.00	10.19	0.00	0.00
SP3007	0.00	0.00	122.33	0.00	0.00	0.00	4.56	0.00	0.00
SP3008	266.06	141.42	374.01	136.40	84.12	0.00	0.00	0.00	0.00
SP3009	194.24	113.56	438.74	109.37	168.57	0.00	0.00	0.00	0.00
SP3010	442.03	289.66	514.42	226.11	129.52	0.00	0.00	0.00	0.00
SP3011	0.00	0.00	215.28	0.00	0.00	0.00	5.15	0.00	0.00
SP3012	0.00	0.00	113.34	0.00	0.00	0.00	4.53	2.63	0.00
SP3013	0.00	0.00	339.86	18.95	36.25	0.00	5.02	0.00	0.00
SP3014	0.00	0.00	131.19	0.00	0.00	0.00	0.00	5.03	0.00
SP3015	321.66	178.87	468.43	141.05	105.00	0.00	0.00	0.00	0.00
SP3016	0.00	0.00	134.02	0.00	0.00	0.00	0.00	2.24	2.29
SP3017	0.00	0.00	209.80	20.71	31.64	0.00	0.00	0.00	0.00
SP3018	0.00	0.00	193.16	0.00	0.00	0.00	0.00	0.00	0.00
SP3019	0.00	0.00	326.21	0.00	0.00	0.00	0.00	0.00	0.00
SP3020	0.00	0.00	115.50	0.00	0.00	0.00	5.40	0.00	1.67
SP3021	142.45	23.48	406.39	94.73	69.06	0.00	0.00	0.00	0.00
SP3022	0.00	0.00	254.53	0.00	0.00	0.00	0.00	0.00	0.00
SP3023	359.27	235.07	495.51	194.81	118.48	0.00	0.00	0.00	0.00
SP3024	227.11	137.98	470.16	142.69	104.76	0.00	0.00	0.00	0.00
SP3025	0.00	0.00	212.42	0.00	0.00	0.00	5.56	0.00	0.00
SP3026	0.00	0.00	280.02	0.00	0.00	0.00	0.00	0.00	0.00
SP3027	71.10	0.00	323.30	50.35	32.37	0.00	0.00	0.00	0.00
SP3028	222.09	125.47	333.37	138.93	109.64	0.00	0.00	0.00	0.00
SP3029	70.40	23.89	291.62	75.63	59.64	0.00	0.00	0.00	0.00
SP3030	118.12	24.44	206.02	70.81	187.61	0.00	0.00	0.00	0.00
SP3031	0.00	0.00	161.37	39.44	72.03	0.00	5.07	0.00	0.00
SP3032	30.40	23.50	322.19	91.68	25.64	0.00	5.04	0.00	0.00
SP3033	0.00	0.00	330.96	0.00	0.00	0.00	0.00	0.00	0.00
SP3034	0.00	0.00	118.69	0.00	0.00	0.00	5.23	2.43	0.00
SP3035	0.00	0.00	335.22	0.00	28.72	0.00	0.00	0.00	0.00
SP3036	0.00	0.00	294.25	0.00	16.41	0.00	0.00	0.00	0.00

\*Critical element  
¹Empirical calibration of XRF result using LA-ICP-MS data

Elemental XRF Values								
Sample	Mo <sup>1</sup>	Nb* <sup>1</sup>	Th	Zr* <sup>1</sup>	Y*	Sr <sup>1</sup>	U	Rb* <sup>1</sup>
Upper crust	1.10	12.00	10.50	193.00	21.00	320.00	2.70	84.00
NIST-698	7.17	49.90	26.78	451.59	263.06	127.23	7.72	0.42
SP3001	0.00	624.16	30.25	1712.55	6.35	121.21	3.10	0.00
SP3002	1.13	447.45	40.10	1326.11	4.81	1461.21	0.00	0.00
SP3003	3.32	731.34	130.48	2066.86	8.12	106.84	12.90	0.00
SP3004	3.66	547.09	43.90	1524.55	6.13	223.46	0.00	0.00
SP3005	0.00	647.71	114.43	1883.45	8.77	142.31	15.31	0.04
SP3006	0.00	613.11	80.36	1741.00	6.73	113.33	3.51	0.00
SP3007	17.43	657.39	118.83	1902.34	7.46	116.62	12.63	0.00
SP3008	0.00	500.05	25.83	1430.95	4.73	83.65	0.00	0.00
SP3009	6.00	580.19	61.20	1663.46	5.82	1809.21	12.48	0.00
SP3010	47.12	506.75	22.00	1499.57	5.18	59.11	0.00	0.00
SP3011	45.79	572.50	95.63	1604.01	5.76	85.29	6.81	0.00
SP3012	30.15	631.71	123.42	1769.65	7.02	93.53	10.72	0.00
SP3013	20.13	531.23	108.46	1523.46	6.49	369.90	16.75	0.00
SP3014	147.62	620.69	125.56	1795.72	7.41	163.46	9.10	0.00
SP3015	7.92	551.43	55.27	1697.94	4.15	26.60	3.07	0.00
SP3016	5.62	562.18	110.41	1571.29	6.85	126.71	12.62	0.00
SP3017	32.34	855.85	141.15	2563.74	10.35	140.25	16.24	0.00
SP3018	0.05	580.16	116.92	1682.08	6.96	190.23	14.17	0.00
SP3019	0.00	530.93	61.88	1462.78	5.29	82.86	2.75	0.00
SP3020	9.11	644.44	125.98	1787.93	7.53	97.66	11.30	0.00
SP3021	49.51	666.62	115.24	2028.69	7.47	99.91	11.15	0.05
SP3022	27.42	578.39	132.05	1590.11	5.84	101.16	7.02	0.11
SP3023	18.17	587.62	29.53	1697.65	5.41	86.09	0.00	0.00
SP3024	24.65	599.61	96.35	1716.60	5.60	84.00	8.26	0.00
SP3025	5.50	651.61	163.55	1849.05	7.38	134.73	12.44	0.08
SP3026	22.08	544.63	111.17	1574.34	5.54	114.75	9.25	0.00
SP3027	41.27	531.94	73.82	1617.55	5.51	113.92	0.00	0.00
SP3028	106.99	718.85	39.32	2148.20	8.09	245.72	4.45	0.00
SP3029	41.35	741.99	69.91	2226.98	8.70	153.99	7.59	0.00
SP3030	22.83	595.65	98.52	1788.98	7.47	1199.47	36.34	0.00
SP3031	10.49	586.63	83.98	1733.54	6.82	403.24	10.33	0.00
SP3032	51.47	597.55	69.58	1784.49	6.73	106.93	5.70	0.00
SP3033	32.46	548.07	109.40	1531.91	5.21	97.21	6.26	0.00
SP3034	37.75	690.71	39.12	1938.62	7.91	89.56	3.33	0.00
SP3035	45.84	657.13	107.98	1803.60	6.76	114.65	12.44	0.14
SP3036	76.32	629.21	78.35	1854.50	7.06	98.82	7.97	0.00

\*Critical element

<sup>1</sup>Empirical calibration of XRF result using LA-ICP-MS data

Elemental XRF Values									
Sample	Bi*	Au	Se	As*	Pb	W*	Zn*	Cu	Ni*
Upper crust	0.16	1.50	0.09	4.80	17.00	1.90	67.00	28.00	47.00
NIST-698	0.00	0.00	0.00	36.38	46.58	0.00	232.99	46.26	225.42
SP3001	0.00	0.00	0.00	8.91	7.76	0.00	15.00	12.20	0.00
SP3002	0.00	0.00	0.00	44.29	10.57	0.00	6.36	27.18	0.00
SP3003	0.00	0.00	0.00	59.49	45.98	0.00	49.76	24.71	0.00
SP3004	0.00	0.00	0.00	23.53	15.15	0.00	43.54	0.00	0.00
SP3005	0.00	0.00	0.00	47.68	47.30	0.00	77.36	11.83	0.00
SP3006	0.00	0.00	0.00	15.20	24.05	0.00	58.10	0.00	0.00
SP3007	0.00	0.00	0.00	41.80	37.91	0.00	56.92	22.35	0.00
SP3008	0.00	0.00	0.00	21.94	7.97	0.00	27.01	0.00	0.00
SP3009	0.00	0.00	0.00	45.47	15.94	0.00	22.42	15.28	0.00
SP3010	0.00	0.00	0.00	10.00	5.55	0.00	23.20	0.00	0.00
SP3011	0.00	0.00	0.00	9.55	37.16	0.00	65.62	11.01	0.00
SP3012	0.00	0.00	0.00	14.78	34.70	0.00	54.74	8.91	0.00
SP3013	0.00	0.00	0.00	29.22	46.67	0.00	76.20	0.00	0.00
SP3014	0.00	0.00	0.00	31.88	24.14	0.00	54.13	0.00	0.00
SP3015	0.00	0.00	0.00	343.49	21.62	0.00	16.74	12.00	0.00
SP3016	0.00	0.00	0.00	18.21	20.79	0.00	26.09	0.00	0.00
SP3017	0.00	0.00	0.00	44.33	45.88	0.00	47.23	45.19	0.00
SP3018	0.00	0.00	0.00	21.36	37.61	0.00	59.50	8.23	0.00
SP3019	0.00	0.00	0.00	12.30	19.82	0.00	41.35	9.37	0.00
SP3020	0.00	0.00	0.00	11.10	37.05	0.00	66.04	0.00	0.00
SP3021	0.00	0.00	0.00	27.29	45.03	0.00	91.77	23.69	0.00
SP3022	0.00	0.00	0.00	18.08	29.78	0.00	65.14	19.37	0.00
SP3023	0.00	0.00	0.00	11.89	10.21	0.00	22.21	0.00	0.00
SP3024	0.00	0.00	0.00	65.24	34.98	0.00	83.13	23.45	0.00
SP3025	0.00	0.00	0.00	18.00	39.01	0.00	62.08	7.84	0.00
SP3026	0.00	0.00	0.00	8.65	32.13	0.00	70.99	0.00	0.00
SP3027	0.00	0.00	0.00	17.75	27.13	0.00	108.87	22.23	0.00
SP3028	0.00	0.00	0.00	134.91	16.90	0.00	10.72	9.99	0.00
SP3029	0.00	0.00	0.00	11.92	38.40	0.00	51.33	30.70	0.00
SP3030	0.00	0.00	0.00	25.79	24.31	0.00	28.31	32.55	0.00
SP3031	0.00	0.00	0.00	21.16	18.34	0.00	12.96	9.21	0.00
SP3032	0.00	0.00	0.00	17.48	24.99	0.00	62.36	12.85	0.00
SP3033	0.00	0.00	0.00	14.79	30.59	0.00	69.09	8.88	0.00
SP3034	0.00	0.00	0.00	19.47	12.61	0.00	109.44	0.00	0.00
SP3035	0.00	0.00	0.00	26.88	48.64	0.00	66.77	19.58	0.00
SP3036	0.00	0.00	0.00	20.55	26.85	0.00	49.15	27.43	0.00

\*Critical element

<sup>1</sup>Empirical calibration of XRF result using LA-ICP-MS data

Elemental XRF Values							
Sample	Co*	Fe	Mn*	Cr*	V*	Ti*	Ca <sup>1</sup>
Upper crust	17.30	39176.47	774.46	92.00	97.00	3836.85	25657.77
NIST-698	45.00	152352.96	2942.94	547.36	358.51	14268.29	4431.15
SP3001	0.00	76652.89	0.00	0.00	0.00	13481.62	0.00
SP3002	0.00	137120.00	0.00	0.00	0.00	10273.77	595.38
SP3003	0.00	12009.04	0.00	0.00	0.00	15670.36	0.00
SP3004	0.00	109620.89	0.00	0.00	0.00	11429.16	0.00
SP3005	0.00	27156.20	0.00	0.00	0.00	13350.66	0.00
SP3006	0.00	10003.24	0.00	0.00	0.00	12071.06	0.00
SP3007	0.00	21470.86	0.00	0.00	0.00	13183.73	0.00
SP3008	0.00	99951.54	0.00	0.00	0.00	9281.65	0.00
SP3009	0.00	87680.09	0.00	0.00	0.00	12355.36	192.57
SP3010	0.00	136521.93	0.00	0.00	0.00	11703.43	0.00
SP3011	0.00	25077.94	0.00	0.00	0.00	11970.73	0.00
SP3012	0.00	7521.20	0.00	0.00	0.00	13206.01	0.00
SP3013	0.00	23414.77	0.00	0.00	0.00	10429.83	0.00
SP3014	0.00	7957.49	0.00	0.00	0.00	12044.74	0.00
SP3015	0.00	123475.92	0.00	0.00	0.00	11848.11	0.00
SP3016	0.00	20832.60	0.00	0.00	0.00	11986.77	0.00
SP3017	0.00	25557.48	0.00	0.00	0.00	18377.99	0.00
SP3018	0.00	7352.57	0.00	0.00	0.00	11221.55	0.00
SP3019	0.00	37831.85	0.00	0.00	0.00	10826.35	0.00
SP3020	0.00	11419.89	0.00	0.00	0.00	12850.13	0.00
SP3021	0.00	41453.36	0.00	0.00	0.00	11728.95	0.00
SP3022	0.00	34778.34	0.00	0.00	0.00	11665.68	0.00
SP3023	0.00	109787.71	0.00	0.00	0.00	10671.16	0.00
SP3024	0.00	68643.40	0.00	0.00	0.00	12084.15	0.00
SP3025	0.00	8843.44	0.00	0.00	0.00	13150.37	0.00
SP3026	0.00	45599.31	0.00	0.00	0.00	11066.74	0.00
SP3027	0.00	65287.35	0.00	0.00	0.00	10736.68	0.00
SP3028	0.00	47662.43	0.00	0.00	0.00	16288.62	0.00
SP3029	0.00	35445.48	0.00	0.00	0.00	15605.84	0.00
SP3030	0.00	54687.70	0.00	0.00	0.00	14470.78	102.54
SP3031	0.00	40148.17	0.00	0.00	0.00	13997.02	0.00
SP3032	0.00	49897.72	0.00	0.00	0.00	12835.26	0.00
SP3033	0.00	53428.28	0.00	0.00	0.00	11713.78	0.00
SP3034	0.00	11284.50	0.00	0.00	0.00	14375.66	0.00
SP3035	0.00	38288.75	0.00	0.00	0.00	14564.66	0.00
SP3036	0.00	36456.19	0.00	0.00	0.00	13581.63	0.00

\*Critical element

<sup>1</sup>Empirical calibration of XRF result using LA-ICP-MS data

Elemental XRF Values							
Sample	K	Al*	P	Si <sup>1</sup>	Cl	S	Mg*
Upper crust	23244.12	81504.65	654.63	311407.86	370.00	621.00	14955.29
NIST-698	83.01	255098.98	1614.76	3225.33	0.00	572.66	349.76
SP3001	0.00	184240.93	0.00	70792.85	0.00	359.60	2362.21
SP3002	0.00	174466.63	7832.10	22861.60	0.00	2074.12	3550.97
SP3003	221.57	147943.51	0.00	86359.70	0.00	598.95	2150.01
SP3004	0.00	187063.38	0.00	96290.70	0.00	273.96	2844.77
SP3005	291.56	158172.35	0.00	84387.27	0.00	772.93	2891.69
SP3006	253.44	117611.56	0.00	85089.53	0.00	129.90	1092.93
SP3007	269.07	163952.41	0.00	102349.05	0.00	750.25	1657.03
SP3008	0.00	200208.67	0.00	105681.79	0.00	2585.84	2944.74
SP3009	0.00	190723.10	4117.23	63286.02	0.00	515.55	2525.64
SP3010	0.00	215704.87	0.00	84075.79	0.00	221.73	3961.69
SP3011	243.22	155103.04	0.00	103706.43	0.00	387.82	2261.01
SP3012	192.34	140247.07	0.00	97623.26	0.00	303.26	1571.94
SP3013	189.86	147681.56	945.33	107721.06	0.00	109.49	1927.21
SP3014	241.75	148194.73	0.00	92911.42	0.00	1084.14	1896.02
SP3015	0.00	179591.85	0.00	41133.90	0.00	2350.71	3073.84
SP3016	0.00	158335.39	0.00	44727.12	0.00	481.49	1297.84
SP3017	66.17	173359.51	0.00	59660.75	0.00	492.13	2254.83
SP3018	214.24	147795.26	0.00	110456.11	0.00	205.77	1819.69
SP3019	185.62	171118.62	0.00	127997.62	0.00	139.73	3216.68
SP3020	257.77	152239.21	0.00	102594.05	0.00	447.50	1999.40
SP3021	330.51	148304.30	0.00	109393.55	0.00	161.77	2418.79
SP3022	209.96	178884.58	511.34	105541.11	0.00	176.14	3847.28
SP3023	0.00	189936.51	313.50	82649.14	0.00	225.05	4547.34
SP3024	0.00	174302.73	0.00	108720.77	0.00	10208.82	3698.95
SP3025	301.89	158413.27	223.52	100479.58	0.00	261.23	3013.68
SP3026	53.99	181480.73	0.00	110885.46	0.00	228.92	2499.61
SP3027	127.59	183300.79	0.00	133734.08	0.00	132.97	2506.75
SP3028	0.00	185273.15	0.00	56857.37	0.00	2555.32	3546.72
SP3029	259.25	169439.79	238.97	123739.05	0.00	224.01	3232.14
SP3030	0.00	177223.97	2282.06	61677.19	0.00	453.23	3772.18
SP3031	0.00	173445.21	205.00	57867.36	0.00	824.55	3228.94
SP3032	229.16	165375.11	419.91	111826.02	0.00	179.36	4465.56
SP3033	66.37	182811.41	389.83	111907.23	0.00	217.55	2242.98
SP3034	327.86	156155.63	0.00	121298.74	0.00	190.89	1754.64
SP3035	169.64	178927.38	0.00	124748.90	0.00	317.34	3858.23
SP3036	208.83	168310.51	0.00	104708.69	0.00	223.35	2467.19

\*Critical element

<sup>1</sup>Empirical calibration of XRF result using LA-ICP-MS data

Elemental XRF Values									
Sample	Nd*	Pr*	Ce*	La*	Ba*	Sb*	Sn*	Cd	Ag
Upper crust	27.00	7.10	63.00	31.00	624.00	0.40	2.10	0.09	53.00
NIST-698	138.32	34.91	300.00	218.16	71.65	0.00	0.00	9.45	0.00
SP4001	0.00	0.00	84.08	0.00	0.00	0.00	4.71	0.00	0.00
SP4002	386.57	227.55	285.74	165.22	113.47	0.00	0.00	0.00	0.00
SP4003	0.00	0.00	181.91	0.00	0.00	0.00	15.40	2.27	0.00
SP4004	81.22	42.96	217.91	63.69	51.91	0.00	0.00	0.00	0.00
SP4005	0.00	0.00	258.92	18.91	63.01	0.00	0.00	0.00	0.00
SP4006	0.00	0.00	235.55	47.59	58.87	0.00	4.49	0.00	0.00
SP4007	0.00	0.00	184.68	0.00	0.00	0.00	4.54	0.00	0.00
SP4008	209.28	145.89	286.45	123.89	111.82	0.00	0.00	0.00	0.00
SP4009	0.00	0.00	80.51	0.00	0.00	0.00	0.00	0.00	0.00
SP4010	295.31	191.98	303.95	157.88	104.28	0.00	0.00	0.00	0.00
SP4011	0.00	0.00	375.30	91.90	116.15	0.00	4.42	0.00	0.00
SP4012	0.00	0.00	143.81	20.67	14.41	0.00	5.82	0.00	0.00
SP4013	249.32	124.32	298.52	131.58	109.75	0.00	0.00	0.00	0.00
SP4014	0.00	0.00	210.62	0.00	76.53	0.00	0.00	0.00	0.00
SP4015	0.00	0.00	275.18	74.59	97.61	0.00	0.00	0.00	0.00
SP4016	0.00	0.00	305.95	42.09	53.25	0.00	5.09	0.00	0.00
SP4017	0.00	0.00	297.92	80.42	88.80	0.00	0.00	0.00	0.00
SP4018	0.00	0.00	394.69	129.36	98.46	0.00	4.24	0.00	0.00
SP4019	33.82	0.00	229.66	95.97	105.75	0.00	0.00	0.00	0.00

\*Critical element  
<sup>1</sup>Empirical calibration of XRF result using LA-ICP-MS data

Elemental XRF Values								
Sample	Mo <sup>1</sup>	Nb* <sup>1</sup>	Th	Zr* <sup>1</sup>	Y*	Sr <sup>1</sup>	U	Rb* <sup>1</sup>
Upper crust	1.10	12.00	10.50	193.00	21.00	320.00	2.70	84.00
NIST-698	7.17	49.90	26.78	451.59	263.06	127.23	7.72	0.42
SP4001	8.60	736.85	134.43	2176.90	8.91	115.08	10.01	0.00
SP4002	55.32	493.79	65.21	1325.89	4.90	105.50	0.00	0.00
SP4003	16.82	686.37	138.60	2032.92	8.27	229.19	16.61	0.00
SP4004	1.45	695.84	39.34	1941.42	7.41	184.11	4.94	0.00
SP4005	11.11	583.53	133.07	1702.08	7.52	954.84	33.32	0.00
SP4006	0.00	629.28	100.41	1894.99	7.99	1036.38	30.78	0.00
SP4007	6.88	736.33	148.21	2199.30	8.92	246.27	16.32	0.00
SP4008	12.37	583.83	97.32	1843.97	6.39	512.99	6.09	0.00
SP4009	0.00	547.77	97.27	1572.15	5.47	74.70	11.10	0.00
SP4010	3.34	598.62	68.17	1609.27	5.65	111.50	2.53	0.00
SP4011	9.82	562.44	128.21	1675.38	7.49	1404.99	28.51	0.00
SP4012	3.75	605.20	71.10	1774.91	6.43	74.74	4.01	0.00
SP4013	15.68	584.11	111.95	1716.00	6.35	148.87	11.04	0.00
SP4014	9.86	646.03	135.52	1820.04	7.77	171.21	11.19	0.00
SP4015	34.30	594.23	125.32	1817.73	8.78	1350.20	51.29	0.00
SP4016	19.29	581.28	119.05	1771.92	7.14	479.49	41.71	0.00
SP4017	18.54	564.03	134.50	1682.70	7.09	476.44	24.81	0.00
SP4018	6.92	570.67	124.44	1705.95	7.79	1099.64	33.66	0.00
SP4019	0.24	530.24	29.38	1567.17	6.61	462.27	6.84	0.00

\*Critical element  
<sup>1</sup>Empirical calibration of XRF result using LA-ICP-MS data

Elemental XRF Values									
Sample	Bi*	Au	Se	As*	Pb	W*	Zn*	Cu	Ni*
Upper crust	0.16	1.50	0.09	4.80	17.00	1.90	67.00	28.00	47.00
NIST-698	0.00	0.00	0.00	36.38	46.58	0.00	232.99	46.26	225.42
SP4001	0.00	0.00	0.00	29.10	28.89	0.00	18.16	0.00	0.00
SP4002	0.00	0.00	0.00	45.31	5.05	0.00	30.61	24.97	0.00
SP4003	0.00	0.00	0.00	19.92	20.85	0.00	4.85	19.15	0.00
SP4004	0.00	0.00	0.00	11.55	6.29	0.00	0.00	0.00	0.00
SP4005	0.00	0.00	0.00	40.86	31.30	0.00	0.00	0.00	0.00
SP4006	0.00	0.00	0.00	14.14	20.77	0.00	0.00	8.23	0.00
SP4007	0.00	0.00	0.00	30.67	32.19	0.00	24.40	23.58	0.00
SP4008	0.00	0.00	0.00	38.55	19.85	0.00	19.55	41.88	0.00
SP4009	0.00	0.00	0.00	18.88	16.35	0.00	38.00	0.00	0.00
SP4010	0.00	0.00	0.00	24.93	10.51	0.00	14.49	13.59	0.00
SP4011	0.00	0.00	0.00	113.49	27.23	0.00	3.78	9.61	0.00
SP4012	0.00	0.00	0.00	14.29	20.21	0.00	15.11	13.04	0.00
SP4013	0.00	0.00	0.00	24.64	28.66	0.00	23.03	42.93	0.00
SP4014	0.00	0.00	0.00	13.29	33.18	0.00	20.65	24.17	0.00
SP4015	0.00	0.00	0.00	81.32	44.56	0.00	26.85	10.25	0.00
SP4016	0.00	0.00	0.00	32.49	59.76	0.00	0.00	22.31	0.00
SP4017	0.00	0.00	0.00	30.38	44.67	0.00	11.23	8.14	0.00
SP4018	0.00	0.00	0.00	23.36	23.84	0.00	0.00	11.36	0.00
SP4019	0.00	0.00	0.00	10.48	11.62	0.00	5.68	0.00	0.00

\*Critical element  
<sup>1</sup>Empirical calibration of XRF result using LA-ICP-MS data

Elemental XRF Values							
Sample	Co*	Fe	Mn*	Cr*	V*	Ti*	Ca <sup>1</sup>
Upper crust	17.30	39176.47	774.46	92.00	97.00	3836.85	25657.77
NIST-698	45.00	152352.96	2942.94	547.36	358.51	14268.29	4431.15
SP4001	0.00	10227.56	0.00	0.00	0.00	16282.53	0.00
SP4002	0.00	142744.08	2828.62	0.00	0.00	9837.07	0.00
SP4003	0.00	18939.87	0.00	0.00	0.00	15718.61	0.00
SP4004	0.00	64909.74	0.00	0.00	0.00	15548.53	0.00
SP4005	0.00	14237.50	0.00	0.00	0.00	13638.49	0.00
SP4006	0.00	16638.80	0.00	0.00	0.00	14639.30	129.07
SP4007	0.00	25176.55	0.00	0.00	0.00	16210.97	0.00
SP4008	0.00	90625.88	0.00	0.00	0.00	12273.52	534.93
SP4009	0.00	43754.19	0.00	0.00	0.00	10159.12	100.72
SP4010	0.00	102531.03	0.00	0.00	0.00	12692.19	44.45
SP4011	0.00	17886.86	0.00	0.00	0.00	14632.83	140.52
SP4012	0.00	75707.61	0.00	0.00	0.00	14439.85	101.69
SP4013	0.00	78113.79	0.00	0.00	0.00	14811.57	388.52
SP4014	0.00	39898.86	0.00	0.00	0.00	15824.58	96.22
SP4015	0.00	12726.62	0.00	0.00	0.00	15923.51	20.39
SP4016	0.00	23574.97	0.00	0.00	0.00	14733.76	68.37
SP4017	0.00	15153.85	0.00	0.00	0.00	14022.95	0.00
SP4018	0.00	11591.44	0.00	0.00	0.00	14549.37	107.10
SP4019	0.00	21864.23	0.00	0.00	0.00	12716.21	14.29

\*Critical element  
<sup>1</sup>Empirical calibration of XRF result using LA-ICP-MS data

Elemental XRF Values							
Sample	K	Al*	P	Si <sup>1</sup>	Cl	S	Mg*
Upper crust	23244.12	81504.65	654.63	311407.86	370.00	621.00	14955.29
NIST-698	83.01	255098.98	1614.76	3225.33	0.00	572.66	349.76
SP4001	0.00	154034.64	0.00	53011.96	0.00	821.32	2453.93
SP4002	0.00	186150.22	0.00	28693.66	0.00	557.78	2200.21
SP4003	0.00	159736.80	0.00	17291.32	0.00	514.38	995.57
SP4004	0.00	177817.56	0.00	28970.70	0.00	796.88	2789.54
SP4005	0.00	152237.82	1431.98	69082.13	0.00	1498.54	2261.77
SP4006	0.00	171286.97	755.96	24752.67	0.00	365.35	2190.11
SP4007	0.00	165539.97	0.00	49545.24	0.00	352.50	3284.87
SP4008	0.00	187924.23	0.00	29320.51	0.00	790.66	2005.60
SP4009	132.91	145042.01	0.00	62480.93	0.00	275.10	878.38
SP4010	0.00	196779.60	0.00	37299.93	0.00	1288.40	3487.34
SP4011	0.00	170114.70	3184.29	48582.05	0.00	710.97	3110.65
SP4012	0.00	208091.46	0.00	46326.77	0.00	421.90	3946.27
SP4013	0.00	210329.81	0.00	34816.82	0.00	389.85	4897.46
SP4014	0.00	190533.08	0.00	47396.55	0.00	370.47	4663.70
SP4015	0.00	168528.64	2405.74	28256.84	0.00	1144.70	3117.44
SP4016	0.00	174978.21	0.00	42936.92	0.00	342.52	2787.02
SP4017	0.00	183398.29	0.00	34714.65	0.00	527.42	3332.99
SP4018	0.00	167851.52	2586.24	37128.56	0.00	629.99	2936.69
SP4019	451.62	136046.82	437.63	125804.13	0.00	991.41	1422.65

\*Critical element  
<sup>1</sup>Empirical calibration of XRF result using LA-ICP-MS data

Appendix G. Compiled results from LA-ICP-MS analysis at TexasTech GeoAnalytical Laboratory for Section 20 bauxite samples Arkansas. NIST-698 samples and background concentrations of the Earth's upper continental crust (in red) at the top of each table for reference.

Sample	Results from LA-ICP-MS analysis					
	Na ppm	Mg* ppm	Si ppm	Ca ppm	Ti* ppm	Sc* ppm
NIST698	95.2	328.7	4007.5	4435.0	13633	46.7
Upper Crust	24258.7	14955.3	311407.9	25657.8	3836.9	14.0
SP1026	114.6	187.9	113156.3	1455.2	14245.9	8.2
SP1018	112.2	135.6	93545.2	1354.4	17611.7	8.0
SP1015	83.0	199.8	84103.0	1106.7	13976.7	6.6
SP1006	94.4	218.4	69241.7	1387.8	15956.6	6.9
Clay015	106.6	700.2	115298.2	1099.8	17290.3	7.0
Clay006	111.7	350.8	144366.4	1144.8	16341.7	7.4
SP2026	107.5	200.3	106907.1	1293.8	12371.4	5.6
SP2022	99.6	331.4	101052.5	1451.1	11012.3	5.2
SP2020	121.0	353.1	113063.4	1505.0	14992.5	6.4
SP2017	98.6	152.8	50282.5	1348.5	18682.8	9.1
SP2007	93.2	412.2	110526.6	1652.3	13350.7	5.8
SP2005	152.0	255.3	172641.6	1817.0	10253.6	5.0
SP3026	100.8	363.8	97559.5	1516.8	14842.3	6.0
SP3023	78.7	533.7	68148.0	1178.8	13604.0	7.0
SP3008	92.0	376.1	80137.0	1343.6	11852.2	5.9
SP3011	104.5	241.3	102276.2	1159.9	16245.2	6.0
SP4018	94.3	181.8	29012.6	3987.9	16661.8	11.1
SP4014	65.9	561.9	43509.1	2371.3	17132.5	9.0
SP4012	59.3	722.2	40672.3	2364.1	16194.6	8.9
SP4006	77.0	172.2	21192.3	4226.9	17706.7	11.3
<i>*Critical element</i>						

Sample	Results from LA-ICP-MS analysis							
	Zr*	V*	Cr*	Ni*	Ga*	Rb*	Sr	Y*
	ppm	ppm	ppm	ppm	ppm	ppm	ppm	ppm
NIST698	460.9	350.6	457.0	225.4	40.7	0.4	127.2	263.1
Upper Crust	193.0	97.0	92.0	47.0	17.5	84.0	320.0	21.0
SP1026	1685.4	188.7	43.0	19.7	58.8	1.7	225.4	42.0
SP1018	2014.7	190.4	40.4	14.1	56.3	2.0	179.5	46.0
SP1015	1796.4	170.8	31.3	13.0	53.6	2.6	133.2	43.0
SP1006	2035.7	162.4	37.6	11.8	61.6	2.1	101.2	43.0
Clay015	2275.5	176.0	38.6	11.5	39.1	3.4	108.2	55.0
Clay006	1998.2	177.5	45.7	11.8	46.1	2.4	94.5	47.0
SP2026	1603.8	151.0	40.1	18.2	48.6	3.9	121.6	46.0
SP2022	1425.2	144.5	25.9	13.8	55.2	3.4	164.9	31.0
SP2020	1629.4	158.3	36.6	23.8	57.9	4.4	127.3	37.0
SP2017	2296.0	197.5	42.9	9.2	59.8	1.7	61.4	85.0
SP2007	1566.6	141.8	37.4	16.1	47.6	3.2	166.9	37.0
SP2005	759.3	102.1	48.9	20.4	53.4	1.3	273.8	15.0
SP3026	1807.8	181.0	26.4	20.3	57.6	3.4	125.2	38.0
SP3023	1799.9	221.4	32.5	11.9	53.2	2.8	90.5	38.0
SP3008	1552.9	162.0	21.1	11.4	49.1	3.6	91.7	34.0
SP3011	1810.4	156.2	30.3	13.1	57.2	3.7	94.6	38.0
SP4018	1858.7	197.9	53.7	8.9	87.2	0.7	1115.2	45.0
SP4014	2021.9	205.8	42.1	8.3	60.8	2.0	181.2	49.0
SP4012	2017.1	219.8	40.3	10.5	54.8	1.9	85.5	47.0
SP4006	2314.3	215.8	58.8	6.6	82.2	0.9	1099.7	54.0
<i>*Critical element</i>								

Sample	Results from LA-ICP-MS analysis							
	Nb*	Mo	Ba*	La*	Ce*	Pr*	Nd*	Eu*
	ppm	ppm	ppm	ppm	ppm	ppm	ppm	ppm
NIST698	49.9	7.2	55.4	218.2	255.5	34.9	138.3	5.6
Upper Crust	8.0	12.0	624.0	31.0	63.0	7.1	27.0	1.0
SP1026	620.6	21.0	100.0	188.1	612.8	34.1	90.4	1.1
SP1018	752.0	30.0	68.7	47.0	252.3	8.4	24.3	0.5
SP1015	653.9	22.6	60.0	43.2	339.4	8.1	25.5	0.6
SP1006	763.5	21.4	51.3	29.3	527.2	6.2	20.2	0.6
Clay015	724.3	18.0	86.1	84.9	207.7	14.3	44.5	0.9
Clay006	677.7	33.6	68.0	77.8	226.3	13.4	41.2	0.8
SP2026	596.9	90.3	59.0	53.7	267.3	10.8	34.3	0.7
SP2022	513.2	40.6	52.7	36.4	571.7	7.2	22.8	0.5
SP2020	662.4	60.8	59.7	39.0	572.3	7.8	23.8	0.6
SP2017	926.0	74.8	52.9	34.5	221.2	7.7	24.9	0.9
SP2007	579.2	14.4	53.2	43.6	339.1	9.1	29.6	0.6
SP2005	316.4	62.7	74.3	636.0	922.9	57.0	110.9	1.2
SP3026	697.2	33.4	52.4	30.8	506.3	6.6	21.0	0.5
SP3023	671.8	46.0	47.7	37.1	460.4	7.4	24.0	0.6
SP3008	583.4	36.6	46.4	31.7	454.9	6.6	21.3	0.5
SP3011	690.9	55.4	52.2	33.6	493.6	7.0	21.8	0.5
SP4018	706.8	29.1	198.7	229.2	787.0	46.2	116.7	1.3
SP4014	766.5	25.2	160.1	46.4	467.8	10.6	36.1	0.9
SP4012	756.5	16.3	50.1	43.5	257.2	8.4	27.0	0.7
SP4006	808.1	28.9	142.0	126.2	565.1	20.9	56.5	1.1
<i>*Critical element</i>								

Sample	Results from LA-ICP-MS analysis							
	Gd*	Tb*	Dy*	Ho*	Er*	Sm*	Tm*	Yb*
	ppm	ppm	ppm	ppm	ppm	ppm	ppm	ppm
NIST698	28.4	3.8	24.9	5.3	14.8	24.5	1.8	10.6
Upper Crust	4.0	0.7	3.9	0.8	2.3	4.7	0.3	2.0
SP1026	7.0	0.9	6.6	1.5	5.7	9.7	0.9	6.8
SP1018	4.2	0.7	6.0	1.5	5.8	3.8	1.0	7.3
SP1015	4.6	0.8	6.0	1.5	5.5	4.4	0.9	6.7
SP1006	4.5	0.8	5.9	1.5	5.7	3.9	1.0	7.4
Clay015	6.3	1.0	7.6	1.8	6.7	6.7	1.2	8.9
Clay006	5.8	0.9	6.8	1.6	6.0	6.1	1.0	7.8
SP2026	5.4	0.9	7.0	1.6	5.7	5.2	0.9	6.5
SP2022	4.4	0.6	4.4	1.0	3.8	3.7	0.6	4.8
SP2020	4.6	0.7	5.2	1.3	4.6	4.0	0.8	6.0
SP2017	6.7	1.5	12.7	3.2	11.2	5.0	1.8	12.2
SP2007	5.2	0.7	5.4	1.2	4.6	4.9	0.8	5.8
SP2005	10.1	0.7	3.7	0.6	2.0	10.3	0.3	1.9
SP3026	4.7	0.7	5.3	1.3	4.8	3.9	0.8	6.3
SP3023	4.9	0.7	5.3	1.3	5.0	4.1	0.8	6.4
SP3008	4.3	0.7	5.0	1.2	4.6	3.7	0.7	5.6
SP3011	4.6	0.7	5.1	1.3	4.8	3.8	0.8	6.2
SP4018	9.4	1.1	7.0	1.6	5.6	11.5	0.9	6.8
SP4014	6.4	1.0	7.2	1.7	6.0	6.1	1.0	7.7
SP4012	5.0	0.9	6.9	1.7	6.0	4.9	1.0	7.3
SP4006	8.6	1.1	8.1	1.9	6.8	8.0	1.1	8.4

\*Critical element

Sample	Results from LA-ICP-MS analysis					
	Lu*	Hf*	Ta*	Pb	Th	U
	ppm	ppm	ppm	ppm	ppm	ppm
NIST698	1.5	12.1	3.4	46.6	26.8	7.7
Upper Crust	0.3	5.3	0.9	17.0	10.5	2.7
SP1026	1.0	36.0	50.0	19.9	55.6	11.5
SP1018	1.2	42.7	63.9	22.3	58.2	12.2
SP1015	1.0	38.0	54.5	25.0	56.8	8.4
SP1006	1.1	42.9	60.0	20.1	62.5	10.1
Clay015	1.4	45.2	61.6	34.5	48.8	7.3
Clay006	1.2	41.7	57.4	28.4	58.6	8.8
SP2026	1.0	33.9	46.4	21.6	51.1	9.3
SP2022	0.7	31.2	40.6	20.4	46.1	7.7
SP2020	0.9	35.3	51.8	26.7	52.8	9.6
SP2017	1.9	47.2	66.7	19.9	62.9	15.7
SP2007	0.9	34.1	47.8	21.2	54.3	6.5
SP2005	0.3	15.4	21.8	50.7	52.7	8.5
SP3026	1.0	38.2	56.3	25.6	58.7	9.1
SP3023	1.0	37.6	54.8	28.2	64.7	8.9
SP3008	0.9	34.3	49.4	26.4	52.9	7.9
SP3011	1.0	37.8	55.1	22.4	56.7	8.7
SP4018	1.0	39.8	55.9	16.0	66.4	16.2
SP4014	1.2	42.6	60.6	28.0	71.9	11.1
SP4012	1.1	44.1	61.4	23.8	66.4	9.9
SP4006	1.2	49.6	65.6	21.7	82.5	20.0
<i>*Critical element</i>						

Appendix H. Section 20 sample results for comparison XRF and LA-ICP-MS. Pearson's correlation values are listed at the bottom of the table.

Comparison of XRF and LA-ICP-MS elemental values										
Sample Number	Sample Name	Mg		Si		Ca		U		
		ppm	(XRF)	ppm	(XRF)	ppm	(XRF)	ppm	(XRF)	
1	SP1026	2670.8	187.9	114522.8	113156.3	250.4	1455.2	16.6	11.5	
2	SP1018	1536.4	135.6	86909.0	93545.2	200.7	1354.4	18.4	12.2	
3	SP1015	2327.3	199.8	91726.1	84103.0	0.0	1106.7	6.1	8.4	
4	SP1006	2115.3	218.4	65275.9	69241.7	289.9	1387.8	7.1	10.1	
5	Clay015	4322.2	700.2	149869.3	115298.2	0.0	1099.8	0.0	7.3	
6	Clay006	5079.6	350.8	145561.6	144366.4	229.5	1144.8	5.5	8.8	
7	SP2026	1511.0	200.3	101756.5	106907.1	213.7	1293.8	11.7	9.3	
8	SP2022	1051.0	331.4	99093.7	101052.5	216.2	1451.1	4.0	7.7	
9	SP2020	885.7	353.1	118317.0	113063.4	268.1	1505.0	9.2	9.6	
10	SP2017	2376.2	152.8	52583.9	50282.5	0.0	1348.5	11.2	15.7	
11	SP2007	2357.6	412.2	119518.8	110526.6	780.3	1652.3	1.4	6.5	
12	SP2005	2592.2	255.3	159685.4	172641.6	323.9	1817.0	12.8	8.5	
13	SP3026	2499.6	363.8	107444.2	97559.5	280.9	1516.8	9.3	9.1	
14	SP3023	4547.3	533.7	78798.3	68148.0	0.0	1178.8	0.0	8.9	
15	SP3008	2944.7	376.1	102165.1	80137.0	0.0	1343.6	0.0	7.9	
16	SP3011	2261.0	241.3	100161.0	102276.2	0.0	1159.9	6.8	8.7	
17	SP4018	2936.7	181.8	32617.3	29012.6	1072.1	3987.9	33.7	16.2	
18	SP4014	4663.7	561.9	43034.2	43509.1	1044.3	2371.3	11.2	11.1	
19	SP4012	3946.3	722.2	41948.9	40672.3	1058.3	2364.1	4.0	9.9	
20	SP4006	2190.1	172.2	20061.9	21192.3	1128.3	4226.9	30.8	20.0	
Pearson's Correlation Coefficient (r)		0.6348		0.9642		0.8549		0.8524		

Comparison of XRF and LA-ICP-MS elemental values											
Sample Number	Sample Name	Ti		V		Cr		Ni		Rb	
		ppm	(XRF)	ppm	(LA-ICP-MS)	ppm	(XRF)	ppm	(LA-ICP-MS)	ppm	(XRF)
1	SP1026	11999.1	14245.9	0.0	188.7	0.0	43.0	0.0	19.7	0.0	1.7
2	SP1018	13162.0	17611.7	0.0	190.4	0.0	40.4	0.0	14.1	0.0	2.0
3	SP1015	11544.5	13976.7	0.0	170.8	0.0	31.3	0.0	13.0	0.0	2.6
4	SP1006	12214.4	15956.6	0.0	162.4	0.0	37.6	0.0	11.8	0.0	2.1
5	Clay015	57612.7	17290.3	0.0	176.0	0.0	38.6	0.0	11.5	0.0	3.4
6	Clay006	12704.0	16341.7	0.0	177.5	0.0	45.7	0.0	11.8	0.6	2.4
7	SP2026	10595.3	12371.4	0.0	151.0	0.0	40.1	0.0	18.2	1.9	3.9
8	SP2022	9440.3	11012.3	0.0	144.5	0.0	25.9	0.0	13.8	0.0	3.4
9	SP2020	11864.1	14992.5	0.0	158.3	0.0	36.6	0.0	23.8	1.1	4.4
10	SP2017	16137.2	18682.8	0.0	197.5	0.0	42.9	0.0	9.2	0.0	1.7
11	SP2007	9770.0	13350.7	0.0	141.8	0.0	37.4	0.0	16.1	0.7	3.2
12	SP2005	9351.1	10253.6	0.0	102.1	0.0	48.9	0.0	20.4	0.0	1.3
13	SP3026	11066.7	14842.3	0.0	181.0	0.0	26.4	0.0	20.3	1.3	3.4
14	SP3023	10671.2	13604.0	0.0	221.4	0.0	32.5	0.0	11.9	0.0	2.8
15	SP3008	9281.7	11852.2	0.0	162.0	0.0	21.1	0.0	11.4	0.0	3.6
16	SP3011	11970.7	16245.2	0.0	156.2	0.0	30.3	0.0	13.1	1.6	3.7
17	SP4018	14549.4	16661.8	0.0	197.9	0.0	53.7	0.0	8.9	0.0	0.7
18	SP4014	15824.6	17132.5	0.0	205.8	0.0	42.1	0.0	8.3	0.0	2.0
19	SP4012	14439.9	16194.6	0.0	219.8	0.0	40.3	0.0	10.5	0.0	1.9
20	SP4006	14639.3	17706.7	0.0	215.8	0.0	58.8	0.0	6.6	0.0	0.9
Pearson's Correlation Coefficient (r)		0.3981		Null		Null		Null		0.6479	

Comparison of XRF and LA-ICP-MS elemental values												
Sample Number	Sample Name	Sr		Zr		Nb		Mo		Ba		(LA-ICP-MS)
		ppm	(XRF)	ppm	(XRF)	ppm	(XRF)	ppm	(XRF)	ppm	(XRF)	
1	SP1026	220.1	225.4	1512.1	1685.4	547.5	620.6	19.0	21.0	0.0	100.0	
2	SP1018	180.8	179.5	1900.1	2014.7	681.1	752.0	31.6	30.0	0.0	68.7	
3	SP1015	130.2	133.2	1718.5	1796.4	600.9	653.9	17.3	22.6	78.4	60.0	
4	SP1006	97.0	101.2	1909.9	2035.7	694.7	763.5	6.9	21.4	15.6	51.3	
5	Clay015	102.4	108.2	2048.5	2275.5	722.5	724.3	8.1	18.0	184.5	86.1	
6	Clay006	89.3	94.5	1744.4	1998.2	628.6	677.7	18.9	33.6	55.7	68.0	
7	SP2026	122.5	121.6	1487.2	1603.8	545.3	596.9	84.9	90.3	0.0	59.0	
8	SP2022	171.7	164.9	1302.7	1425.2	466.2	513.2	38.1	40.6	0.0	52.7	
9	SP2020	129.8	127.3	1607.2	1629.4	587.5	662.4	59.1	60.8	0.0	59.7	
10	SP2017	56.1	61.4	2127.5	2296.0	784.8	926.0	73.6	74.8	0.0	52.9	
11	SP2007	173.0	166.9	1549.3	1566.6	571.3	579.2	2.9	14.4	57.0	53.2	
12	SP2005	238.2	273.8	721.8	759.3	300.4	316.4	52.8	62.7	0.0	74.3	
13	SP3026	118.7	125.2	1668.3	1807.8	591.6	697.2	31.1	33.4	0.0	52.4	
14	SP3023	89.5	90.5	1809.7	1799.9	644.2	671.8	27.4	46.0	118.5	47.7	
15	SP3008	87.0	91.7	1503.8	1552.9	537.1	583.4	9.0	36.6	84.1	46.4	
16	SP3011	88.7	94.6	1702.3	1810.4	625.7	690.9	53.3	55.4	0.0	52.2	
17	SP4018	1120.3	1115.2	1819.3	1858.7	623.5	706.8	16.9	29.1	98.5	198.7	
18	SP4014	176.1	181.2	1950.1	2021.9	715.6	766.5	19.6	25.2	76.5	160.1	
19	SP4012	78.0	85.5	1898.4	2017.1	665.7	756.5	13.9	16.3	14.4	50.1	
20	SP4006	1056.0	1099.7	2036.1	2314.3	695.2	808.1	6.8	28.9	58.9	142.0	
Pearson's Correlation Coefficient (r)		0.9993		0.9790		0.9676		0.9443		0.3355		

Comparison of XRF and LA-ICP-MS elemental values												
Sample Number	Sample Name	La		Ce		Pr		Nd		Pb		(LA-ICP-MS)
		ppm	(XRF)	ppm	(XRF)	ppm	(XRF)	ppm	(XRF)	ppm	(XRF)	
1	SP1026	0.0	188.1	188.5	612.8	0.0	34.1	0.0	90.4	38.6	19.9	
2	SP1018	0.0	47.0	75.7	252.3	0.0	8.4	0.0	24.3	43.6	22.3	
3	SP1015	93.7	43.2	258.8	339.4	86.0	8.1	91.3	25.5	20.1	25.0	
4	SP1006	0.0	29.3	261.0	527.2	0.0	6.2	0.0	20.2	21.8	20.1	
5	Clay015	283.9	84.9	379.6	207.7	343.2	14.3	596.1	44.5	19.4	34.5	
6	Clay006	89.4	77.8	166.2	226.3	0.0	13.4	79.1	41.2	25.9	28.4	
7	SP2026	0.0	53.7	68.6	267.3	0.0	10.8	0.0	34.3	32.5	21.6	
8	SP2022	0.0	36.4	263.5	571.7	0.0	7.2	0.0	22.8	10.4	20.4	
9	SP2020	0.0	39.0	235.3	572.3	0.0	7.8	0.0	23.8	38.2	26.7	
10	SP2017	0.0	34.5	59.6	221.2	0.0	7.7	0.0	24.9	21.4	19.9	
11	SP2007	54.0	43.6	247.0	339.1	18.0	9.1	71.1	29.6	18.9	21.2	
12	SP2005	222.8	636.0	346.2	922.9	0.0	57.0	0.0	110.9	80.8	50.7	
13	SP3026	0.0	30.8	280.0	506.3	0.0	6.6	0.0	21.0	32.1	25.6	
14	SP3023	194.8	37.1	495.5	460.4	235.1	7.4	359.3	24.0	10.2	28.2	
15	SP3008	136.4	31.7	374.0	454.9	141.4	6.6	266.1	21.3	8.0	26.4	
16	SP3011	0.0	33.6	215.3	493.6	0.0	7.0	0.0	21.8	37.2	22.4	
17	SP4018	129.4	229.2	394.7	787.0	0.0	46.2	0.0	116.7	23.8	16.0	
18	SP4014	0.0	46.4	210.6	467.8	0.0	10.6	0.0	36.1	33.2	28.0	
19	SP4012	20.7	43.5	143.8	257.2	0.0	8.4	0.0	27.0	20.2	23.8	
20	SP4006	47.6	126.2	235.6	565.1	0.0	20.9	0.0	56.5	20.8	21.7	
Pearson's Correlation Coefficient (r)		0.4649		0.4862		0.1513		-0.1261		0.5992		
<i>*Values in red are negative</i>												

Comparison of XRF and LA-ICP-MS elemental values			
Sample Number	Sample Name	Th Ppm	
		(XRF)	(LA-ICP-MS)
1	SP1026	105.6	55.6
2	SP1018	116.5	58.2
3	SP1015	59.4	56.8
4	SP1006	76.1	62.5
5	Clay015	14.7	48.8
6	Clay006	68.9	58.6
7	SP2026	104.9	51.1
8	SP2022	28.5	46.1
9	SP2020	65.4	52.8
10	SP2017	130.2	62.9
11	SP2007	63.6	54.3
12	SP2005	87.2	52.7
13	SP3026	111.2	58.7
14	SP3023	29.5	64.7
15	SP3008	25.8	52.9
16	SP3011	95.6	56.7
17	SP4018	124.4	66.4
18	SP4014	135.5	71.9
19	SP4012	71.1	66.4
20	SP4006	100.4	82.5
Pearson's Correlation Coefficient (r)		0.4764	

Appendix I. Full list of elements representative of percent greater than NIST-698 sample from values of LA-ICP-MS results using Equation 5.

Sample	LA-ICP-MS percent greater: NIST-698									
	Na %	Mg %	Si %	Ca %	Sc %	Ti %	V %	Cr %	Ni %	Ga %
SP1026	20.4	42.8	2723.6	67.2	82.5	4.5	46.2	90.6	91.3	44.7
SP1018	17.9	58.8	2234.3	69.5	82.9	29.2	45.7	91.2	93.7	38.5
SP1015	12.8	39.2	1998.6	75.0	85.8	2.5	51.3	93.2	94.2	31.9
SP1006	0.9	33.6	1627.8	68.7	85.3	17.0	53.7	91.8	94.8	51.6
Clay015	12.0	113.0	2777.1	75.2	84.9	26.8	49.8	91.5	94.9	3.8
Clay006	17.3	6.7	3502.4	74.2	84.2	19.9	49.4	90.0	94.7	13.4
SP2026	12.9	39.1	2567.7	70.8	88.1	9.3	56.9	91.2	91.9	19.6
SP2022	4.6	0.8	2421.6	67.3	88.8	19.2	58.8	94.3	93.9	35.8
SP2020	27.1	7.4	2721.3	66.1	86.2	10.0	54.9	92.0	89.5	42.5
SP2017	3.6	53.5	1154.7	69.6	80.6	37.0	43.7	90.6	95.9	47.0
SP2007	2.1	25.4	2658.0	62.7	87.6	2.1	59.5	91.8	92.8	17.2
SP2005	59.7	22.4	4208.0	59.0	89.3	24.8	70.9	89.3	90.9	31.4
SP3026	5.9	10.7	2334.4	65.8	87.1	8.9	48.4	94.2	91.0	41.8
SP3023	17.3	62.4	1600.5	73.4	84.9	0.2	36.8	92.9	94.7	30.9
SP3008	3.4	14.4	1899.7	69.7	87.4	13.1	53.8	95.4	95.0	20.8
SP3011	9.7	26.6	2452.1	73.8	87.1	19.2	55.5	93.4	94.2	40.6
SP4018	0.9	44.7	624.0	10.1	76.1	22.2	43.5	88.2	96.1	114.5
SP4014	30.8	70.9	985.7	46.5	80.6	25.7	41.3	90.8	96.3	49.5
SP4012	37.7	119.7	914.9	46.7	81.0	18.8	37.3	91.2	95.3	34.8
SP4006	19.1	47.6	428.8	4.7	75.8	29.9	38.5	87.1	97.1	102.3
<i>*Values in red are negative</i>										

Sample	LA-ICP-MS percent greater: NIST-698										
	Rb %	Sr %	Y %	Zr %	Nb %	Mo %	Ba %	La %	Ce %	Pr %	
SP1026	301.7	77.1	84.0	265.7	1143.3	192.4	80.5	13.8	139.8	2.4	
SP1018	383.2	41.1	82.5	337.1	1406.6	318.1	24.0	78.5	1.3	75.9	
SP1015	519.5	4.7	83.7	289.7	1210.0	215.3	8.3	80.2	32.8	76.7	
SP1006	406.6	20.5	83.7	341.6	1429.7	198.5	7.3	86.6	106.3	82.1	
Clay015	712.5	14.9	79.1	393.7	1351.2	150.9	55.5	61.1	18.7	59.1	
Clay006	477.2	25.7	82.1	333.5	1257.8	369.1	22.8	64.3	11.4	61.5	
SP2026	816.3	4.4	82.5	248.0	1095.9	1159.8	6.6	75.4	4.6	68.9	
SP2022	699.9	29.6	88.2	209.2	928.2	466.6	4.9	83.3	123.8	79.4	
SP2020	954.3	0.1	85.9	253.5	1227.2	747.9	7.8	82.1	124.0	77.7	
SP2017	309.1	51.7	67.7	398.1	1755.2	943.5	4.5	84.2	13.4	77.8	
SP2007	649.7	31.2	85.9	239.9	1060.4	100.9	4.0	80.0	32.7	74.0	
SP2005	215.9	115.2	94.3	64.7	534.0	774.8	34.2	191.5	261.2	63.3	
SP3026	715.7	1.6	85.6	292.2	1296.9	365.8	5.4	85.9	98.1	81.1	
SP3023	558.8	28.9	85.6	290.5	1246.1	542.4	13.8	83.0	80.2	78.8	
SP3008	749.6	27.9	87.1	236.9	1069.0	411.3	16.3	85.5	78.0	81.1	
SP3011	787.2	25.7	85.6	292.8	1284.2	673.2	5.8	84.6	93.2	80.0	
SP4018	75.3	776.5	82.9	303.3	1316.1	306.0	258.7	5.1	208.0	32.3	
SP4014	384.3	42.4	81.4	338.7	1435.8	251.5	189.0	78.7	83.1	69.5	
SP4012	361.3	32.8	82.1	337.6	1415.6	127.8	9.5	80.1	0.7	76.0	
SP4006	125.0	764.4	79.5	402.1	1519.2	303.1	156.4	42.1	121.1	40.1	
<i>*Values in red are negative</i>											

Sample	LA-ICP-MS percent greater: NIST-698										
	Nd %	Sm %	Eu %	Gd %	Tb %	Dy %	Ho %	Er %	Tm %	Yb %	
SP1026	34.6	60.2	80.6	75.2	76.0	73.5	70.8	61.6	49.1	36.0	
SP1018	82.4	84.6	90.5	85.2	80.4	75.9	71.4	61.1	43.8	30.9	
SP1015	81.5	82.2	89.4	83.7	80.1	75.9	72.3	62.9	49.8	36.7	
SP1006	85.4	84.2	90.0	84.0	80.1	76.2	71.6	61.9	46.2	30.5	
Clay015	67.8	72.7	83.9	77.7	73.6	69.6	65.2	54.9	34.5	16.2	
Clay006	70.2	75.1	85.1	79.6	75.8	72.5	69.8	59.9	44.8	26.4	
SP2026	75.2	78.6	87.0	80.9	76.3	72.0	69.5	61.4	48.6	38.9	
SP2022	83.5	84.7	90.8	84.6	84.0	82.3	80.1	74.1	65.1	54.4	
SP2020	82.8	83.5	89.8	83.6	81.7	79.1	76.0	68.8	54.3	43.2	
SP2017	82.0	79.8	84.5	76.5	61.1	48.8	40.0	24.4	0.6	15.2	
SP2007	78.6	80.1	88.8	81.5	81.1	78.5	76.4	69.0	57.2	45.7	
SP2005	19.8	57.9	78.3	64.3	80.4	85.1	87.8	86.4	85.1	82.2	
SP3026	84.8	84.2	90.6	83.5	82.0	78.7	76.0	67.7	54.4	41.0	
SP3023	82.7	83.2	89.8	82.7	81.5	78.6	75.1	66.4	53.9	39.6	
SP3008	84.6	85.0	90.9	84.9	82.8	79.9	76.7	69.3	58.3	46.9	
SP3011	84.2	84.5	90.5	83.6	82.6	79.5	76.1	67.6	54.7	41.3	
SP4018	15.6	53.1	77.1	66.8	71.0	71.9	69.4	62.0	48.7	35.9	
SP4014	73.9	75.1	84.6	77.5	74.6	71.2	68.6	59.4	42.7	27.5	
SP4012	80.5	80.2	87.2	82.4	75.7	72.2	68.5	59.6	44.3	31.3	
SP4006	59.1	67.4	81.2	69.8	70.3	67.5	63.8	54.3	37.3	21.2	
<i>*Values in red are negative</i>											

Sample	LA-ICP-MS percent greater: NIST-698					
	Lu %	Hf %	Ta %	Pb %	Th %	U %
SP1026	31.4	196.8	1352.9	57.2	107.5	49.2
SP1018	23.1	252.5	1758.6	52.2	117.3	58.1
SP1015	32.2	213.8	1484.7	46.4	111.9	8.7
SP1006	26.3	254.1	1644.0	56.8	133.4	30.8
Clay015	8.2	273.0	1690.3	26.0	82.3	5.0
Clay006	19.4	243.9	1570.2	39.0	119.0	13.9
SP2026	35.3	180.0	1249.5	53.7	90.6	20.2
SP2022	53.2	157.8	1079.7	56.1	72.3	0.6
SP2020	40.4	191.0	1407.6	42.8	97.3	24.9
SP2017	22.4	289.0	1839.1	57.3	134.7	104.1
SP2007	40.1	181.4	1290.6	54.4	102.7	15.8
SP2005	81.8	27.2	534.0	8.9	96.9	10.1
SP3026	35.9	214.9	1537.4	45.1	119.1	18.1
SP3023	36.2	210.3	1492.4	39.5	141.5	14.9
SP3008	41.8	182.8	1336.7	43.2	97.6	2.8
SP3011	36.7	212.0	1503.0	52.0	111.9	12.7
SP4018	32.8	228.4	1525.8	65.7	148.1	109.4
SP4014	23.3	251.0	1663.2	40.0	168.3	44.3
SP4012	27.5	263.8	1685.6	48.9	147.8	28.2
SP4006	17.5	308.9	1807.1	53.4	208.2	159.4

\*Values in red are negative

Appendix J. Complete list of Pearson correlation values of all elements tested by XRF, comparing Fe, Ti, and Al to elements.

Pearson correlation values comparing Fe, Ti, and Al to elements using XRF													
Group	Element compared	Nd	Pr	Ce	La	Ba	Sb	Sn	Cd	Ag	Mo	Nb	Th
Clasts	Fe	0.93	0.91	-	0.74	0.70	-	-	-	-	-	<b>0.68</b>	-
	Ti	<b>0.71</b>	<b>0.70</b>	<b>0.23</b>	-	-	-	-	-	-	-	0.92	0.74
	Al	-	-	0.06	-	-	-	-	-	-	-	-	-
Matrix	Fe	-	-	0.29	-	-	-	-	-	-	<b>0.05</b>	-	<b>0.80</b>
	Ti	-	-	-	-	-	-	-	-	-	-	0.89	0.93
	Al	-	-	-	-	-	-	-	-	-	<b>0.70</b>	0.78	-
SP1	Fe	0.88	0.91	-	0.83	-	-	-	-	-	-	-	-
	Ti	<b>0.32</b>	-	<b>0.23</b>	-	-	-	-	-	-	-	0.60	0.38
	Al	0.61	-	-	0.66	-	-	-	-	-	-	-	<b>0.53</b>
Clay	Fe	0.93	0.90	0.85	0.89	0.88	-	-	-	-	-	-	<b>0.75</b>
	Ti	0.88	0.87	0.79	-	0.77	-	-	-	-	-	-	-
	Al	0.54	0.50	-	-	0.33	-	-	-	-	-	0.57	<b>0.36</b>
SP2	Fe	0.95	0.94	-	0.79	0.95	-	-	-	-	-	-	-
	Ti	-	<b>0.26</b>	<b>0.09</b>	<b>0.31</b>	<b>0.24</b>	-	-	-	-	-	0.89	0.52
	Al	0.76	0.75	0.58	-	0.76	-	-	-	-	<b>0.13</b>	-	<b>0.37</b>
SP3	Fe	0.92	0.91	-	0.90	0.81	-	-	-	-	-	<b>0.54</b>	<b>0.73</b>
	Ti	<b>0.31</b>	<b>0.31</b>	<b>0.36</b>	-	-	-	-	-	-	-	0.89	0.25
	Al	0.61	0.61	0.68	0.63	0.55	-	-	-	-	-	<b>0.31</b>	<b>0.56</b>
SP4	Fe	0.90	0.90	-	-	-	-	-	-	-	-	<b>0.32</b>	-
	Ti	-	<b>0.55</b>	-	-	-	-	-	-	-	-	0.75	-
	Al	-	-	-	-	-	-	-	-	-	-	-	-

\*Values in red are negative

Pearson correlation values comparing Fe, Ti, and Al to elements using XRF													
Group	Element compared	Zr	Y	Sr	U	Rb	Bi	Zr	Y	Sr	U	Rb	Bi
Clasts	Fe	-	<b>0.67</b>	<b>0.76</b>	-	-	-	-	<b>0.67</b>	<b>0.76</b>	-	-	-
	Ti	-	0.97	0.76	-	-	-	-	0.97	0.76	-	-	-
	Al	-	-	-	-	-	-	-	-	-	-	-	-
Matrix	Fe	-	-	<b>0.68</b>	-	-	-	-	-	<b>0.68</b>	-	-	-
	Ti	0.87	-	-	-	-	-	0.87	-	-	-	-	-
	Al	0.76	-	-	-	-	-	0.76	-	-	-	-	-
SP1	Fe	-	<b>0.54</b>	-	<b>0.57</b>	-	-	-	<b>0.54</b>	-	<b>0.57</b>	-	-
	Ti	0.60	0.63	-	0.47	-	-	0.60	0.63	-	0.47	-	-
	Al	-	<b>0.29</b>	-	-	-	-	-	<b>0.29</b>	-	-	-	-
Clay	Fe	-	-	-	-	-	-	-	-	-	-	-	-
	Ti	-	-	-	-	-	-	-	-	-	-	-	-
	Al	0.52	-	-	-	-	-	0.52	-	-	-	-	-
SP2	Fe	-	-	-	-	-	-	-	-	-	-	-	-
	Ti	0.87	0.82	-	0.76	-	-	0.87	0.82	-	0.76	-	-
	Al	-	-	-	-	-	-	-	-	-	-	-	-
SP3	Fe	<b>0.45</b>	<b>0.65</b>	-	-	-	-	<b>0.45</b>	<b>0.65</b>	-	-	-	-
	Ti	0.88	0.81	-	-	-	-	0.88	0.81	-	-	-	-
	Al	-	<b>0.44</b>	-	-	-	-	-	<b>0.44</b>	-	-	-	-
SP4	Fe	<b>0.47</b>	<b>0.77</b>	-	-	-	-	<b>0.47</b>	<b>0.77</b>	-	-	-	-
	Ti	0.80	0.88	-	-	-	-	0.80	0.88	-	-	-	-
	Al	-	-	-	-	-	-	-	-	-	-	-	-
<i>*Values in red are negative</i>													

Pearson correlation values comparing Fe, Ti, and Al to elements using XRF													
Group	Element compared	Au	Se	As	Pb	W	Zn	Cu	Ni	Co	Fe	Mn	Cr
Clasts	Fe	-	-	-	-	-	-	-	-	-	1.00	-	-
	Ti	-	-	-	-	-	-	-	-	-	0.89	-	-
	Al	-	-	-	-	-	-	-	-	-	-	-	-
Matrix	Fe	-	-	-	-	-	-	-	-	-	1.00	-	-
	Ti	-	-	-	-	-	-	-	-	-	-	-	-
	Al	-	-	0.81	-	-	-	0.66	-	-	-	-	-
SP1	Fe	-	-	-	-	-	-	-	-	-	1.00	-	-
	Ti	-	-	-	-	-	-	-	-	-	0.45	-	-
	Al	-	-	-	-	-	-	-	-	-	0.80	-	-
Clay	Fe	-	-	-	0.53	-	-	-	-	-	1.00	-	-
	Ti	-	-	-	-	-	-	-	-	-	0.90	-	-
	Al	-	-	-	-	-	-	-	-	-	0.65	-	-
SP2	Fe	-	-	-	-	-	-	-	-	-	1.00	-	-
	Ti	-	-	-	0.36	-	-	-	-	-	-	-	-
	Al	-	-	-	-	-	-	-	-	-	0.84	-	-
SP3	Fe	-	-	-	0.64	-	-	-	-	-	1.00	-	-
	Ti	-	-	-	-	-	-	-	-	-	0.39	-	-
	Al	-	-	-	0.53	-	0.41	-	-	-	0.77	-	-
SP4	Fe	-	-	-	0.56	-	-	-	-	-	1.00	-	-
	Ti	-	-	-	-	-	-	-	-	-	0.58	-	-
	Al	-	-	-	-	-	-	0.64	-	-	0.61	-	-

\*Values in red are negative

Appendix K - Complete list of Pearson correlation values of elements tested by LA-ICP-MS, comparing Ti elements.

Pearson correlation values comparing Ti to elements using LA-ICP-MS results			
Element	Ti	Element	Ti
Na	<b>0.353</b>	Pr	-
Mg	-	Nd	-
Si	<b>0.530</b>	Sm	-
Ca	-	Eu	-
Sc	0.733	Gd	-
Ti	1.000	Tb	0.639
V	0.674	Dy	0.694
Cr	0.425	Ho	0.723
Ni	<b>0.533</b>	Er	0.746
Ga	-	Tm	0.798
Rb	<b>0.336</b>	Yb	0.827
Sr	-	Lu	0.830
Y	0.775	Hf	0.878
Zr	0.898	Ta	0.895
Nb	0.907	Pb	<b>0.365</b>
Mo	<b>0.242</b>	Th	0.590
Ba	-	U	0.589
La	-		
Ce	<b>0.402</b>		
<i>*Values in red are negative</i>			

## **VITA**

Melanie L. Ertoms graduated from Tarkington High School in Cleveland, Texas in May of 2007. In Fall 2007, Melanie attended Stephen F. Austin State University in Nacogdoches, Texas where she received her Bachelor of Science in Nursing in May 2011. After working as a nurse for several years, Melanie returned to Stephen F. Austin State University in 2017 and acquired her Bachelor of Science in Geology in August 2021. Subsequently she began pursuing a Master of Science in Geology with a Spatial Science minor. Melanie will receive her Master of Science degree in Geology with a Spatial Science minor in May, 2024.

Address: PO Box 633094, Nacogdoches, TX 75963

Style manual designation: Geological Society of America

This thesis was typed by Melanie Ertoms.